

AD-A205 716

POPULATION INVERSIONS IN ABLATION PLASMAS GENERATED BY
INTENSE ELECTRON B. (U) MICHIGAN UNIV ANN ARBOR DEPT OF
NUCLEAR ENGINEERING R M GILGENBACH ET AL. NOV 88

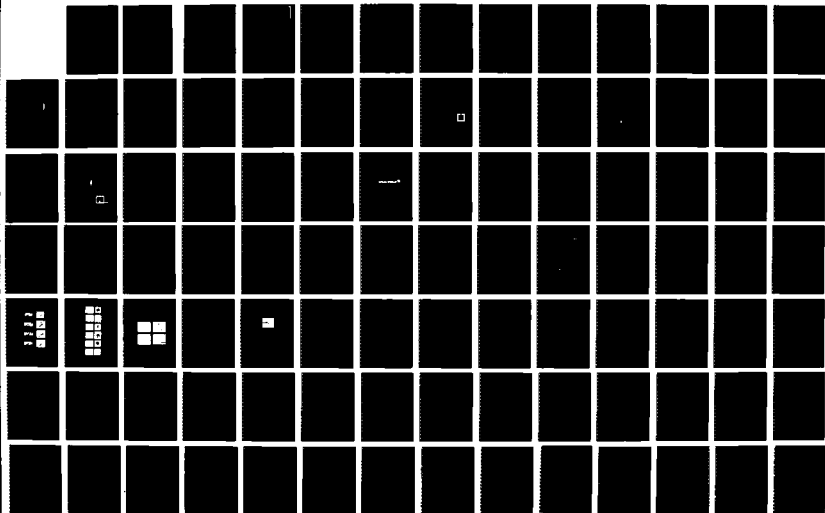
1/2

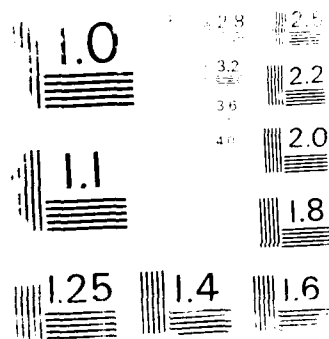
UNCLASSIFIED

AFOSR-TR-89-0294 AFOSR-86-0012

F/G 20/9

NL





AD-A205 716

✓ ②
AFOSR-TR-86-0012

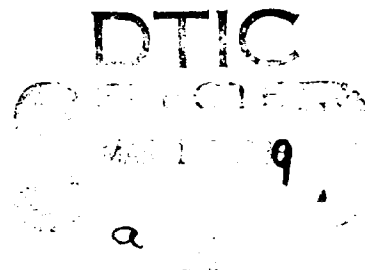
Final Report to:
The Air Force Office of Scientific Research
for the project:

**"POPULATION INVERSIONS IN
ABLATION PLASMAS GENERATED
BY INTENSE ELECTRON BEAMS"
(AFOSR-86-0012)**

R.M. Gilgenbach

T. Kamash

M.L. Brake



Nuclear Engineering Department
The University of Michigan
Ann Arbor, MI 48109

November 1988

Intense Energy Beam Interaction Laboratory



UNCLASSIFIED

SECURITY CLASSIFICATION OF THIS PAGE

REPORT DOCUMENTATION PAGE

1a. REPORT SECURITY CLASSIFICATION Unclassified		1b. RESTRICTIVE MARKINGS	
2a. SECURITY CLASSIFICATION AUTHORITY		3. DISTRIBUTION/AVAILABILITY OF REPORT Approved for public release; Distribution unlimited	
2b. DECLASSIFICATION/DOWNGRADING SCHEDULE			
4. PERFORMING ORGANIZATION REPORT NUMBER(S) AFOSR Final Report, Dec. 1988		5. MONITORING ORGANIZATION REPORT NUMBER(S) AFOSR-TR. 89-0294	
6a. NAME OF PERFORMING ORGANIZATION Nuclear Engineering Dept. University of Michigan	6b. OFFICE SYMBOL (If applicable)	7a. NAME OF MONITORING ORGANIZATION Air Force Office of Scientific Research	
6c. ADDRESS (City, State and ZIP Code) Cooley Bldg., North Campus Ann Arbor, MI 48109		7b. ADDRESS (City, State and ZIP Code) Bolling Air Force Base Washington, DC 20332-6648	
8a. NAME OF FUNDING/SPONSORING ORGANIZATION Air Force OSR	8b. OFFICE SYMBOL (If applicable) NP	9. PROCUREMENT INSTRUMENT IDENTIFICATION NUMBER AFOSR 86-0012	
8c. ADDRESS (City, State and ZIP Code) Bolling Air Force Base Washington, DC 20332-6448		10. SOURCE OF FUNDING NOS.	
		PROGRAM ELEMENT NO. 61102F	PROJECT NO. 2301
		TASK NO. AS	WORK UNIT NO.
11. TITLE (Include Security Classification) Population Inversions in Ablation Plasmas Generated by Intense Electron Beams (U)			
12. PERSONAL AUTHOR(S) R. M. Gilgenbach, T. Kammash, and M. L. Brake			
13a. TYPE OF REPORT Final Report	13b. TIME COVERED FROM 11-1-85 TO 10-31-88	14. DATE OF REPORT (Yr., Mo., Day) 1988, Dec., 22	15. PAGE COUNT 86
16. SUPPLEMENTARY NOTATION			
17. COSATI CODES		18. SUBJECT TERMS (Continue on reverse if necessary and identify by block number)	
FIELD	GROUP	SUB GR	
		intense electron beams, e-beam pumping, anode plasma, spectroscopy	
19. ABSTRACT (Continue on reverse if necessary and identify by block number)			
<p>Experiments during the past three years have concerned the generation and spectroscopic study of electron beam-driven carbon plasmas in order to explore the production of optical and ultraviolet radiation from nonequilibrium populations. A unique electron beam facility, the Michigan Electron Long Beam Accelerator, (MELBA), has been utilized in these investigations. MELBA has been operated with typical parameters of voltage = -0.8 MV, current = 6 to 65 kA, and pulselengths of about 1 microsecond. In this experimental configuration, the output of MELBA has been connected to an electron beam diode consisting of an aluminum (or brass) cathode stalk and a carbon anode. Magnetic field coils have been designed, procured, and utilized during the final year of this project in order to focus the electron beam. A side viewing port permitted spectroscopic diagnostics to view across the surface of the anode. Spectroscopic diagnosis has been performed using a 1 m spectrograph capable of operation from the vacuum ultraviolet through the visible. This spectrograph is coupled to a 1024 channel optical multichannel analyzer. Spectroscopic data can be summarized as follows (over).</p>			
20. DISTRIBUTION/AVAILABILITY OF ABSTRACT UNCLASSIFIED/UNLIMITED <input checked="" type="checkbox"/> SAME AS RPT <input type="checkbox"/> DTIC USERS <input type="checkbox"/>		21. ABSTRACT SECURITY CLASSIFICATION Unclassified	
22a. NAME OF RESPONSIBLE INDIVIDUAL Dr Robert L. Parker	22b. TELEPHONE NUMBER (Include Area Code) 202/767-1911	22c. OFFICE SYMBOL NP	

Spectra taken during the initial 400 ns period of the e-beam pulse showed a low effective charge plasma with primarily molecular components (C_2 , CH) as well as atomic hydrogen and singly ionized carbon (CII). These constituents are probably due to hydrocarbons on the surface of the cathode and anode as well as absorbed gases in the graphite. When the generator pulse was crowbarred after the first 400 ns, the spectra revealed a continuation of the low charge state plasma. At times greater than 400 ns in non-crowbarred shots, the spectra revealed a highly ionized plasma with a very large intensity line at 2530 Angstroms due to CIV (5g-4f), and lower intensity lines due to CIII and CII. This CIV line emission increased with time, peaking sharply between 750 ns and 900 ns, and decayed rapidly in less than 100 ns. (Other researchers at National Bureau of Standards have shown the 2530 Angstrom CIV (5g-4f) line to be a lasing transition in a theta pinch.) Emission from these high ionization states may be due to electron beam-plasma instabilities, as this emission was accompanied by high levels of radio frequency and microwave emission. This high power RF emission may play a role in enhancing the energy transfer from the electron beam to the plasma. At times well after diode shorting, the emission spectra reveal a cooling and recombining plasma. Emission spectroscopy performed with an applied magnetic field of 500-920 Gauss yielded an overall increase in the optical emission intensity, although the features of the spectra were similar to the unmagnetized case. In the magnetized case, the spectroscopic emission also indicated an extremely non-equilibrium carbon plasma or plasma species which have not yet been identified. Data analysis is underway to determine whether population inversions were generated in the magnetized and unmagnetized case.

A number of other electron beam-plasma diagnostics have been developed in this research, including: 1) Cerenkov plate with gated-intensified microchannel plate camera, 2) Laser deflection system, 3) Radio Frequency and microwave probes, 4) Faraday cups, and 5) B-dot loops. These diagnostics also show that the electron beam interaction with the dense carbon plasma is subject to a strong electron beam-plasma instability. This apparent instability also shows large fluctuations in the cathode current, a spreading of the electron beam profile on Cerenkov plates, and is associated with the phenomenon of "voltage peaking". Voltage peaking behavior showed a large increase in the e-beam generator voltage after predicted cathode shorting.

Theoretical models have been developed in order to understand the emission from an electron beam heated carbon plasma with special emphasis on the CIV (C^{++}) 5g-4f transition occurring at 2530 Angstroms. This study was motivated by the experiments carried out on MELBA, and represents an attempt to understand the plasma response to various electron beam parameters. The evolution of the 2530 Angstrom line emission cannot be studied by only considering plasma ionization dynamics (atomic physics). Heating and cooling rates which depend on the plasma macroscopic evolution and electron beam-plasma interactions are important. The complete theoretical model consists of three coupled modules describing the plasma hydrodynamics, ionization dynamics, and electron beam-plasma interactions. A one dimensional geometry was utilized and an optically thin plasma was assumed in addition to the absence of externally applied electromagnetic fields. These studies revealed two characteristic responses of the plasma to electron beam heating. Type A plasma occurs for "slow" heating rates which cause slow barrier burnthrough and little heating with the subsequent 2530 Angstrom emission being of low intensity. Type B plasma quickly burns through the radiative emission barrier to reach temperatures where significant 2530 Angstrom emission is observed. Model results agree qualitatively with MELBA experimental observations, indicating a Type A response.

Table of Contents	page
1.0 Executive Summary	2
1.1 Experimental Program	2
1.2 Theoretical Program	3
2.0 Introduction	4
3.0 Experimental Configuration and Diagnostics	5
3.1.1 MELBA Marx Generator	5
3.1.2 Diode Configuration	9
3.2 Diagnostics	13
3.2.1 Electrical Diagnostics	13
3.2.2 Particle/ Beam Diagnostics	16
3.3.3 Plasma Diagnostics	19
4.0 Experimental Results	27
4.1 Optical and Ultraviolet Spectroscopy of Electron Beam Driven Plasmas	27 27
4.2 Electron Beam Dynamics and Diode Plasma Physics	48
4.3 References for Section 4	60
5.0 Theoretical Progress on Electron Beam-Induced Emission from Carbon Plasmas	61
5.1 Theoretical Model	61
5.2 General Parameter Studies	65
5.3 MELBA Implications	71
5.4 References for Theoretical Progress Section	73
6.0 Graduate Students and Doctoral Dissertations Supported by this Grant	75
7.0 Publications Resulting from This Grant	76
8.0 References	78
9.0 Reprints of Publications	87

1.0 Executive Summary

1.1 Experimental Program

Experiments during the past three years have concerned the generation and spectroscopic study of electron beam-driven carbon plasmas in order to explore the production of optical and ultraviolet radiation from nonequilibrium populations. A unique electron beam facility, the Michigan Electron Long Beam Accelerator, (MELBA), has been utilized in these investigations. MELBA has been operated with typical parameters of voltage = -0.8 MV, current = 6 to 65 kA, and pulselengths of about 1 microsecond. In this experimental configuration, the output of MELBA has been connected to an electron beam diode consisting of an aluminum (or brass) cathode stalk and a carbon anode. Magnetic field coils have been designed, procured, and utilized during the final year of this project in order to focus the electron beam. A side viewing port permitted spectroscopic diagnostics to view across the surface of the anode. Spectroscopic diagnosis has been performed using a 1 m spectrograph capable of operation from the vacuum ultraviolet through the visible. This spectrograph is coupled to a 1024 channel optical multichannel analyzer. Spectroscopic data can be summarized as follows. Spectra taken during the initial 400 ns period of the e-beam pulse showed a low effective charge plasma with primarily molecular components (C_2 , CH) as well as atomic hydrogen and singly ionized carbon (CII). These constituents are probably due to hydrocarbons on the surface of the cathode and anode as well as absorbed gases in the graphite. When the generator pulse was crowbarred after the first 400 ns, the spectra revealed a continuation of the low charge state plasma. At times greater than 400 ns in non-crowbarred shots, the spectra revealed a highly ionized plasma with a very large intensity line at 2530 Angstroms due to CIV (5g-4f), and lower intensity lines due to CIII and CII. This CIV line emission increased with time, peaking sharply between 750 ns and 900 ns, and decayed rapidly in less than 100 ns. (Other researchers at National Bureau of Standards have shown the 2530 Angstrom CIV (5g-4f) line to be a lasing transition in a theta pinch.) Emission from these high ionization states may be due to electron beam-plasma instabilities, as this emission was accompanied by high levels of radio frequency and microwave emission. This high power RF emission may play a role in enhancing the energy transfer from the electron beam to the plasma. At times well after diode shorting, the emission spectra reveal a cooling and recombining plasma. Emission spectroscopy performed with an applied magnetic field of 500-920 Gauss yielded an overall increase in the optical emission intensity, although the features of the spectra were similar to the unmagnetized case. In the magnetized case, the spectroscopic emission also indicated an extremely non-equilibrium carbon plasma or plasma species which have not yet been identified. Data analysis is underway to determine whether population inversions were generated in the magnetized and unmagnetized case. A number of other electron beam-plasma diagnostics have been developed in this research, including: 1) Cerenkov plate with gated-intensified microchannel plate camera, 2) Laser deflection system, 3) Radio Frequency and microwave probes, 4) Faraday cups, and 5) B-dot loops. These diagnostics also show that the electron beam interaction with the dense carbon plasma is subject to

a strong electron beam-plasma instability. This apparent instability also shows large fluctuations in the cathode current, a spreading of the electron beam profile on Cerenkov plates, and is associated with the phenomenon of "voltage peaking". Voltage peaking behavior showed a large increase in the e-beam generator voltage after predicted cathode shorting.

1.2 Theoretical Program

Theoretical models have been developed in order to understand the emission from an electron beam heated carbon plasma with special emphasis on the CIV (C^{4+}) 5g-4f transition occurring at 2530 Angstroms. This study was motivated by the experiments carried out on MELBA, and represents an attempt to understand the plasma response to various electron beam parameters. The evolution of the 2530 Angstrom line emission cannot be studied by only considering plasma ionization dynamics (atomic physics). Heating and cooling rates which depend on the plasma macroscopic evolution and electron beam-plasma interactions are important. The complete theoretical model consists of three coupled modules describing the plasma hydrodynamics, ionization dynamics, and electron beam-plasma interactions. A one dimensional geometry was utilized and an optically thin plasma was assumed in addition to the absence of externally applied electromagnetic fields. These studies revealed two characteristic responses of the plasma to electron beam heating. Type A plasma occurs for "slow" heating rates which cause slow barrier burnthrough and little heating with the subsequent 2530 Angstrom emission being of low intensity. Type B plasma quickly burns through the radiative emission barrier to reach temperatures where significant 2530 Angstrom emission is observed. Model results agree qualitatively with MELBA experimental observations, indicating a Type A response.

2.0 Introduction

Plasma use as a lasing medium has many potential advantages over conventional techniques including increased power levels and greater wavelength ranges, particularly in the ultraviolet and soft X-ray regimes. The basic concept, first proposed by Gudzenko¹, is to heat and then rapidly cool a plasma forcing inversion through bottleneck creation between the recombination reaction populating a given energy level and the subsequent decay processes. Much effort has been devoted to plasmas heated by lasers² and pinch devices³. The ultimate efficiency of laser driven plasma lasers is limited by the relatively low efficiency of the laser used to pump the plasma. A plasma laser driven directly by a pulsed power source (e.g. Marx generator) has the potential for high efficiency, compact/light weight design, and moderate cost. The Soviets have investigated intense proton beam pumped plasma lasers, however, the University of Michigan experiments are the first to explore the possibility of directly driving plasma emission by means of a long-pulse, intense, relativistic electron beam.

1. L. I. Gudzenko and L. A. Shelepin, Sov. Phys. JETP **18**, 988 (1963). Also L. I. Gudzenko, L. A. Shelepin, and S.I. Yakovlenko in Proceedings of the P. N. Lebedev Institute, G. N. Basov, Ed., 1977, Vol. 83.

2. For example see S. Suckewer, C. K. Skinner, H. Milchenburg, C. Keane, and D. Voorhees, Appl. Phys. Lett. **55**, 1753 (1985).

3. R. U. Datla, J. R. Roberts, and M. Blaha, J. Quant. Spect. Radiat. Transfer **16**, 1043 (1987).

3.0 Experimental Configuration and Diagnostics

3.1.1. Marx Bank

These experiments were performed on the Michigan Electron Long Beam Accelerator (MELBA). MELBA is driven by a long pulse Marx bank with an additional capacitor stage designed for voltage compensation (at 1 MV, 10 kA, and 1.5 μ s). This design, due to Abramyan [Abr77a, Smi79] uses a reverse-charged, ringing capacitor stage for voltage compensation of the natural Marx RC decay and decay from impedance collapse caused by diode closure. See [Gil85, Luc88] for a description of the generator and further descriptions of voltage compensation in theory and practice. Voltage compensation was not an important issue in the experiments performed in this thesis. Typical MELBA parameters for these experiments are peak voltages of -0.8 MV, currents up to 60 kA, and pulselengths between 0.5 and 4.0 μ s depending on gap length, closure velocity and crowbar setting.

An equivalent circuit for MELBA [Pul83] with erected Marx and diode load is shown in Figure 3.1. In addition to the physical components and lumped element values for the primary current flow paths, the model includes parasitic elements as well: stray capacitances, inherent inductance loops, and the effective Marx shunt impedance. These values were determined by Pulse Sciences, Inc., for their Marx bank design proposal, by a combination of measurements, empirical approximations, and analytical estimates. A lumped element approach is valid when the shortest characteristic wavelengths of the power pulse (fastest frequencies i.e. during the rise time), are much greater than the characteristic lengths (frequencies) of the device. This condition is satisfied for the MELBA diode stalk dimensions and typical risetimes by slightly greater than a factor of ten

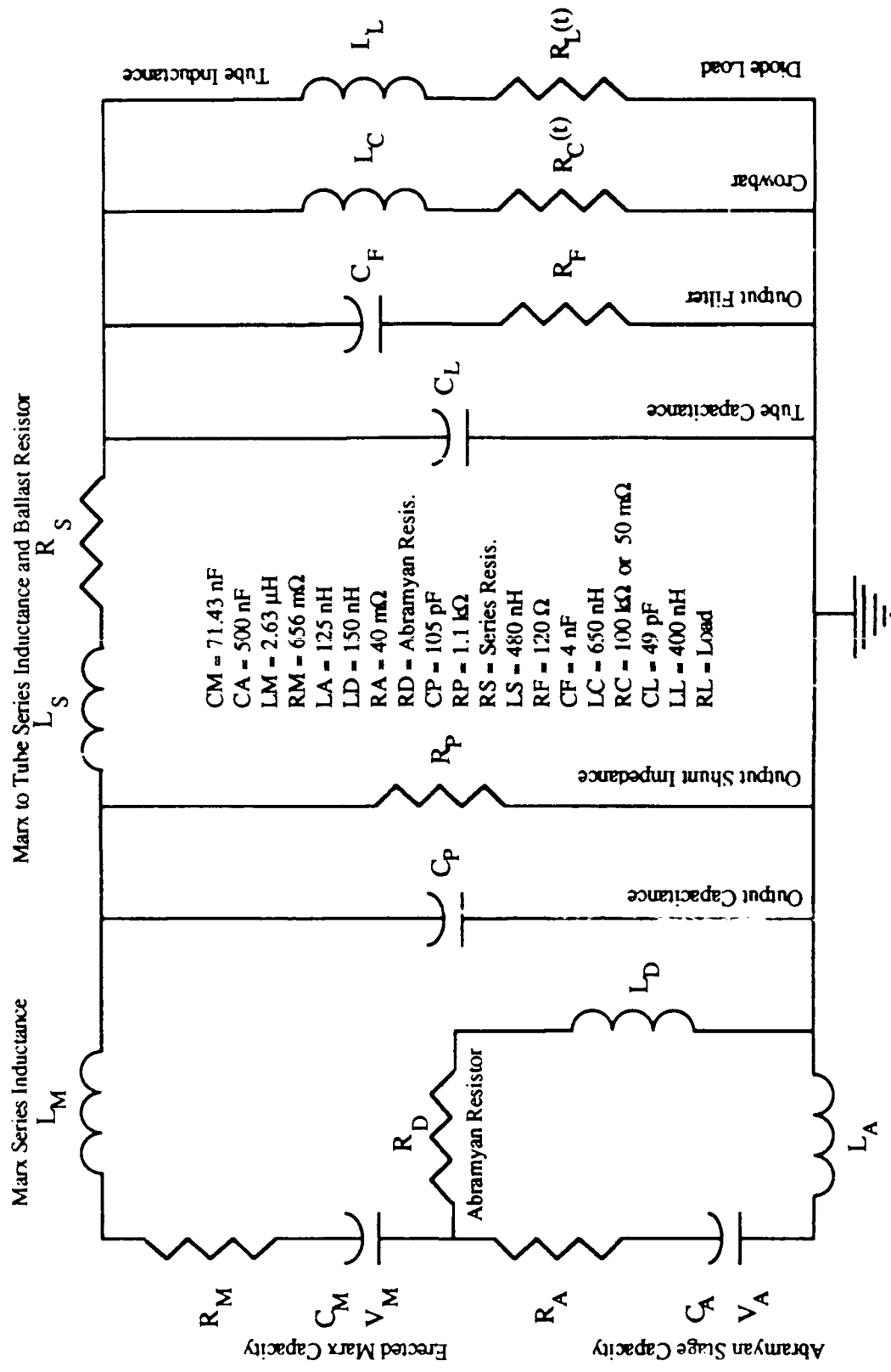


Figure 3.1MELBA equivalent circuit model

In addition to the Abramyan stage, (here represented by the elements subscripted A and D), and the main Marx stage (subscripts M), Figure 3.1 displays several machine features important in a discussion of the experiment. The crowbar gap, a high pressure SF₆ gap in parallel with the diode load, can be command triggered with preset time delays. The crowbar is intended to limit the total energy delivered to the diode, after the desired desired pulselength is obtained, by short circuiting the generator. When short pulses were desired, the crowbar would be triggered before diode shorting. Due to the rapid impedance collapse, crowbarred operation beyond 300-500 ns was difficult to obtain for the small gap experiments described in this thesis. In non-crowbarred shots the diode was allowed to short circuit before the crowbar was command triggered. This is the most common mode of operation used here. This mode maximized energy and current densities incident on the anode and also allowed determination of the plasma closure velocity. The diode load is represented by the stalk inductance L_L , and a diode impedance $R_L(t)$ where allowance can be made for both time-dependent inductive and resistive components. The time-dependent nature of the diode load is due to the phenomenon of cathode plasma closure, which leads to decaying impedance, and other phenomena which lead to changing impedance. The series (or ballast) resistance R_S , is intended to absorb the full generator energy in a crowbar or in the event of a diode short circuit. This resistance (2 - 4 ohms) does not have a great effect on the overall performance of the device, as the characteristic impedance ($2\sqrt{L/C}$) of the Marx is 14 ohms. In Figure 3.1, the voltage monitor measures the accelerator voltage across the tube capacitance, output filter, crowbar, and load, before the tube inductance. The final feature that should be noted is the RC filter on the Marx output, necessary to limit the voltage peak during the initial risetime of the accelerator.

The MELBA equivalent circuit has been simulated using transient circuit analysis codes. Codes which have been used are SCPETRE and various versions of SPICE [Nag81]. Figure 3.2 shows an early comparison [Gil85] of theory and experiment for a

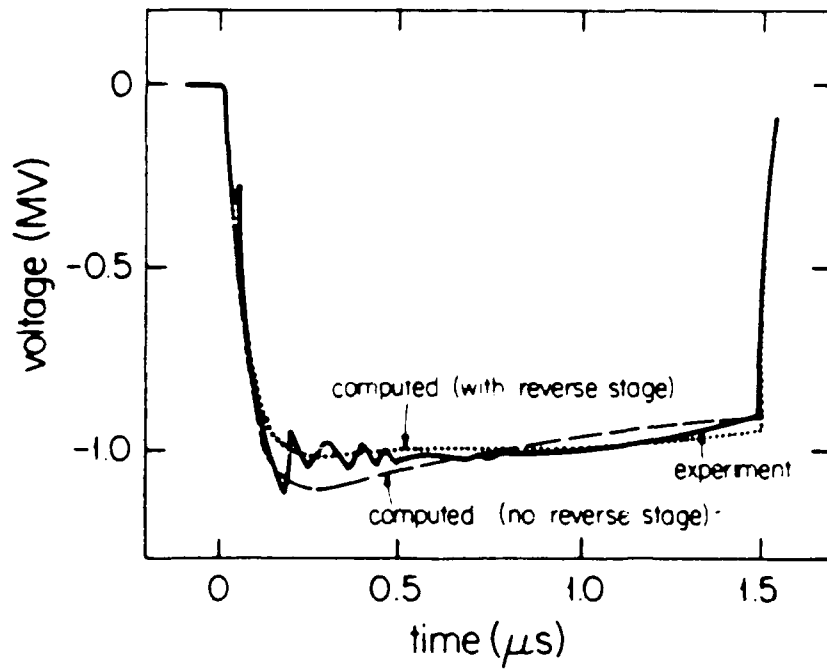


Figure 3.2. Comparison of SPICE simulations of the MELBA equivalent circuit with experimental data for a resistive generator load. The agreement is quite good, demonstrating that the circuit model is satisfactory. Note also the effect of voltage compensation, particularly in the beginning of the pulse.

resistive diode load (performed by Joel Miller using SPICE). As can be seen, the agreement is quite good, indicating that the lumped-element model is satisfactory; some minor differences indicate that additional transmission line effects or parasitic elements may need to be included for complete agreement. The generator short-circuit current predicted by this model is about 65 kA from SPICE simulations, and this agrees with peak experimental currents obtained after diode shorting for the short gap diodes. Some of the circuit values have changed over time and components have failed and been replaced. Good agreement of simulation and experiment depended on precise values.

3.1.2. Diode Configuration

The diode configuration used for the experiments is depicted in the cutaway view of Figure 3.3 (not to exact scale). Refer to the letters in the figure in the description which follows. The incident power pulse from the Marx travels to the right along a blunt nosed cathode stalk (a) (radius = 5.5 cm) through the accelerator insulator and grading ring stack (b). This cathode stalk is at the minimum electric field radius for the coaxial cylindrical geometry. The cathode stalk is sprayed with Glyptal to aid in prevention of breakdown (1201-A Red Insulating Enamel, Glyptal Inc., Chelsea, MA). According to work on the prevention of high voltage breakdown at long pulselengths at Sandia [San78], Glyptal gave very good results, preventing emission up to fields of 200 kV/cm. Examination of the cathode stalk after a run showed that many emission sites were visible along the entire length of the stalk, with a small melted aluminum spot (0.1 cm diameter) visible where the Glyptal has pitted. These emission sites increased in number and severity as the number of shots increased. Similar treatment of another cathode stalk used for low current density experiments, revealed very few emission sites. The differences could be due to the large amount of plasma formed in the diode region during these experiments. This type of damage has been observed in other experiments where anode participation has been

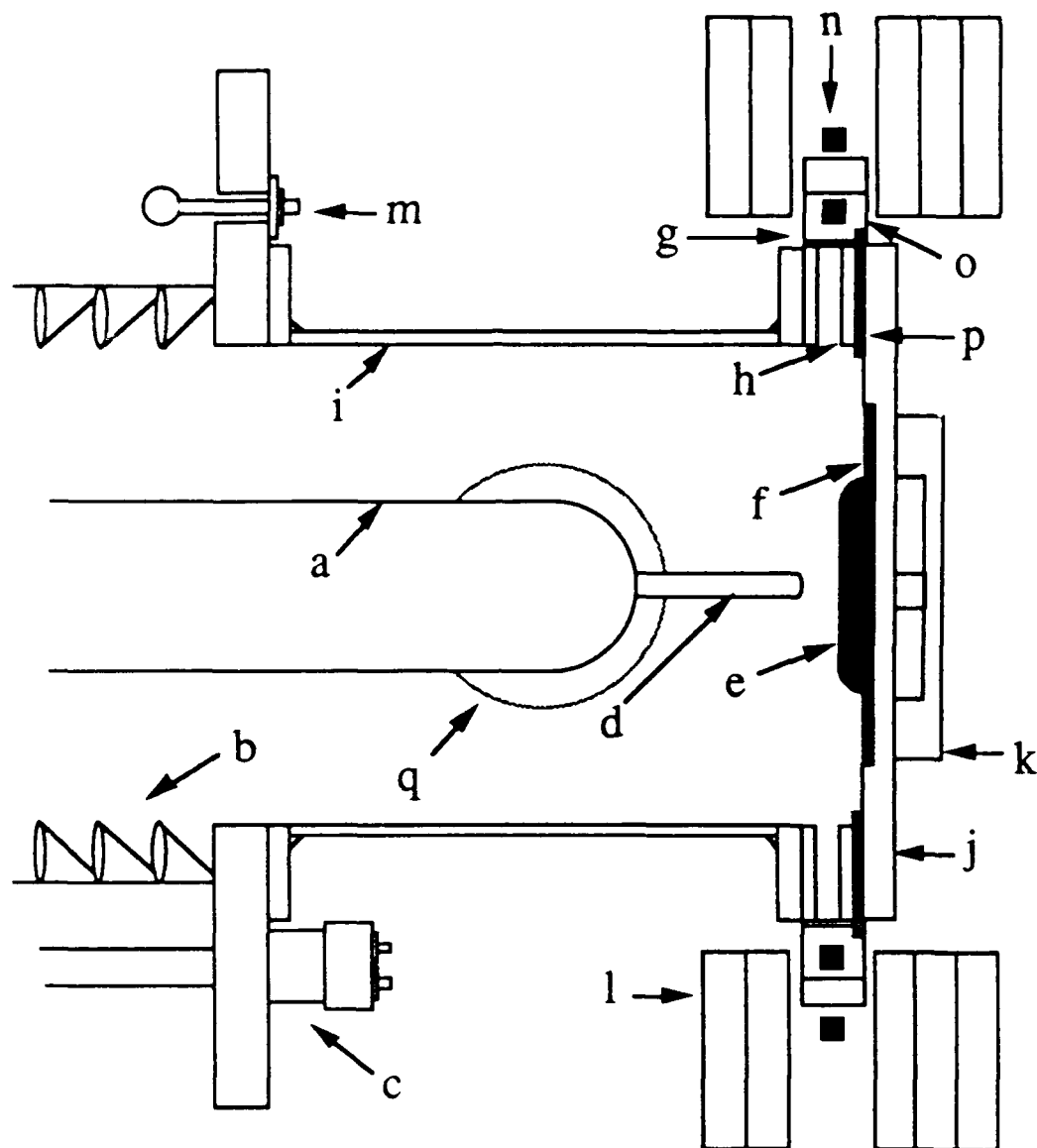


Figure 3.3. Cutaway view of primary diode configuration from above showing Glyptal coated cathode stalk (a), diode insulating stack (b), voltage monitor (c), aluminum or brass rod cathode (d), carbon anode surfaces (e),(f), transverse viewing windows (g), transverse viewing flange (h), aluminum diode chamber (i), aluminum end flange 1 (j), aluminum end flange 2 (k), 5 pancake magnetic field coils (l), B-dot loop current diagnostic (m), Pearson coils (n), current return path (o), insulating Teflon spacer (p), and diffusion pump port(q).

observed [Gra85, Gra86]. Anode participation can lead to microparticle formation and subsequent deterioration and poorer performance of the cathode on succeeding shots.

The experimental voltage monitor (c) measures the voltage from the cathode supporting plate (where the full machine voltage is applied) to ground across the insulating stack. The rod cathodes (d) were made of brass or aluminum, with a radius, $r = 0.6$ cm. Anode-cathode (AK) gaps for the short gap experiments ranged from 3.1 to 4.2 cm. This low aspect ratio diode design was chosen to increase the current density over the early large gap experiments, but was intended to minimize the total current and rate of impedance collapse in an attempt to retain some ability to crowbar the pulses. This was only moderately successful. An important consideration in the selection of the cathode material was the choice of different materials for the anode and cathode, which enabled spectroscopic identification of the sources of the diode plasma. In the early large gap experiments, carbon brush or velvet was necessary to aid in field enhancement. Differentiation between cathode and anode plasma light was difficult under these conditions. The rod cathode has very high electric fields which aid in cathode turn-on. A disadvantage to this design was that the geometry dependent effects on the diode impedance were difficult to estimate analytically.

The anode (e),(f) was extended to allow the surface region of most intense electron bombardment to be observed through the transverse windows (g) mounted on aluminum flange (h). Part (e) was Poco graphite HPD-1, part (f) Poco graphite AXF-5Q (Poco Graphite Inc., Decatur, TX). The large graphite block (e) (17.8 cm diameter, 6 cm thick) was mounted on end flange (k). This assembly was removeable for insertion of a light source to align the spectroscopic optics. In experiments described below in section 3.2.2, the solid anodes as shown in this figure, were modified to allow the beam to be extracted through apertures for measurements of the beam dynamics. The transverse viewing flange (h) was successful in reducing the amount of direct electron flux incident on the transverse viewing windows (g).

The diode resides in an all aluminum chamber (i) (inner radius = 19.45 cm), whose side walls and end flanges (j),(k) are quite thick (0.8 cm and 2.54 cm respectively). The conductivity and thickness of the diode chamber posed special problems in the design and fabrication of the pulsed magnetic field coils (l). Much of the data taken was without a magnetic field except where noted. Shown in the figure is a coil configuration which will give a field in the AK gap region, uniform to 1% from DC measurements. (Magnetic diffusion effects increase field uniformity over this value). Other spatial configurations are possible due to the pancake nature of the coils and overhead adjustment rail. Different field strengths could be obtained using different charging voltages on the capacitors, or using different timing delays between the bank and Marx trigger. These coils had to be designed with enough inductance so that the current pulse would be slow enough to allow magnetic field diffusion through the chamber. A large inductance implies a larger coil resistance which will reduce the percentage of capacitor bank energy that is converted to magnetic field energy. These magnet design issues and bank details are more fully discussed in Appendix A.

The total cathode stalk current was measured with a B-dot loop (m) which extended through the front flange of the Marx oil tank. The signal was integrated at the Faraday cage with a nominally 20 μ s integrator yielding a signal proportional to current. This B-dot loop responded to the time changing azimuthal field created by the current traveling along the cathode stalk and was calibrated *in-situ* with a current return path as close as possible to the experimental one. The current from the diode which flows to the front anode plate (tube return current) was measured using current transformers (n) (Pearson Electronics 110A, Palo Alto, CA) placed on 4 azimuthally spaced, low-inductance current return paths (o). These return paths were isolated by using insulated bolts and a Teflon spacer (p). These 4 return paths were located 60° above and below the two transverse viewing windows which were directly on the machine centerline. Further details on the accelerator electrical diagnostics are given in section 3.2.1.

The diode chamber was evacuated by a roughing pump (typical hydrocarbon-based pump oils) and a diffusion pump (silicon-based oils) through the port (q), directly below the cathode stalk in the figure. The diode pressure was always less than 10^{-4} torr before firing the Marx. Not shown in the figure are the x-ray monitor and x-ray pinhole camera which were used on occasion. These diagnostics were set up to view the end flanges. The entire chamber except for the end flanges, was covered with 2 cm of lead shielding. Line of sight from the end flange to the operator area was also well shielded with lead bricks and sheets.

This diode configuration has been simulated using the code EGUN.

The code is somewhat borderline in its usefulness for high current intense beam diodes. If a great deal of care is taken to ensure convergence of the code, some quantitative results can be obtained. In Figure 3.4, the initial cathode surface electric field enhancement profile (no electron space charge) for the small gap diode is shown. The units are kV/cm per kV applied to the cathode. The distance scale for the figure is 0.25 cm/mesh unit. The cathode surface will not field-emit for fields of ≈ 100 kV/cm and lower.

3.2. Diagnostics

3.2.1. Electrical Diagnostics

Interpretation of the electrical diagnostics form an important basis of the theory for these experiments. As described in the introduction, the beam-plasma interaction is taking place within the diode. The investigations are concerned primarily with the anode plasma which is visible through the transverse viewing windows described above in section 3.1.2. The anode plasma which is formed has an effect on the impedance evolution of the diode. However, the motion of the cathode plasma allows it to come into view as well. In order to interpret the signals from the plasma diagnostics described below, the electrical diagnostics can be used in conjunction with a suitable model of the

ROD CATHODE, EXTENDED ANODE, 3.8 CM AK GAP, NO MAGNETIC FIELD

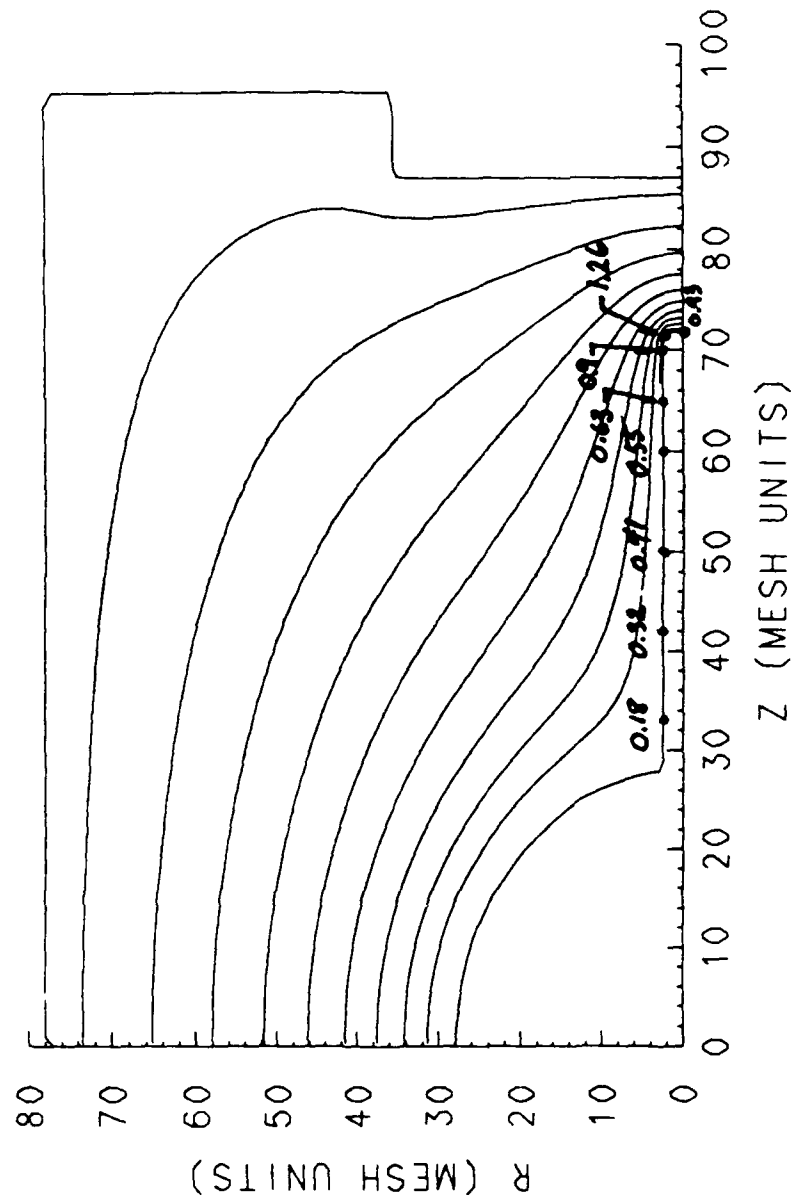


Figure 3.4. EGUN results for the cathode field enhancement profile (without electron space charge effects), for a 3.8 cm gap diode. The units above are $kV/cm/kV$ where the profile is normalized to the gap voltage.

diode impedance to predict the velocity of the cathode plasma, and therefore when shorting can be expected to occur. In addition, understanding and modeling the modification of the diode impedance evolution and stability (and thereby the diode electrical signals) in response to the plasma formation is of interest in its own right.

The voltage monitor measured across the diode insulating stack, but before the cathode stalk. The voltage correction due to inductive drop on the cathode stalk was always less than 5% due to the slow risetimes and was therefore neglected. This voltage monitor was a balanced, water solution (Cu_2SO_4) resistive divider which gave a factor of 179:1 attenuation. A resistive divider using carbon resistors gave another factor of $\approx 88:1$ with another factor of 10 introduced at the screen room. This gave a nominal attenuation of 160,000. Normally, the voltage was split for display on two scopes, and terminated in $50\ \Omega$. In this case, actual external calibration of the voltage monitor gave the factor 308 kV/Volt.

The current flowing to the front anode plate (tube return current) was measured by wide-band current transformers (Pearson Electronics 110A) on four isolated current return paths which were summed at the Faraday cage using $50\ \Omega$ RF power ferrite core adders (Mini-Circuits ZSC2-2, Brooklyn, NY). The signal from each Pearson monitor was attenuated by a factor of 100. These four signals were summed two at a time with separate adders. These two signals were in turn summed with a third power adder. Each adder introduced between 3.3 and 3.6 dB attenuation depending on the frequency in the range 2 KHz to 60 MHz. The final signal was attenuated by another factor of 10, before display on the scope ($50\ \Omega$ termination). The calibration of the entire combination was $25.0 \pm 0.7\ \text{mV/kA}$. Care must be taken in the use of these RF adders. When used in the configuration for the Mirnov coil position monitors, extra $50\ \Omega$ terminators have been added, which change the calibration to $12.4 \pm 0.3\ \text{mv/kA}$.

After shot M1105, the total Marx current could also be measured by integrating the signal from a calibrated B-dot loop. The B-dot loop responds to the time-changing azimuthal magnetic field due to the current flowing in the entire cathode stalk, and is integrated to yield a signal proportional to current. This current is the principal one of interest when comparison of generator performance with its equivalent circuit performance is desired. The L/R risetime for this diagnostic was 7.0 ns, corresponding to a bandwidth of 143 MHz, giving a much faster response than the above current diagnostic. In these experiments, the monitor shows very large fluctuations after 400-600 ns which may be due to the presence of an instability in the diode, (during which time RF emission is also detected from the diode). As a result of these fluctuations, the diode current is normally viewed with a 20 MHz scope input filter switched on to aid in digitizing. The calibration factor for this diagnostic, when integrated by a 20.5 μ s RC

3.2.2. Particle/Beam Diagnostics

Cerenkov Converter

To obtain a time-resolved photograph of the beam current density profile, a Cerenkov plate diagnostic was used with a gated microchannel plate image intensifier tube camera. Time-integrated photographs are obtained using an open shutter camera. The experimental configuration is shown in Figure 3.5. Refer to this figure in the discussion which follows. The anode configuration used allowed the beam to be extracted through a carbon mask (normally Poco HPD-1) with an array of apertures (b). The values used for hole diameter, mask width, and drift distance, and the criteria involved in selecting these properly are discussed below. This mask is placed in the diode chamber (a) prior to putting on the large aluminum end flanges. The carbon mask insert (10.2 cm diameter - a snug press fit, 0.7 cm thick) is pulled flush with the surface of the extended carbon piece (also HPD-1) (c) and screwed into place from behind. This

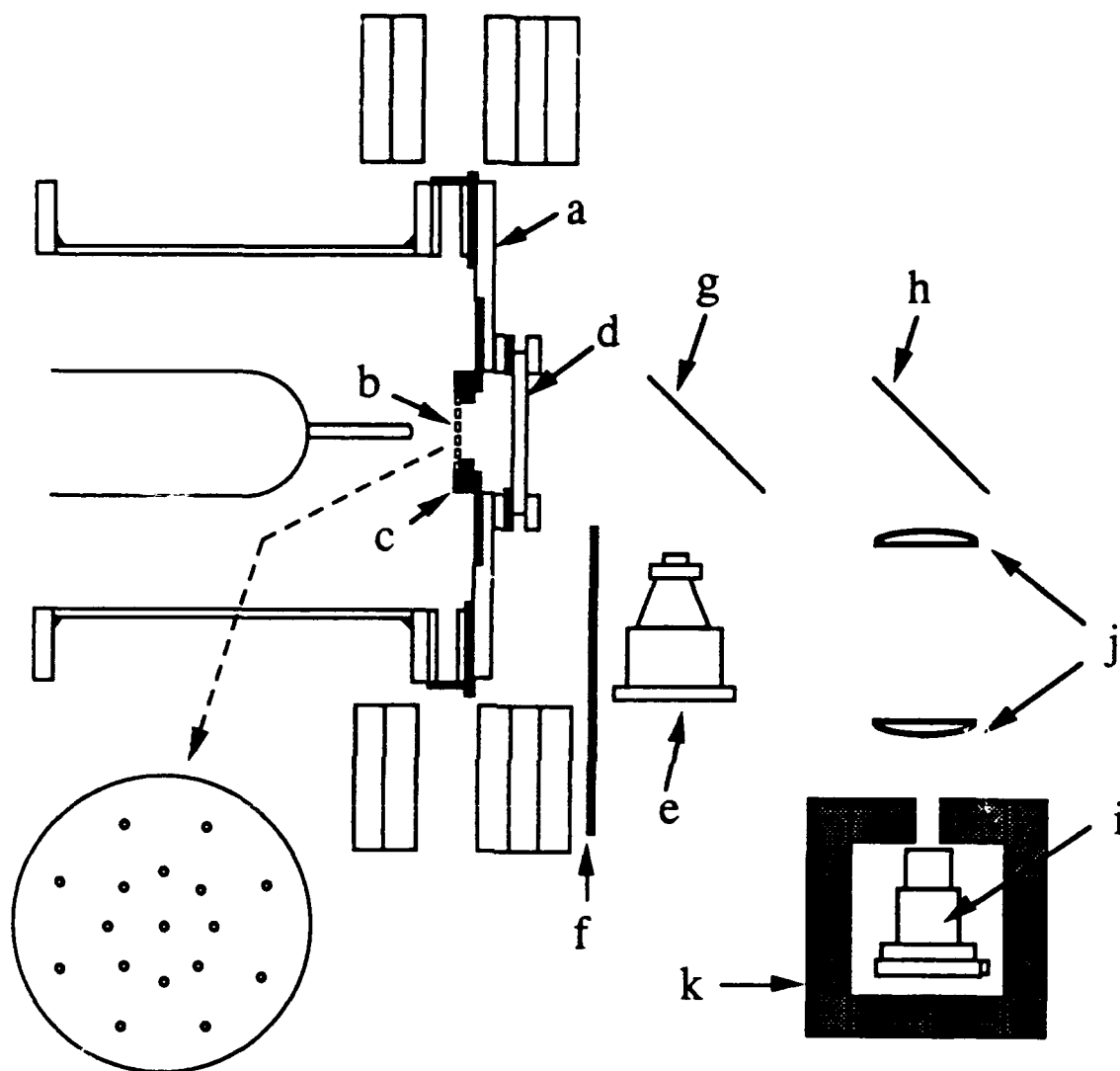


Figure 3.5. Experimental configuration for beam dynamics measurements showing the diode chamber (a), apertured carbon beam mask anode insert (in position) (b), extended carbon anode (c), Cerenkov plate-glass convertor (d), open shutter camera position (e), lead shield (f), turning mirror position for open shutter camera (g), turning mirror position for gated camera (h), intensifier-tube gated camera (i), telescope (j), lead bunker (k). Also shown is a view of a typical mask.

procedure enabled spectroscopic optics to be aligned as well. (The screws are loosely threaded to prevent cracking of the insert when thermal expansion occurs during the pulses). These apertures caused no observable differences in diode behavior. A blowup of a typical mask is also shown in Figure 3.5. The masks had an aperture at the center, and one or two rings of eight apertures at 2 and 4 cm radius, each aperture spaced 45° apart. The outer two rings were rotated 22.5° from each other so that the beamlet images would not overlap on the Cerenkov plate. The use of inserts allowed precise determination of the amount of carbon lost by weighing with an analytical balance before and after (keeping in mind that the majority of the erosion comes after the pulse in the arc). After entering the mask, the electrons drift until they strike a 2 cm thick plate glass. To prevent the photography of diode plasma light, the side of the glass plate facing the mask was coated with a multiple layers (3-4) of Aerodag, a colloidal carbon spray (Aerodag G, Acheson Colloids, Port Huron, MI), until it was opaque.

Both time-integrated and time-resolved pictures are taken of the beamlet images. Time-integrated pictures were obtained using an open-shutter camera (e), and a turning mirror (g). No fogging of film was observed when the camera was shielded with one sheet of 0.3 cm thick lead (f). Type 57 Polaroid film was used with an f-stop of 22. No exposure was obtained with type 55 P/N. Time-resolved pictures are taken with a image intensifier tube camera (i), developed using plans from NRL [Hau85]. The image was also turned in a mirror (h), and expanded using a pair of lenses (j) as a telescope. The camera was located in a completely enclosing lead bunker (k) (side wall thickness = 5 cm, top and bottom thickness ≈ 0.6 cm) to shield the microchannel plate/intensifier tube combination from x-rays, which would completely saturate the film. Other experimental details are the same as in previous discussions.

The gated camera consisted of a conventional Hasselblad single-lens-reflex camera with 80-mm lens, (normally used with 8 mm extension tube), and a Polaroid film back. A gateable, proximity-focused, image intensifier tube is located between the camera and film back.

Apertured Beam Detector/Faraday Cup

Two techniques were used to directly measure the particle (and plasma) currents entering the mask. A second isolated current return path was set up in place of the Cerenkov plate, through which the mask beamlet return current was measured using a Pearson coil. Since the area of the apertures is known, the averaged current density on the anode is approximately given by the total measured current divided by that area. Some estimate should be made as to whether any of the current is being captured by the mask apertures. To that end masks with very large apertures were used. Different apertures patterns could be used to investigate the currents at different radii. This implementation, proved to be quite noisy. A fast response time Faraday cup was also used in place of the isolated current return path. This Faraday cup was developed by Smutek [Smu86] using plans of Pellinen's [Pel70]. The direct measurement of particle current supplements the Cerenkov measurements.

3.2.3. Plasma Diagnostics

Diagnostics which concern the measurement of diode plasma properties are discussed in this section. The principal diagnostic technique used for the largest portion of this research was time-resolved plasma emission spectroscopy. A helium-neon laser deflection diagnostic has also been used to obtain some qualitative plasma information. Simple B-dot loops have been used to investigate diode RF emissions. A streak camera, open shutter camera and a pin diode have been used to obtain further information about diode plasma visible optical emissions.

Spectroscopy

Refer to Figure 3.6 and the following discussion for the experimental set up used for spectroscopy. The optical emissions from the plasmas in the diode chamber (a) were imaged with a lens (b) (plano-convex, focal length = 25.4 cm) onto the entrance slit of a spectrograph (c) via turning mirrors (d) and an initial collecting lens (e) (plano-convex, focal length = 60 cm). The spectroscopic equipment was located in a lead faced Faraday cage (f), necessitated by the x-ray and electromagnetic noise environment associated with

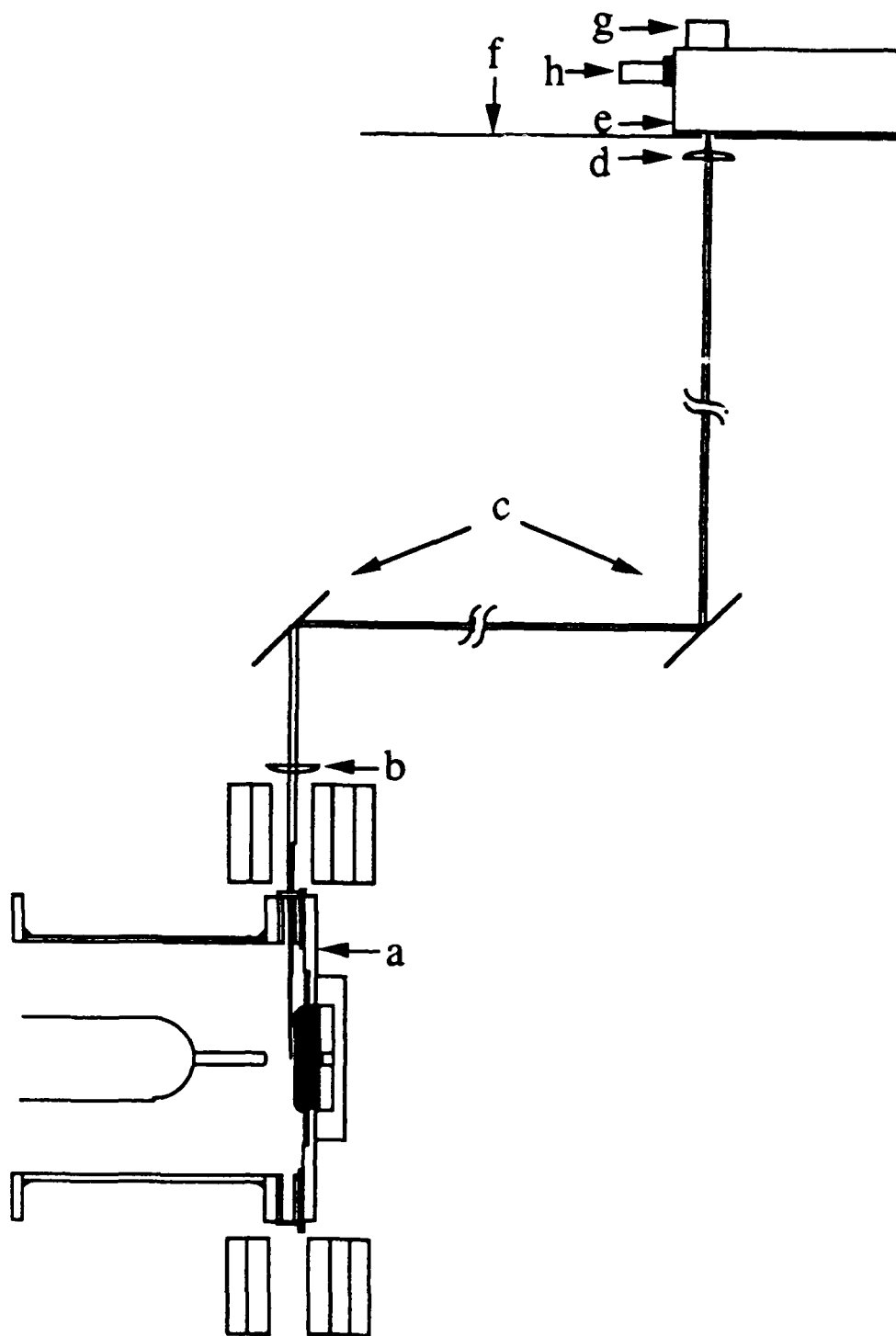


Figure 3.6. Experimental set up for spectroscopy, showing the diode chamber (a), collecting lens (b), turning mirrors (c), imaging lens (d), spectrograph (e), lead-faced Faraday cage (f), optical multichannel analyzer (OMA) (g), and the photomultiplier tube (PMT) (h).

pulsed power accelerators. The distance over which the optical signal was transported was about 13.5 m. There were two spectrographs available during different periods of this research. Initially a 0.275 m monochrometer (Jarrell-Ash Monospec 27) was coupled to a 1024 channel optical multichannel analyzer (OMA) (Tracor-Northern TN-6500 series, with 6100 series detector head, and 6130-1 pulse driver) (g). This configuration had maximum resolutions of about 0.7 and 1.4 Å per channel depending on the grating used (600 grooves/mm or 1200 grooves/mm). In practice this meant the system was able to resolve individual peaks when they were about 10 Å or greater apart. Although the individual peaks were often overlapping and identification was sometimes difficult due to the many species present, a broad spectral emission overview of about 750 Å or 1500 Å could be obtained. A 1-m monochrometer was obtained later in the investigations (Acton Research Corporation VM-510, Acton, MA). When coupled to the OMA maximum resolutions of about 0.2 and 0.4 Å per channel were possible, depending on the grating used. Spectral widths of about 200 - 400 Å were obtained. In addition to the use with the OMA, the Acton had a side port which was equipped with a uv-sensitive photomultiplier tube (sodium salicylate coating on the entrance window) (h).

The ability of the monochrometer to resolve individual peaks depended on the size of the initial slit. There was a tradeoff of spectrograph resolution versus total light intensity detected. Particularly for the smaller gate widths of 200 ns, the smallest slit widths were marginal as far as counts from detected light. Typical slit widths used were 200 µm, although some spectra were taken as low as 80 µm. The broad slits were often adequate for temperature estimates, if peaks were adequately separated, whereas the narrow slits were needed to perform density estimates from broadening. Tom Repetti has done calculations and measurements of the spectral system response which show that at 100 µm slit widths, a delta function spectral peak input (one of the Penray wavelength calibration lamps), will give about 5 channels width out (about 2 Å), the

minimum achievable. Any decrease in slit width below this results only in a loss of light and little increase in resolution. In these experiments the spectral resolution was dominated by the slit widths.

The OMA consisted of a 1024 channel, time-gateable, intensified, photodiode array. OMA gates could be set with arbitrary delay relative to some starting time. Gate widths as small as 100 ns could be obtained, however, in order to obtain higher signal to noise ratios, gate widths of 200-500 ns and larger were used. The gate-out monitor from the pulse driver, was routinely displayed on an oscilloscope with the accelerator voltage. Due to the rapid time-evolution of the processes in the diode, and the different physical processes that occur, the time-resolving ability of the diagnostic is quite important. Conclusions based on time-integrated spectra, or spectra obtained with long gates can be misleading. To correct for timing differences, the OMA gate is moved out 16 ns with respect to the voltage trace, a correction which is fairly unimportant for most spectra obtained due to the long time scales of interest. This number is obtained by comparing the delay of propagation for the electrical signal to the scope through 12.2 m of cable at 0.66c (61 ns), and the delay of light propagation along the slightly longer optical path of 13.5 m at c (45 ns).

The optical system was calibrated for relative peak height intensity with a calibrated irradiant standard, a tungsten filament lamp (Optronic Laboratories Inc., Model 245A, Orlando, Fla.). This accounted for the wavelength dependent response of the chamber windows, optics, gratings, and OMA detector diodes. The lamp was placed in the diode chamber and so was used to simultaneously align and calibrate the optics. This calibration was important for determination of temperatures from relative peak heights. In the case of the Jarell-Ash spectrograph, this was because the region of the spectra that was viewed was so wide, while for the case of ultraviolet spectroscopy with the Acton, because the diode sensitivity fell off with decreasing wavelength. After two years of operation, the diodes on the right side of the detector array (higher wavelength,

about the rightmost 100 channels) were discovered to have a reduced sensitivity by a factor of two relative to the left side. Intensity calibration now became particularly important. Spectral peaks of interest were positioned using the grating settings so that they fell outside this region. Calibration had an effect on relative peak height ratios by as much as a factor of 10 for widely spaced peaks in the ultraviolet. The detector diodes were calibrated for wavelength using a krypton, mercury or neon, low pressure gas discharge lamp (Oriel, models 6031, 6035, 6032) depending on the wavelength region being studied.

The optical axis for these experiments was typically aligned 0.1 cm off of the anode face, directly at the diode axis (112.5 cm). The anodes (normally Poco graphite, grade HPD-1) were extended into the transverse window field of view so that it could be observed directly across its face, at presumably the most dense part of the plasma. In some early experiments, plasma could only be viewed about 2 cm off the anode face; measurements gave very low intensity light emissions from principally molecular components. Those early experiments also showed the importance of shielding the window from incident electron flux, so as to avoid the increase in continuum due to Cerenkov radiation. As discussed above, in section 3.1.2, the windows are located in a flange designed to shield them from the electron flux. The windows employed in the earliest visible spectroscopy experiments were acrylic and had a cut off for transmission below about 3800 Å, which is readily apparent in those spectra. In spectroscopic studies below this cutoff, quartz windows and lenses were used. See section 4.3 for a discussion of the optical system spatial sensitivity.

He-Ne Laser Deflection

A laser deflection technique was also used to study time-resolved diode plasma behavior. This technique is sensitive to the index of refraction gradient of a fast-pulsed plasma [Enl87], and can be used to obtain the line density at a particular axial location as a function of time. Since the index of refraction of plasma is opposite in sign to that of neutral material the overall composition can also be determined. Calculations show that the sensitivity of this diagnostic compares very favorably with both schlieren photography and holographic interferometry [Enl87].

The experimental configuration for the deflection diagnostic, is shown in Figure 3.7. Refer to that figure in the discussion which follows. The basis for the method is a very fast differential amplifier circuit (b) connected to a photodiode quadrant detector (Silicon Detector Corporation SD-380-23-21-051). Opposite pairs of quadrants are shorted and the circuit is designed so that the output from the amplifiers is proportional to the deflection of the laser beam (c) from an initial zero position. A 5 mW He-Ne laser (Jodon HN-2SHP) is directed across the face of the extended carbon anode in the diode chamber (a) at distances from 0.1-0.4 cm. The laser and circuit are mounted on micrometers (d) to aid in zeroing the initial signal, for calibration, and for scanning measurements in the axial direction. As setup for these experiments, the deflection is due to axial gradients. Note that the diagnostic could also be setup to detect radial gradients. To maximize sensitivity to the He-Ne laser beam, a He-Ne line filter is used. The beam is diverted in a turning mirror (e) so that the photodiode detector is out of line of sight from the diode windows. The circuit was located a distance of about 1 - 1.5 m away (distance measured along the laser path) from the center of the diode, in a lead bunker (f) to shield the photodiode and active circuit elements from x-rays. A distance of about 3 m, gives the most sensitivity, which is a combination of total angular deflection and laser power density incident on the photodiode quadrant detector.

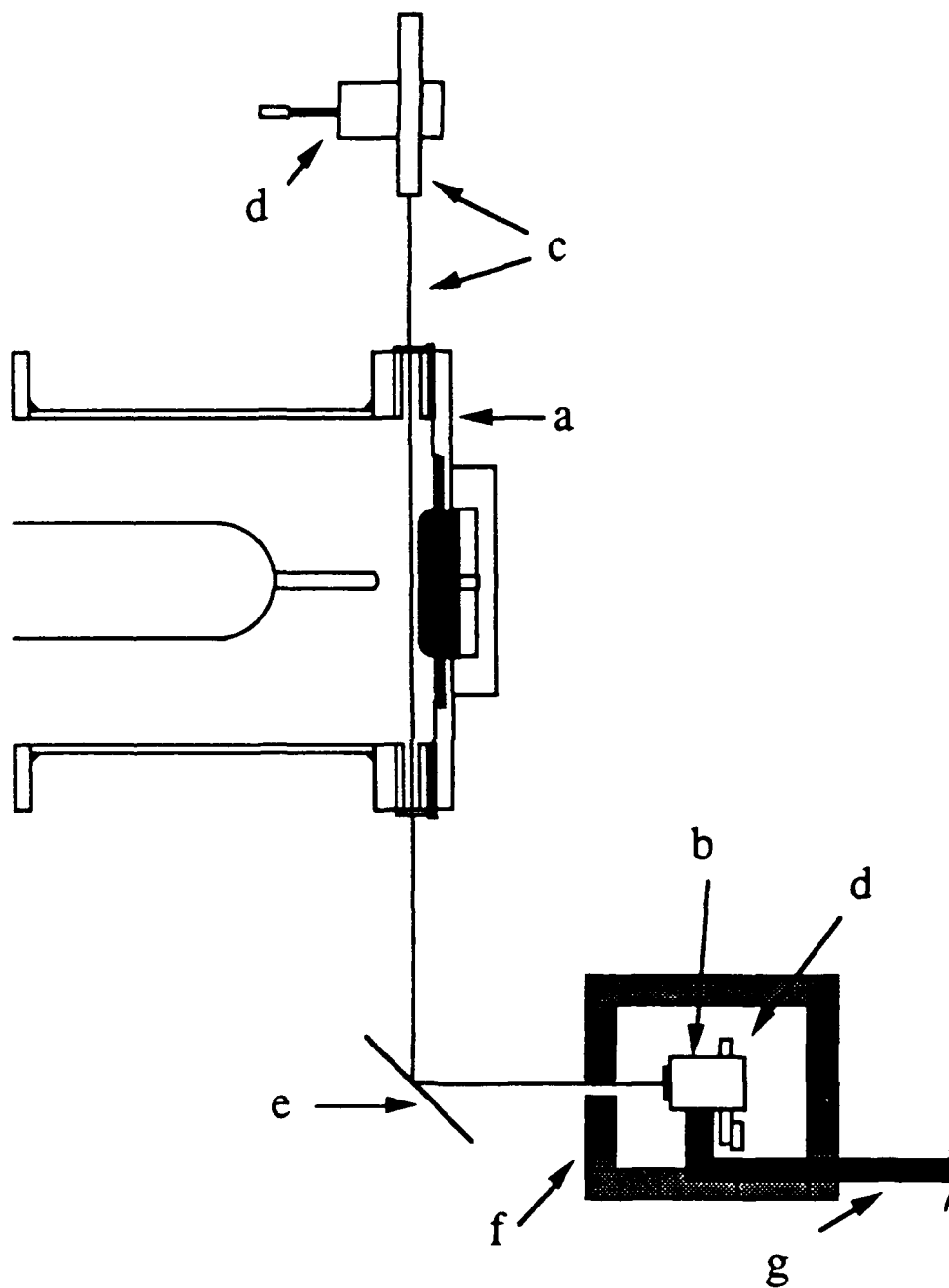


Figure 3.7. Experimental configuration for He-Ne deflection showing the diode chamber (a), fast differential amplification circuit (b), 5 mW He-Ne laser and beam (c), micrometers (d), turning mirrors (e), lead wall (f), and ground shield for signal cable (g).

RF Diagnostics

The transverse windows allowed observation and measurement of the RF emission escaping from the diode chamber. The cutoff frequency for the dimension along the beam axis (1.27 cm) was 1.0 GHz, while for the long dimension transverse to the beam axis (14.0 cm) was 10.1 GHz. The radiation was observed with B-dot loops. The signals were either transported to an calibrated S-band microwave detection system [Luc88] in a calibrated RG-8 cable or transported to the screen room in RG-58 and displayed on an oscilloscope using a simple RF rectification circuit. The signals could also be analyzed with a calibrated band pass analyzer circuit [Luc88] for frequencies below 400 MHz.

Miscellaneous Diagnostics

Also used for further diagnosis of the plasmas in the diode are a streak camera, pin diodes and open shutter cameras. Further information about beam profile was obtained from an x-ray pinhole camera.

4.0 Experimental Results

4.1 Optical and Ultraviolet Spectroscopy of Electron

Beam Driven Plasmas

The plasma produced in the diode was investigated with emission spectroscopy as described in section 3.3.3 in both crowbarred and non-crowbarred shots in the ultra-violet (180 - 350 nm) and visible (350 - 650 nm) region of the electromagnetic spectrum. Emission spectroscopy was also performed on shots which had an applied axial magnetic field. Time resolved as well as time integrated spectra were obtained. Through calibration studies it was determined that the region approximately 2mm in front of the anode surface was observed. Note however that light from a cathode plasma could be reflected from the face of the anode and into the field of view of the collection optics making it difficult to identify the origin of the plasma light. Line identification of the collected emission spectra was made by comparing the observed lines to those tabulated by Strignakov¹ for atomic emission and Pierce² for molecular species.

Time resolved emission spectroscopy of crowbarred shots before diode shorting had occurred revealed emission from molecular carbon (the Swan and Deslandres systems) as well as CH, CII (singly ionized carbon) and H β (Figure 4.1). These species are typical components expected from hydrocarbon impurity 'cracking' and may have originated from cathode or anode surface impurities. The average charge state of the observed material is quite low, with much molecular emission observed both before and after shorting. Figure 4.2 shows the resulting spectrum taken during and after shorting. No cathode material (brass or aluminium) was ever detected for crowbarred shots. This may mean that the cathode and/or anode plasmas are formed primarily from surface impurities, or that emission from the metal cathodes was not bright enough to be detected.

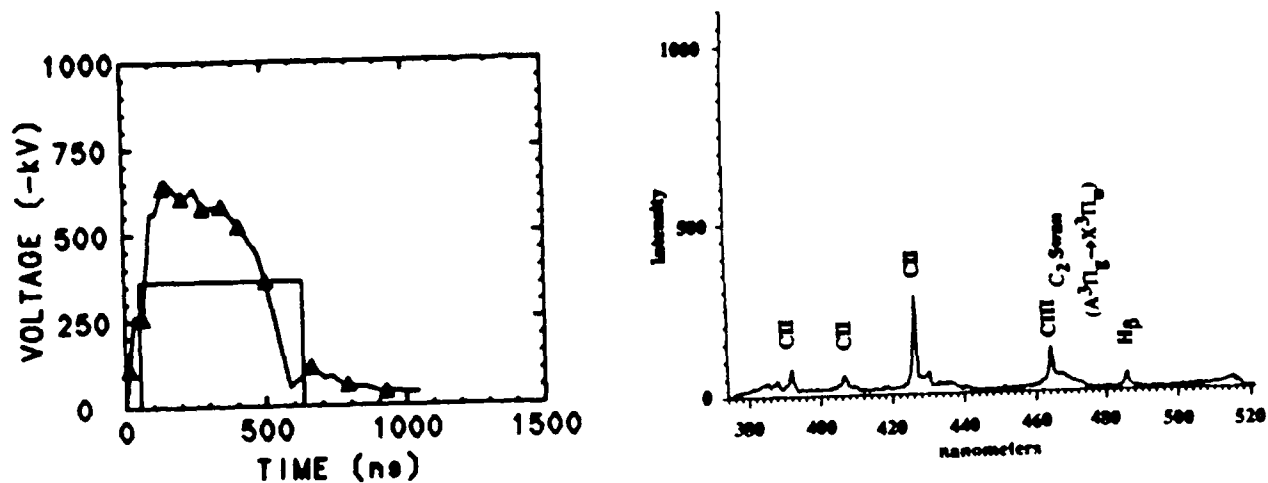


Figure 4.1 Data from a shot crowbarred before RF emission including the voltage with the OMA gate and the spectra obtained with the OMA gate before diode shorting

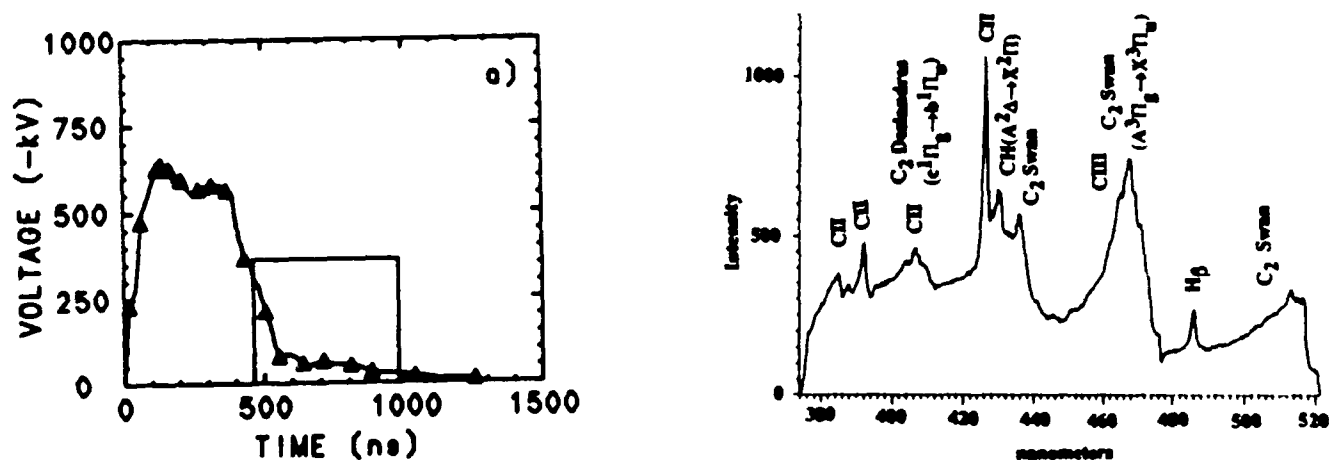


Figure 4.2 Data from a shot crowbarred before RF emission including the voltage with the OMA gate and the spectra obtained with the OMA gate during/after diode shorting.

(In general however, even small amounts of metal impurities result in very bright metal line emission.)

Spectra obtained during time integrated (0 - 2 μ s) wavelength scan of non-crowbarred shots revealed bright emission from a highly ionized plasma, with charge states AlI, AlII, AlIII, AlIV, CI, CII, CIII, and CIV over the range of 180 to 420 nm (Figure 4.3). Initially, time resolved emission studies in the visible (360 nm to 600 nm) in time gates of one microsecond generally resulted in negligible amounts of light produced in the first microsecond followed by a plasma consisting of mainly CII and CIII which cools and recombines to form neutral carbon (Figures 4.4 and 4.5). A time resolved study of the ultra-violet region of the electromagnetic spectrum on the other hand indicated that CIV emission dominated during the first microsecond (Figure 4.6). The CIV line at 252.9 nm first occurred at about 500 ns (diode shorting), peaked sharply between 750 and 900 ns and decayed rapidly in less than 200 ns. This line did not reappear as might be expected if the plasma was ionized past CIV and cooled off later in time. As CIV diminished, CIII and CII increased. Note that the appearance of CIV coincides with the appearances of voltage peaking and strong RF emissions (to be discussed in the following section) which signifies a beam-plasma instability and more efficient coupling of beam energy to the plasma through collective effects³ or more probably due to RF enhanced ionization.⁴

A more careful time resolved study of the light emission in various wavelength regions was performed and the results are summarized in Figure 4.7. Figure 4.7a shows a comparison of the time behavior of the peak intensities of the CII line at 358.7 nm and 359.1 nm and the CIII line at 360.9 nm. Figure 4.7b shows the time behavior of the H α line at 653.2 nm and two CII lines at 657.6 nm and 658.1 nm. Figure 4.7c shows the time behavior of CI at 566.9 nm, CII at 564.8 nm, CIII at 569.6 nm and CIV at 580.1 nm. Finally, Figure 4.7d shows the time behavior of CII at 283.6 nm, CIII at 269.8 nm and CIV at 252.9 nm. The time points are plotted at the midpoints of the nominally 200 ns wide OMA gates, and referenced to the start of the voltage pulse. Note that each of these data points were obtained with a single shot. Each figure was obtained with a single run which used the same calibration and optics alignment. Depending upon the wavelength regime, aluminum ions were not observed until after 800 - 1000 ns, which is long after predicted

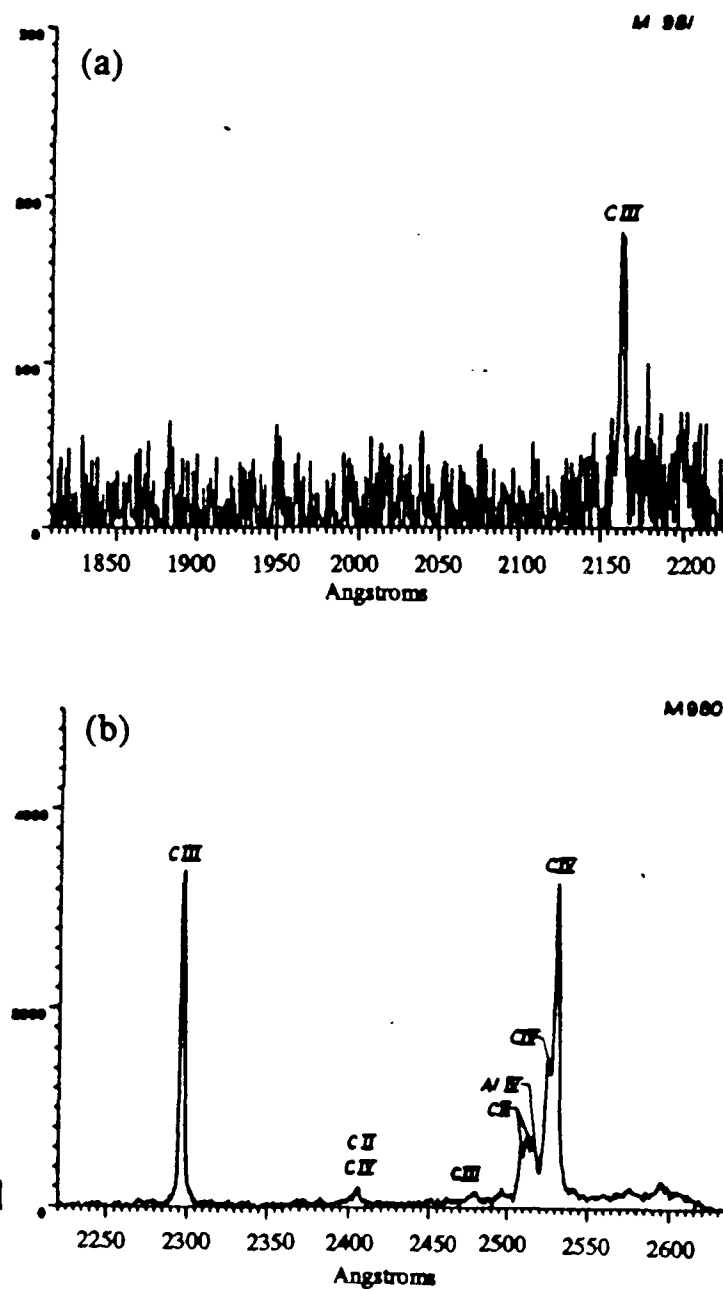


Figure 4.3 A time-integrated wavelength scan from 0 - 2 μ s on non-crowbarred shots.

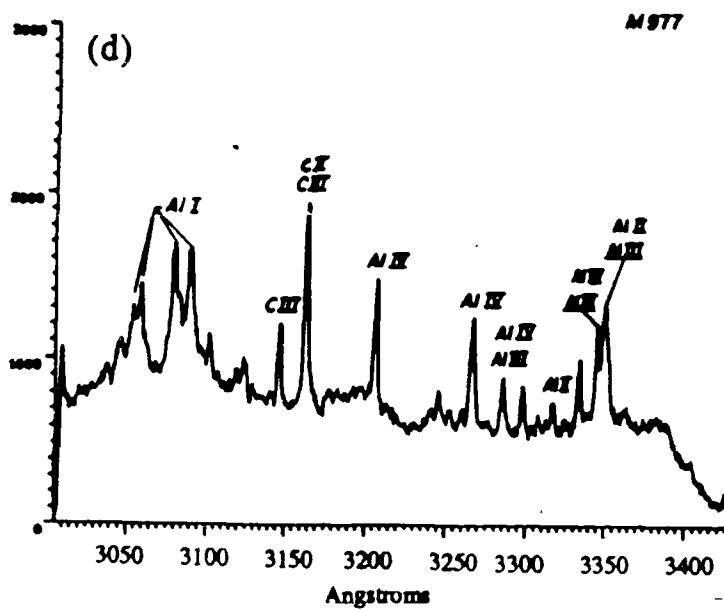
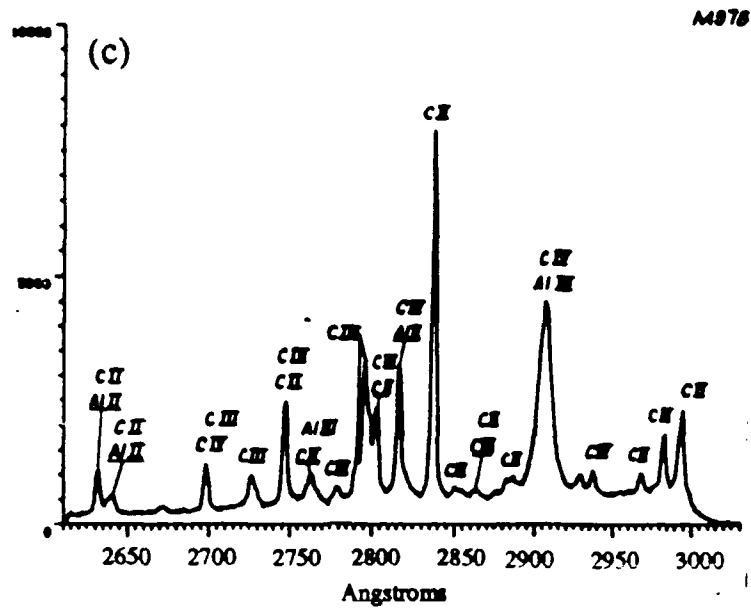


Figure 4.3. (continued).

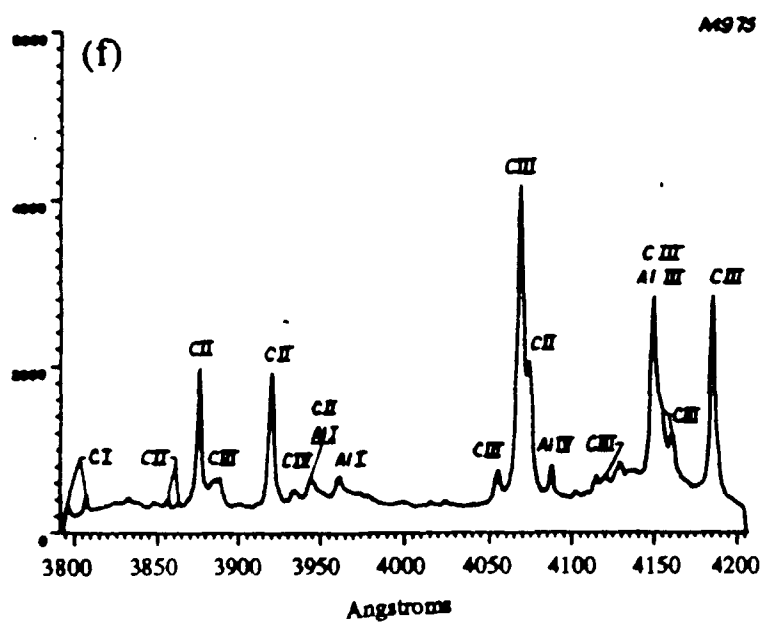
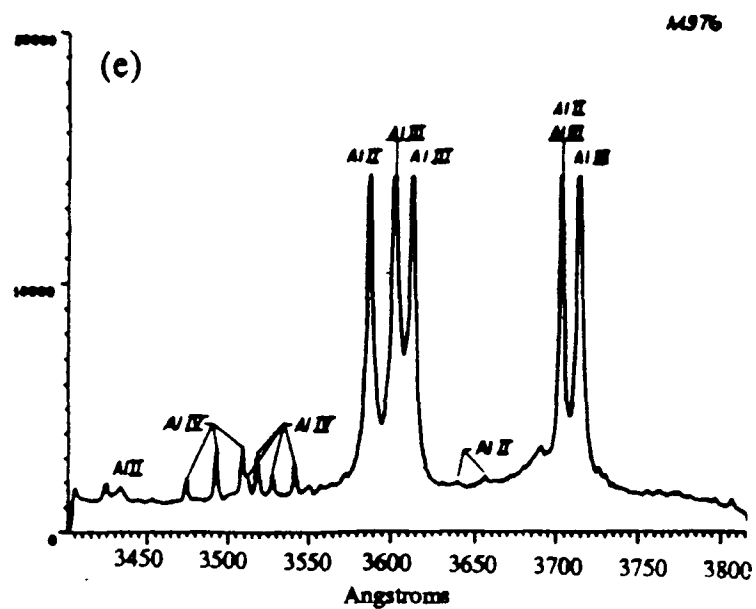
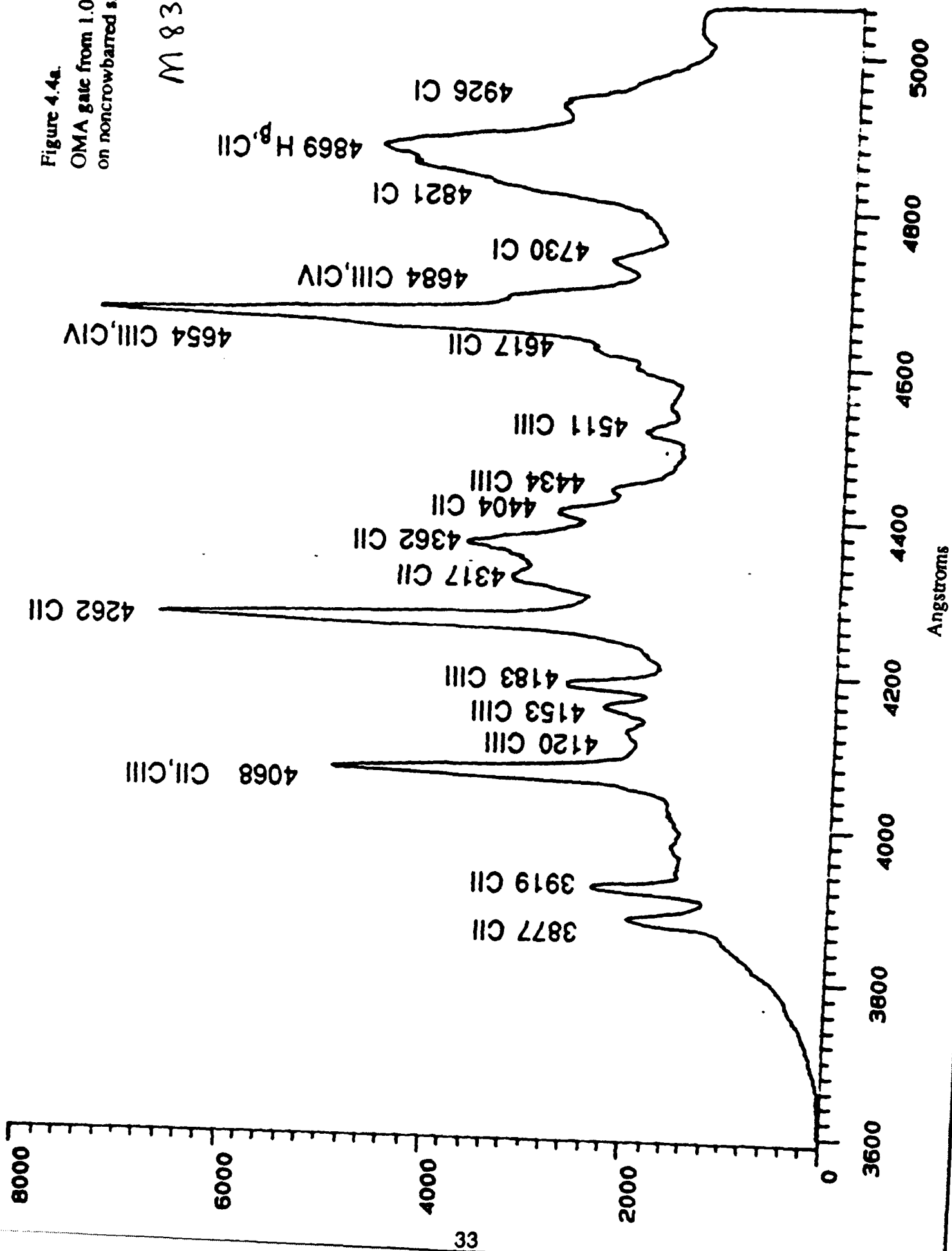


Figure 4.3. (continued).

Figure 4.4a.

OMA gate from 1.0-1.95 μ s
on noncrowbarred shot

M 835



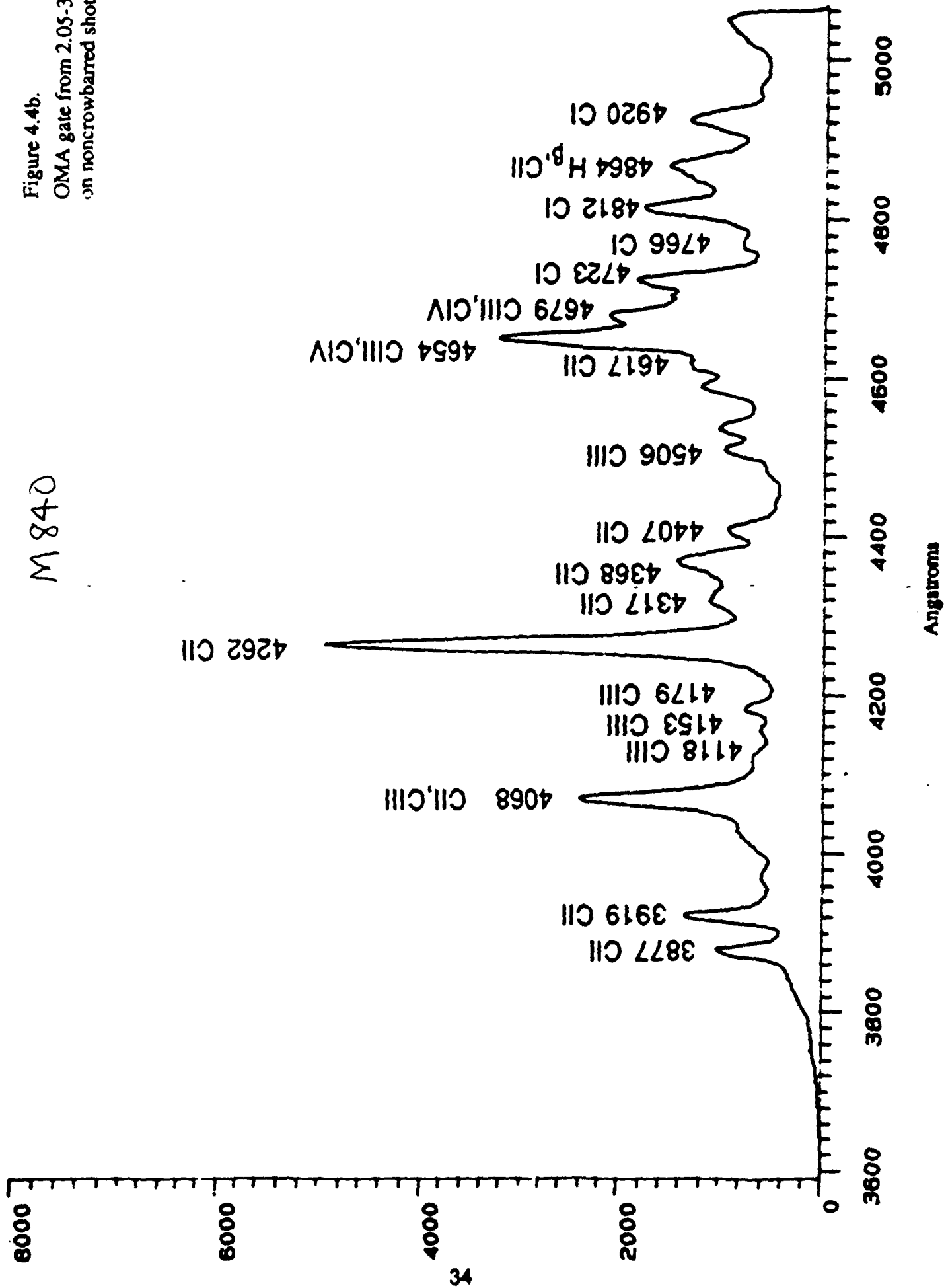


Figure 4.5a.

OMA gate from 1.05-1.95 μ s
on noncrowbarred shot

M836

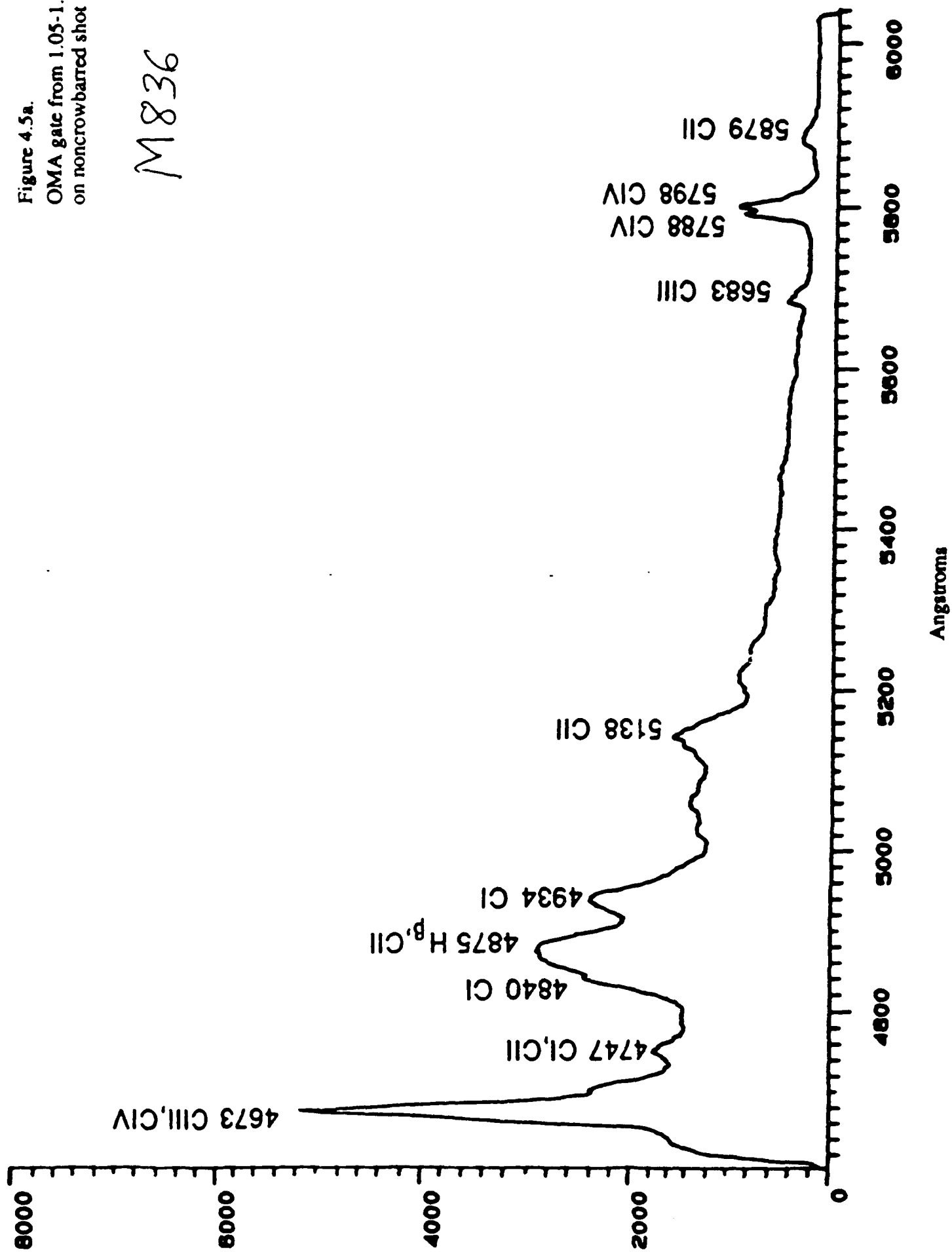


Figure 4.5b.

OMA gate from 1.95-2.95 μ s
on noncrowbarred shot

M837

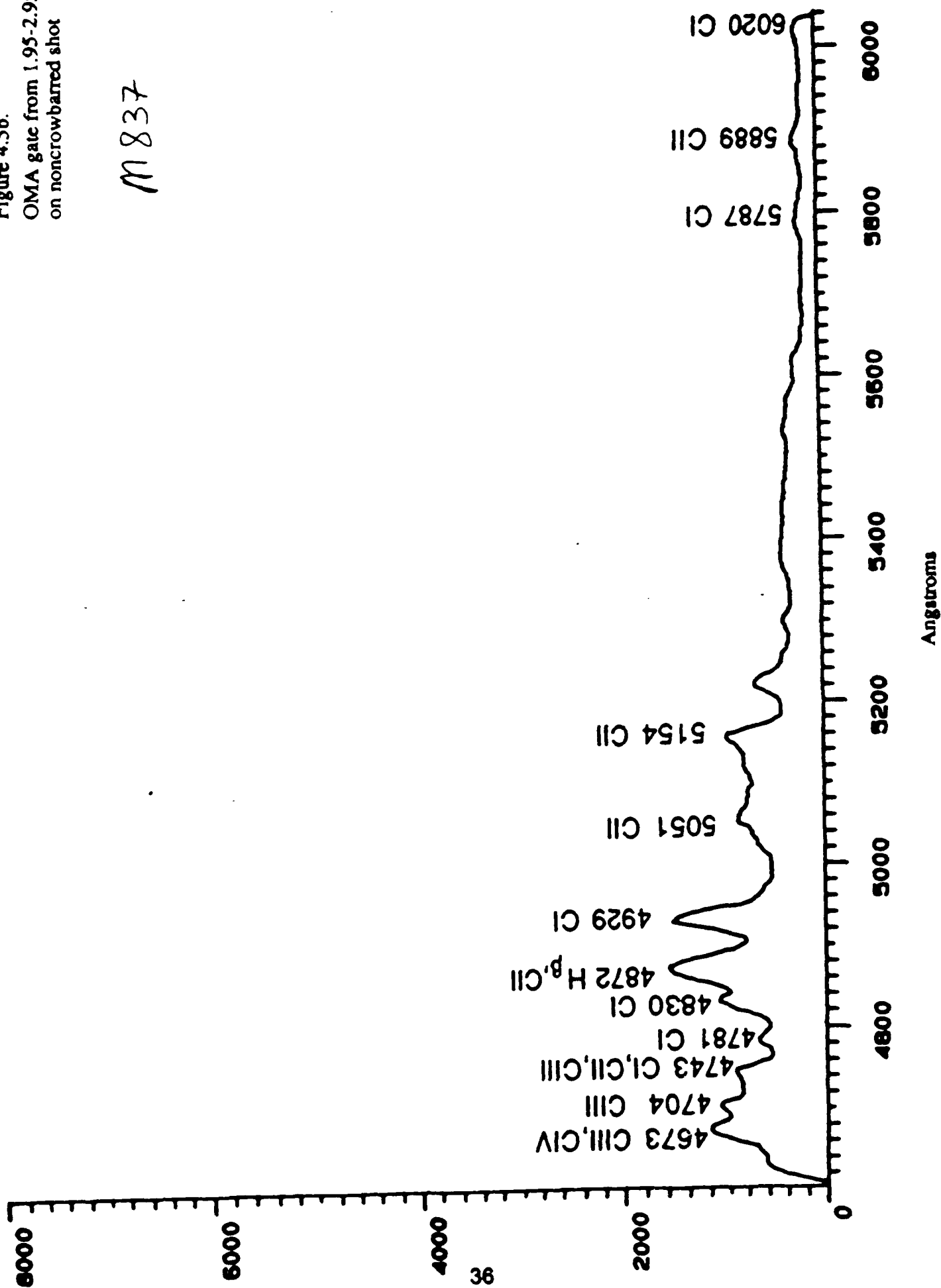
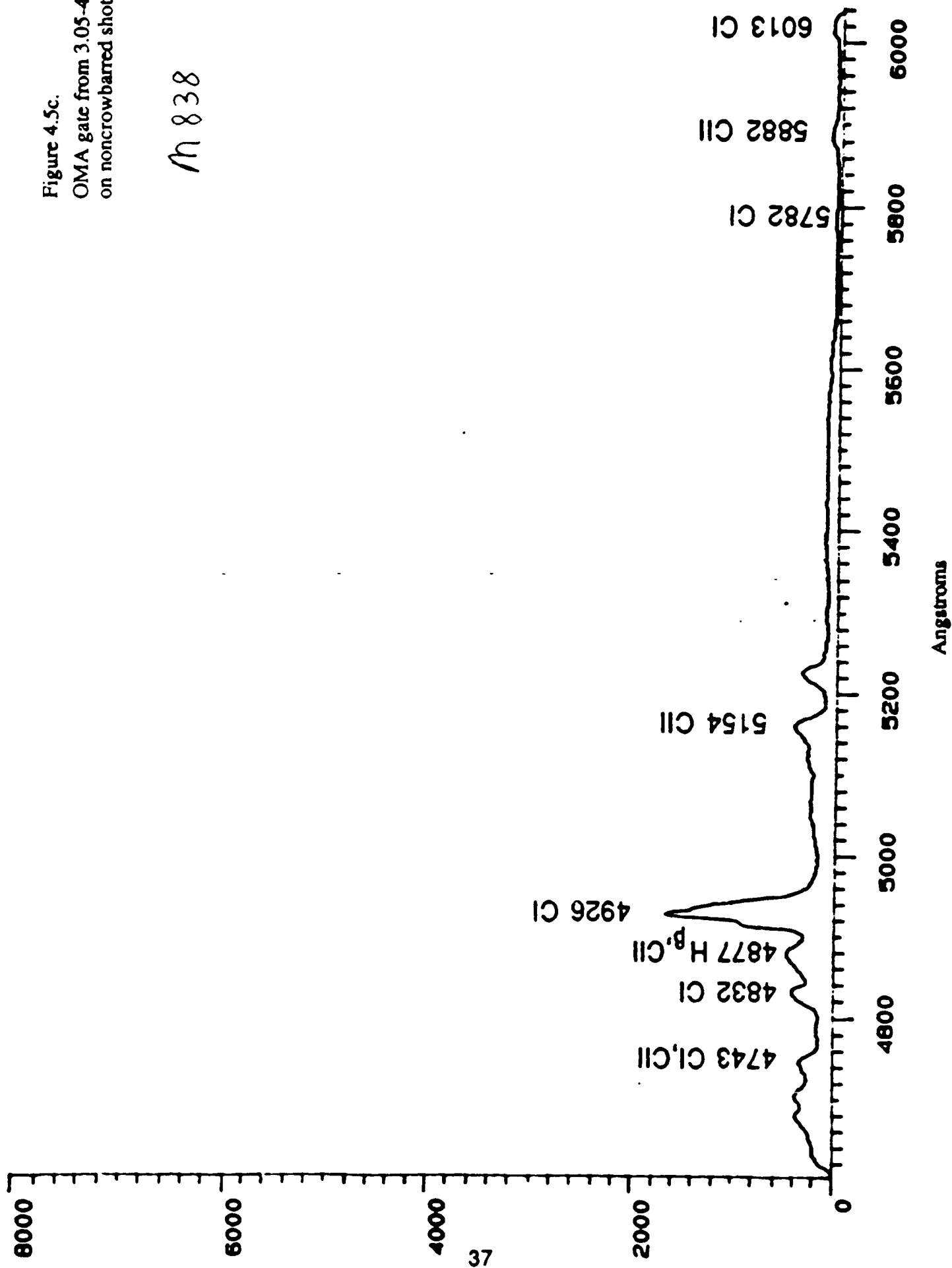


Figure 4.5c.

OMA gate from 3.05-4.05 μ s
on noncrowbarred shot

M 838



TIME STUDY OF 2400 - 2600 Å (130 ns gates)

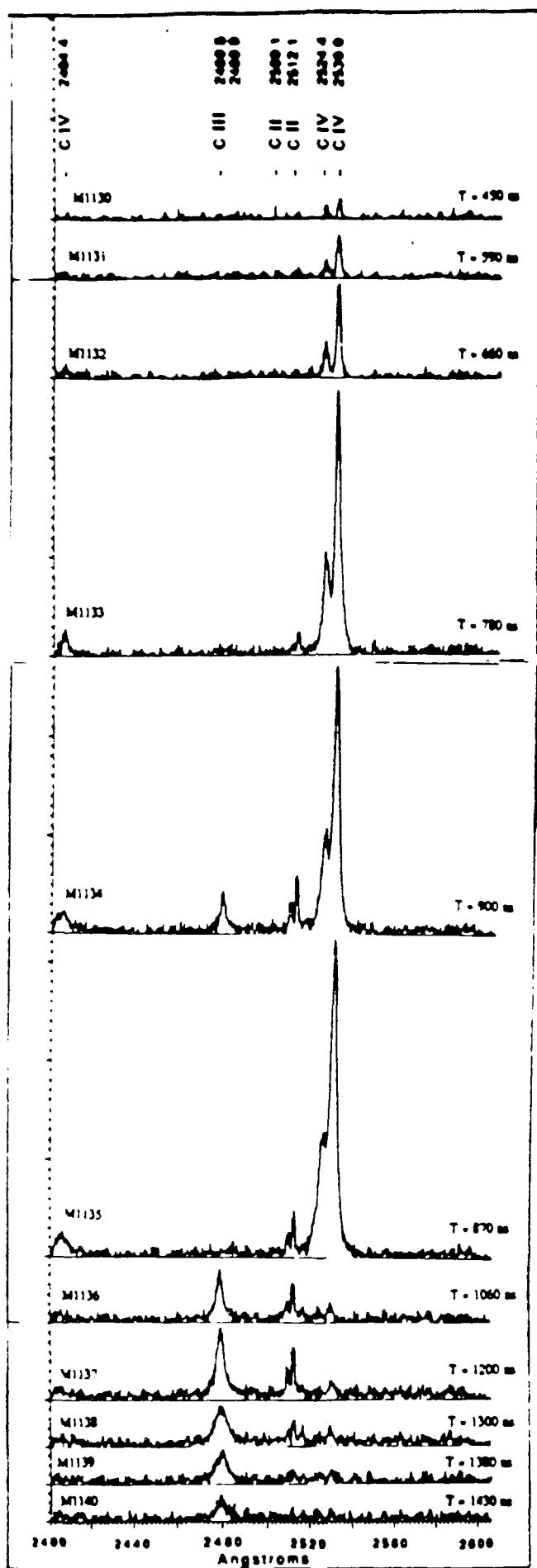


Figure 4.6 Time resolved study of the ultra-violet emission from $t = 0.24 \mu\text{s}$ to $t = 1.43 \mu\text{s}$ with 130 ns wide gates.

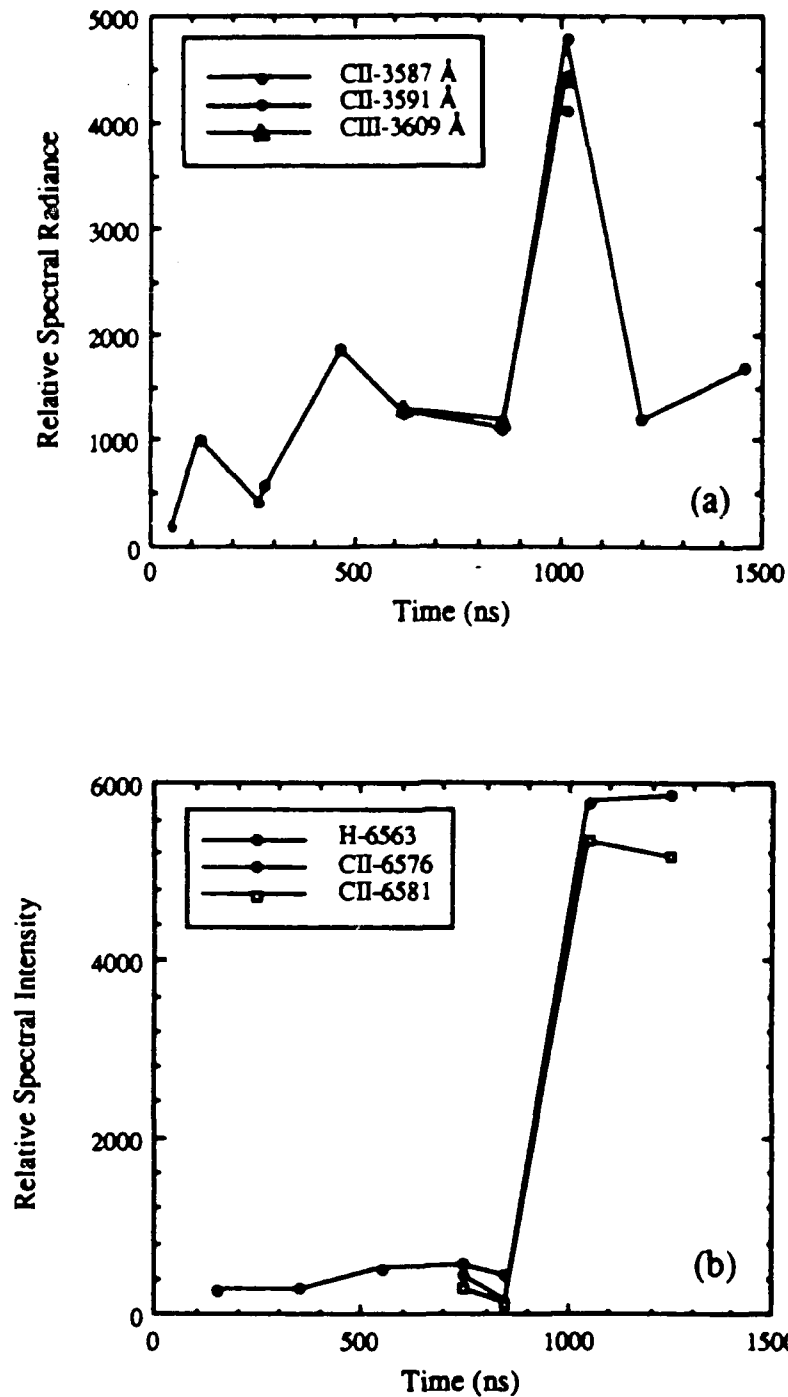


Figure 4.7 Time behavior of line emission of a) CII-3587 Å, 3591 Å, CIII-3609 Å, b) H α at 6563, CII-6576 Å, 6581 Å, c) CI-5669 Å, CII-5648 Å, CIII-5696 Å, CIV-5801 Å, d) CII-2836 Å, CIII-2698 Å, CIV-2529 Å. The points are plotted at the center of the nominally 200 ns wide OMA gate, and referenced to the start of the voltage pulse.

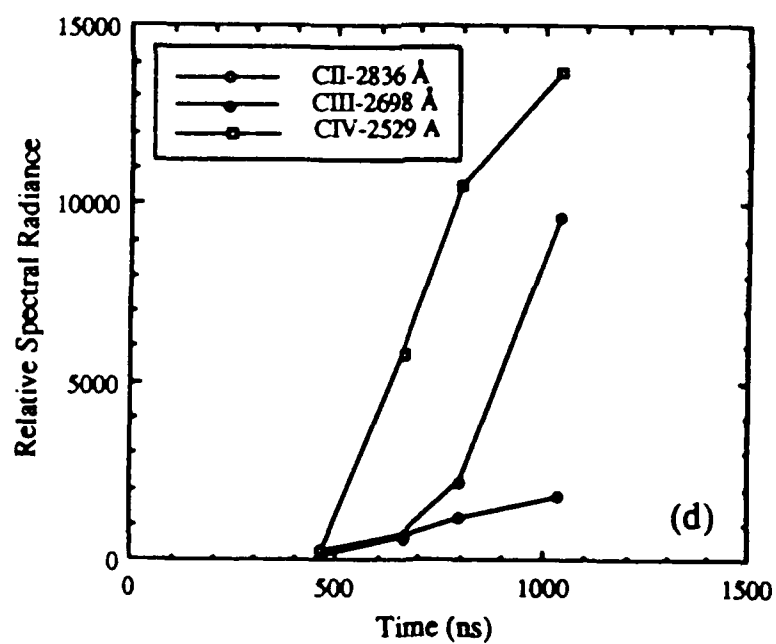
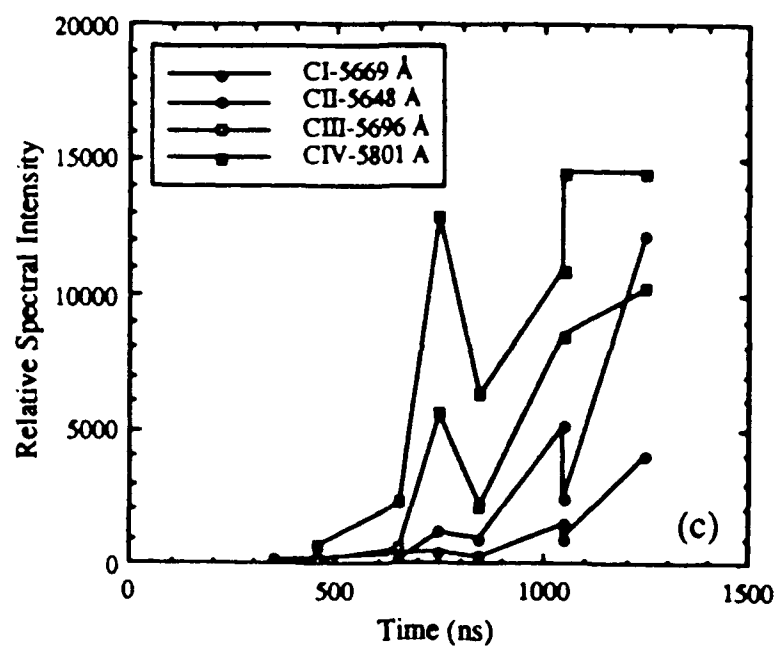


Figure 4.7. (continued).

shorting times. In general, CII and H were observed immediately upon the application of the voltage pulse, probably due to light reflected from the cathode off of the diode chamber walls. CIII and CIV ions were not observed until approximately 400 ns at the onset of voltage peaking (to be discussed in the next section) and RF emission from the diode. Note that the hydrogen line emission was observed at the beginning of the voltage pulse, again probably originating from cathode plasma whose light was reflected into the field of view of the optics. The H_{α} intensity was constant within a factor of two for the first 900 ns of the voltage pulse where at that point the overall light output jumped by more than an order of magnitude and H_{α} was observed as an absorption peak in the very broad nearby CII line.

The line intensities of various carbon lines, ionization state CI through CIV obtained in a time study of the region 560 to 600 nm is shown in Figure 4.7c. Although CII emission is observed as early as 350 ns, emission from CIV does not start until about 450 ns, when it then rapidly increases. Later in time, there appears to be an overall cooling of the plasma since the intensities of the lower ionization states are increasing in intensity relative to the higher ionization states, although the total overall optical emission did increase. Although the spectra show the coexistence of highly ionized states of carbon and atomic hydrogen, the plasma may be quite large radially, and the lower ionization states could be detected from a cooler plasma further out in radius, toward the edge.

From the observations of primarily hydrocarbons in the crowbarred shots, and the observation of CII and H_{α} early in non-crowbarred shots, the most likely conclusion is that the emission detected is due to impurities on the cathode and anode. According to the results of the laser deflection diagnostic, discussed in the following section, the plasma observed during the period from 400 ns to 600 ns may be due to a fast, on-axis cathode plasma, streaming across the gap. As mentioned earlier, the spectra obtained during this period (which also coincides with voltage peaking and RF emission) reveal a high average charge plasma, with the primary emission due to CIV, CIII and from CII. There are two hypotheses as to the source of the high ionization state plasma. The first is that a low effective charge plasma is being ionized by the large currents

obtained at shorting. However, these states would be expected to occur in the case of crowbarred shots as well since the differences in total current between crowbarred and noncrowbarred shots after shorting is only a factor of 2 to 6. The second hypothesis is that the high ionization states are due to a beam-plasma instability or due to the interaction of the RF with the plasma. The exact cause of the high ionization state plasma is still being investigated.

Temperature estimates can be obtained from time-resolved spectra obtained in the ultra-violet wavelength regime, Figure 4.6, from a comparison of the line ratios observed with a Collisional Radiative Equilibrium (CRE) code.⁵ The two lines which have initially been used to estimate the temperature occurred at 229.6 nm (CIII) and 252.5 and 253.0 (CIV). These lines were chosen because they could be obtained using the same grating setting on a single shot and represented persistent, intense lines. The results from the code have been given for the ratio of the expected intensities of the sum of the two CIV peaks to the expected CIII line intensity for a range of densities and temperatures. The calculations are shown in Figure 4.8. A time resolved study of these lines showed that the relative intensities did not change much with time and resulted in an approximate temperature of 7 eV in the density range of 10^{16} to 10^{18} cm⁻³. Note that this temperature did not change with the application of the magnetic field. This may be due to the fact that these lines originate from some part of the plasma which undergoes equilibrium quickly or it may mean that the population mechanisms of these lines is not dominated by the kinetics assumed in the CRE model but by some other physical mechanism such as cascade pumping by the relativistic electrons.

The broadening of particular lines such as H α can be used to estimate electron densities. Figure 4.9 shows the width of the H α line at various times. The largest line width indicates an upper density of 10^{17} cm⁻³. Note that line broadening can be produced by the free electron density of the plasma and/or by the strong electric fields in the diode. The increase and decrease in the H α line may indicate different plasmas (cathode or anode) and different plasma regions which come into the viewing area of the spectrograph. These data are currently being investigated in light of the HeNe deflection data.

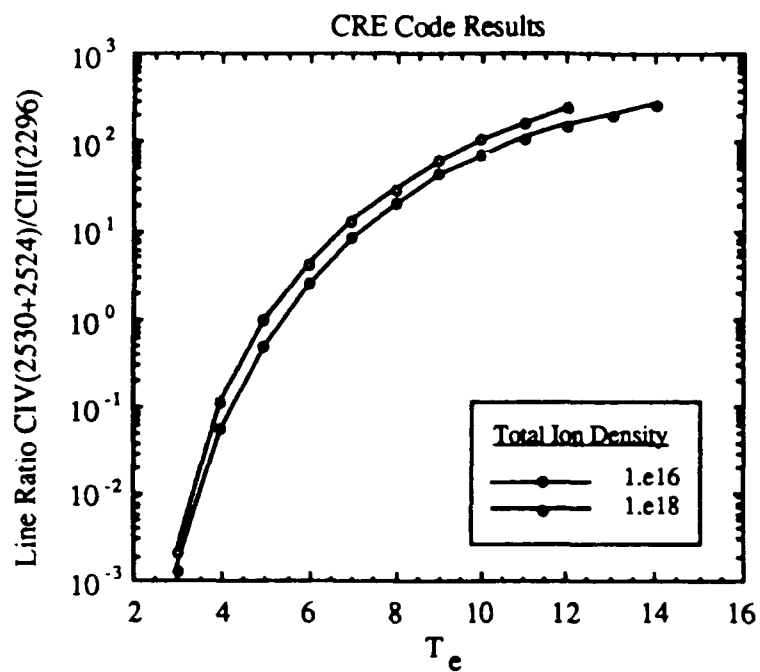


Figure 4.8 CRE code results for the ratio of line intensities for the sum of two CIV peaks at 2530 and 2424 Å, and the line intensity for the CIII peak at 2296 Å [Whe88].

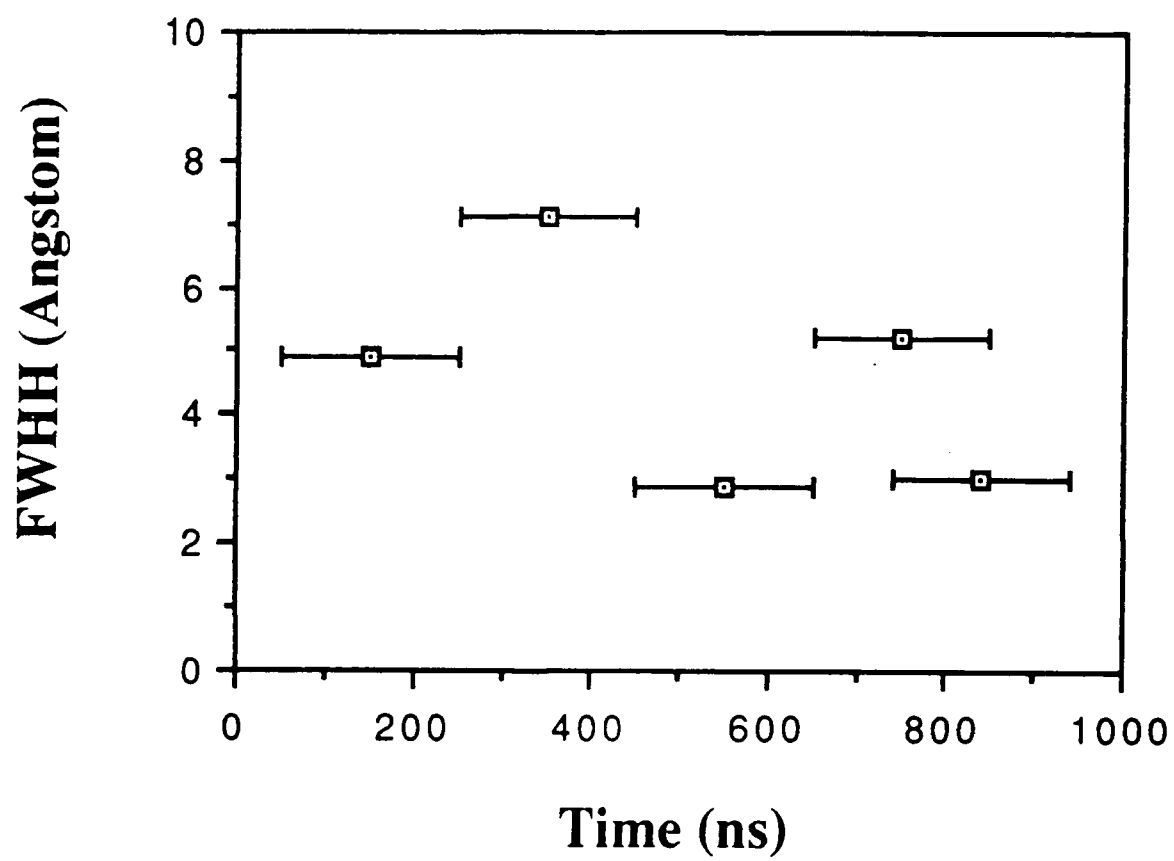


Figure 4.9. The full width at half height of the $H_{\alpha}(656.3 \text{ nm})$ as a function of time

Ultra-violet emission was observed during the presence of axial magnetic fields ranging from 500 to 920 Gauss, (Figure 4.10b). The spectra are similar to that observed without the magnetic fields, with two exceptions. The first is that the overall light intensity was about a factor of 2 higher than without the fields; the second is the presence of unidentified line emission between 255 to 265 nm. The line emission could be due to CII and CIII but the absence of lines in the same wavelength region originating from the same upper energy level is unexpected. The lines do not match with those of known impurities, such as cathode metals or hydrocarbons. We are currently investigating this unusual spectra.

In conclusion, emission spectra taken during the initial 400 ns period of the beam pulse, before crowbarbing or before the onset of RF emission in non-crowbarred shots showed a low effective charge plasma with primarily molecular components as well as atomic hydrogen and singly ionized carbon. This is probably due to hydrocarbon compounds found on the surface of the electrodes. After the first 400 ns in crowbarred shots, the spectra revealed a continuation of the low charge state plasma. At time greater than 400 ns in non-crowbarred shots where voltage peaking occurred, large amplitude RF emissions were detected at the same time that the spectra revealed a high average charge plasma with most of the emission originating from CIV, CIII and to some extent from CII. These highly charged states may be due to beam-plasma interactions or more likely due to interactions between the RF field and the plasma. At times well after diode shorting, the emission spectra revealed a cooling and recombining plasma. A comparison of the line intensities of various species compared to the CRE theoretical model indicates temperatures of about 7 eV. Emission observed during the application of axial magnetic fields was more intense than that without fields, and exhibited some unidentified spectral lines. Although nonequilibrium plasmas were generated in both the magnetized and unmagnetized cases, we are still analyzing data to determine whether a population inversion occurred.

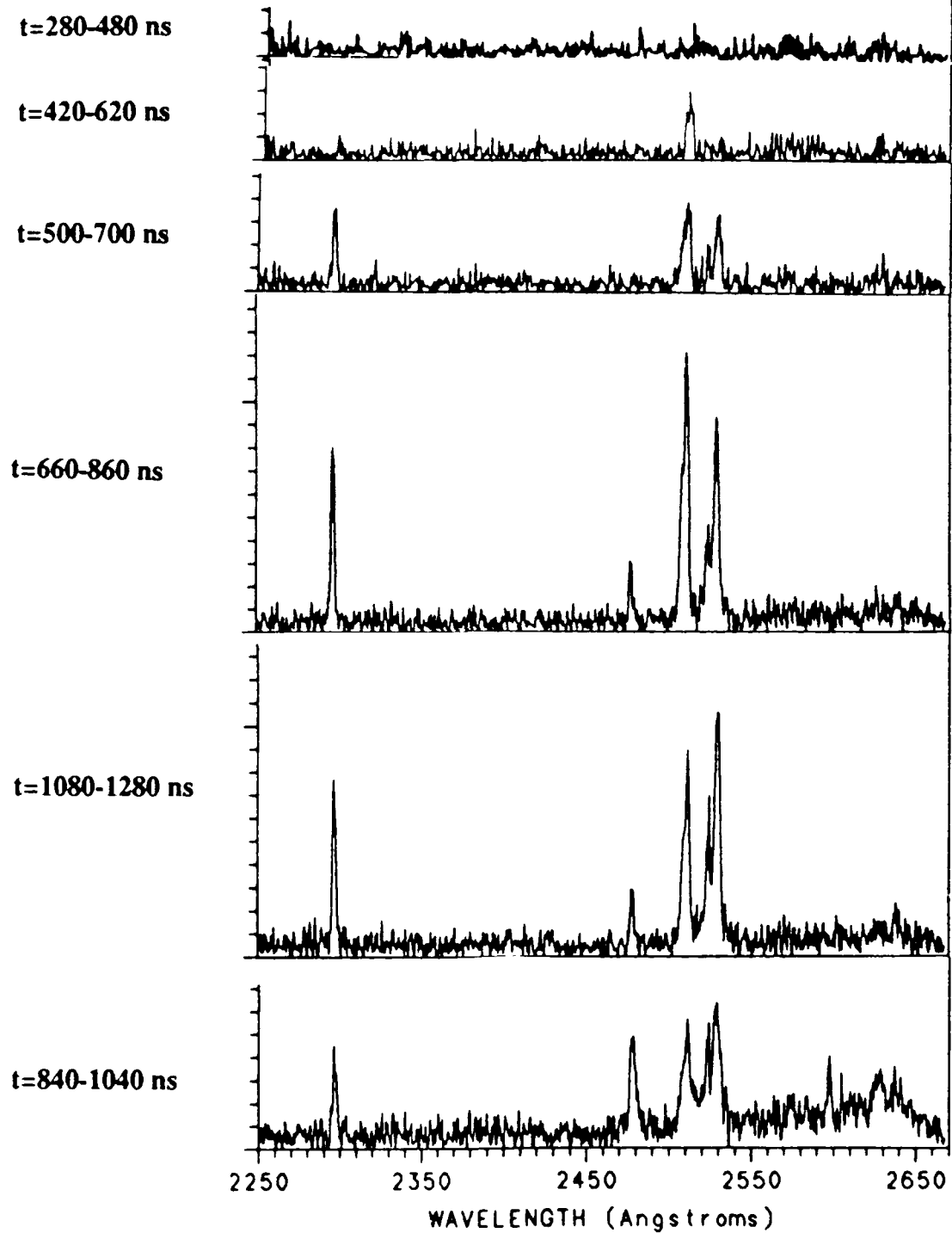


Figure 4.10a. Time resolved emission spectroscopy
with no magnetic field

$t=560-760$ ns

$t=660-860$ ns

$t=880-1080$ ns

$t=1060-1260$ ns

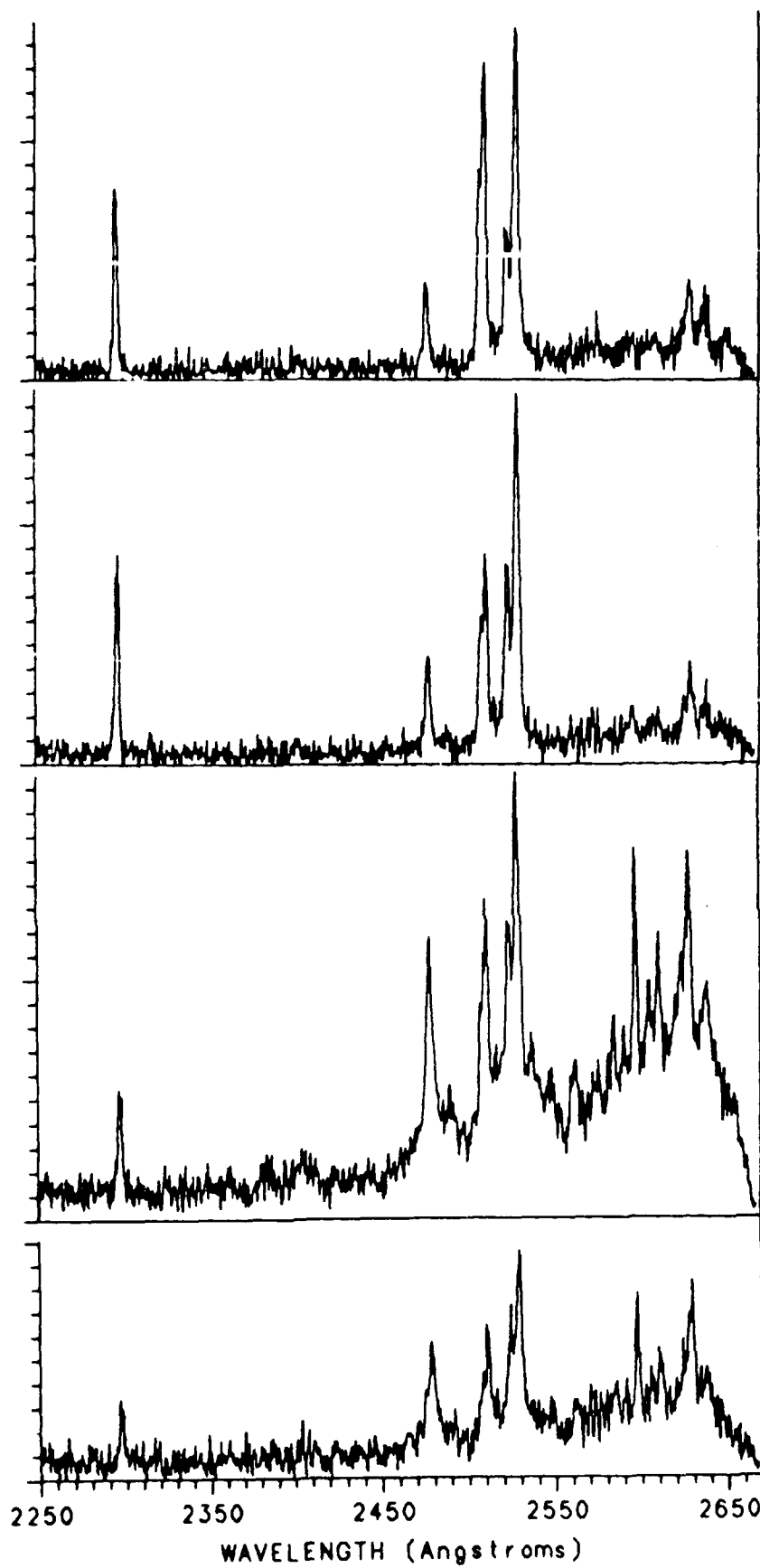


Figure 4.10b. Time resolved emission of plasmas with an axial B of 800 Gauss

4.2 Electron Beam Dynamics and Diode Plasma Physics

The behavior of the cathode and anode plasmas in the electron beam diode have a major effect on the electron beam energy deposition in the carbon plasma. Extensive diagnostic experiments have been performed in order to understand the plasma physics in the diode region of the MELBA generator during the electron beam irradiation of carbon anodes.

The electrical characteristics of the MELBA accelerator driving the short gap, low aspect ratio diode display 3 main types of behavior. The most prevalent type, occurring in over 95% of the shots is referred to as "voltage peaking", an increase in the voltage after about 400 ns to 600 ns. This voltage peaking phenomenon coincided in time with the generation of large levels of radio frequencies and emission from highly ionized carbon. Figure 4.11 depicts the experimental data for a typical shot. The voltage peaking behavior starts at about 500 ns in Figure 4.11 a, at which time the effective gap model in 4.11 d deviates from the experimental measurement. The B-dot current (I_D in Fig. 4.11 b) and the tube return current (I_A in Fig. 4.11 b, open circles) agree quite well for the first 400 ns. The difference between I_D and I_A is the current flowing radially to the walls of the diode chamber, and is displayed as I_W in Figure 4.11 b (closed circles). Before voltage peaking, differences of about ± 0.4 kA are well within the experimental error for these two diagnostics. Some of this current difference is due to stalk emission. After voltage peaking begins these two currents begin to disagree, (substantially at later times). Noticeable damage to the glyptol cathode coating indicates cathode shank emission. These two currents are used to calculate two diode impedances: Z_A - the anode impedance, and Z_D - the total diode impedance. The diode makes transitions through the Child-Langmuir phase, voltage peaking, then finally reaches a nearly constant impedance of about 16-20 ohms before shorting.

The effective A-K gap is found by plotting a linear best fit to $(1/P)^{1/2}$ where P is the experimental perveance ($I/V^{3/2}$). The extrapolation of the linear portion of the previous quantity gives a prediction of the diode shorting time or an *implied* closure velocity. We also define *apparent* closure velocity from diagnostics which observe the cathode plasma (such as laser deflection). *Effective* closure velocity is calculated from diagnostics which give an estimate of the shorting time (e.g. voltage shorting). Closure velocity data will be summarized later in this report.

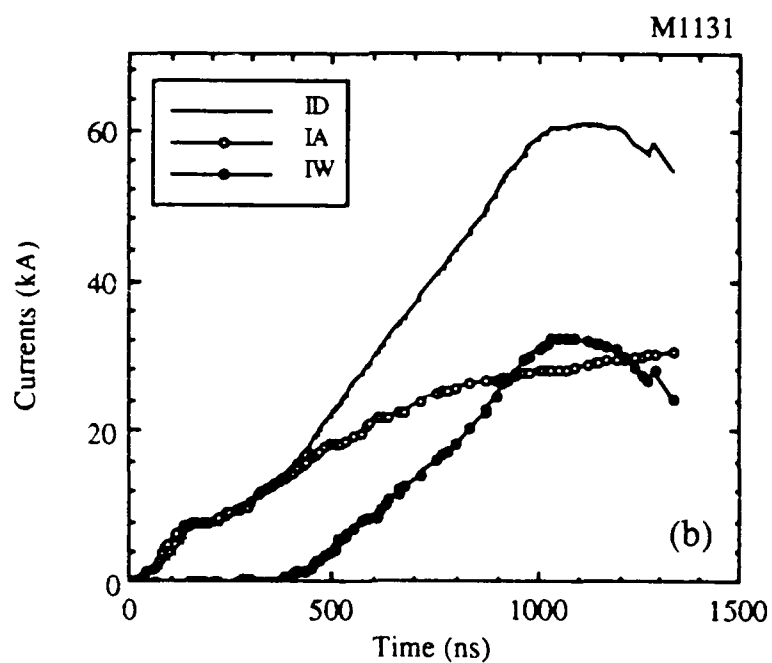
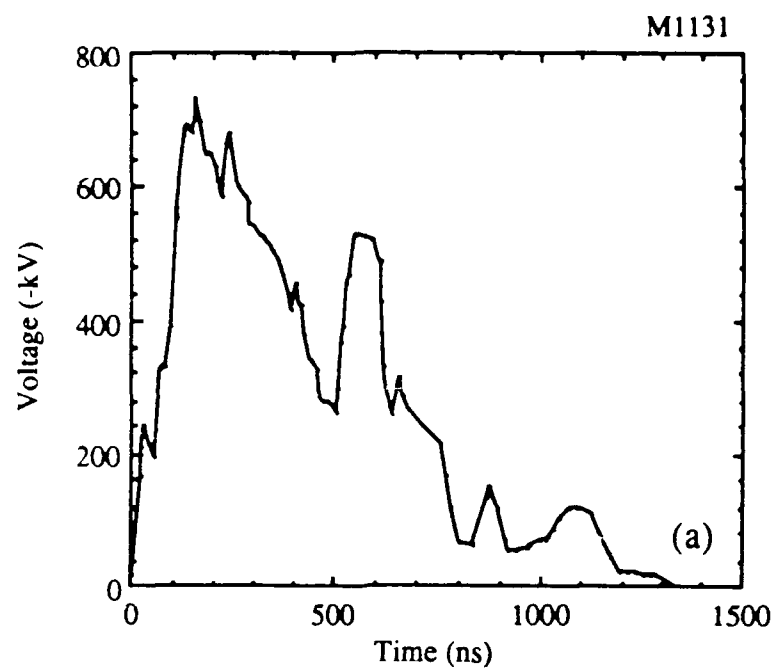


Figure 4.11. Data for 'voltage peaking' shot M1131 including a) voltage, b) B-dot (ID), tube return (IA) and wall (IW) currents, c) diode impedances using ID and IA, d) closure analysis with OMA gate showing regions of different behavior, e) carbon spectral line emission during OMA gate.

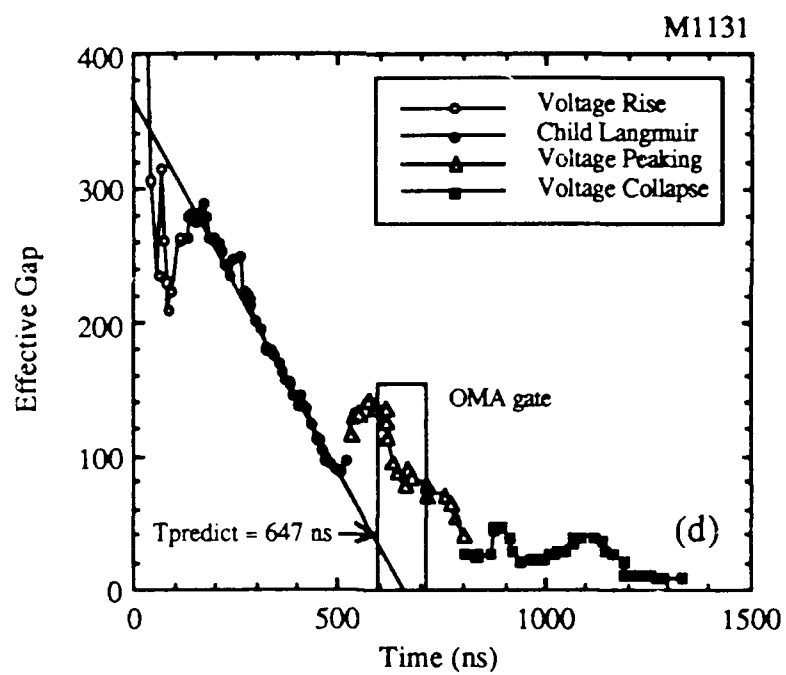
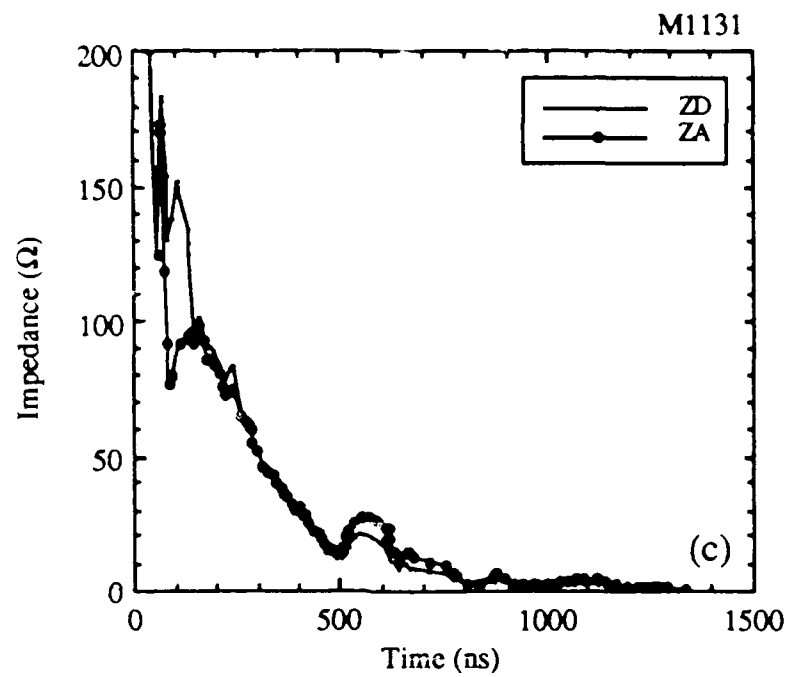


Figure 4.11.(continued).

Figure 4.12 gives oscilloscope traces for a number of shots, showing the significant levels of radio frequency and microwave emission which occurred primarily after the start of voltage peaking. This RF was also seen as a current modulation on the unfiltered B-dot probe. This strong RF emission was correlated with emission from highly ionized carbon in the absence of a magnetic field. We discovered that the application of a magnetic field reduced the level of RF, but caused even higher intensity of optical emission, an effect which is not totally understood at this time.

Temporally gated Cerenkov plate diagnostic data is shown in Figure 4.13. It can be seen that, during the initial 50 ns (during Child-Langmuir phase), the electron beam pattern was well defined on the Cerenkov plate. At 260 ns the beam appears to become nonuniform as if pinching or filamenting. By 520 ns (during voltage peaking and RF emission) the beam apertures are not recognizable, indicating a beam-plasma instability. At later times the beam begins to exhibit well formed beamlets on the outer edges.

The previous data can be related to the apertured beam monitor data shown in Figure 4.14. Again, the initial CL phase of the electron beam pulse shows increasing current, however, after about 200 ns the beam current shows a spikey nature that persists throughout the voltage peaking and RF phase. This provides further evidence of an e-beam-plasma instability in the diode. In the tail of the e-beam voltage pulse we see a low energy electron beam current which is effectively filtered out by a 200 kV foil filter.

Laser deflection diagnostic data provided the most direct measurements of plasma in the diode region. Typical data is depicted in Figure 4.15. Note that the data exhibits a positive deflection followed by a negative one, then finally a second positive deflection late in time. In the experimental configuration used, a positive deflection corresponds to net plasma gradients increasing towards the cathode (henceforth denoted cathode plasma) or net neutral particle gradient increasing towards the anode (hence anode neutral). A negative deflection corresponds to net plasma gradient toward the anode (anode plasma) or a net neutral gradient toward the cathode (cathode neutrals). Note that due to the relative contributions to the index of refraction this diagnostic is 10 times as sensitive to plasmas as to neutrals. The interpretation of this diagnostic is complicated by the fact that there may be two clumps of plasma (or neutrals) streaming in opposite

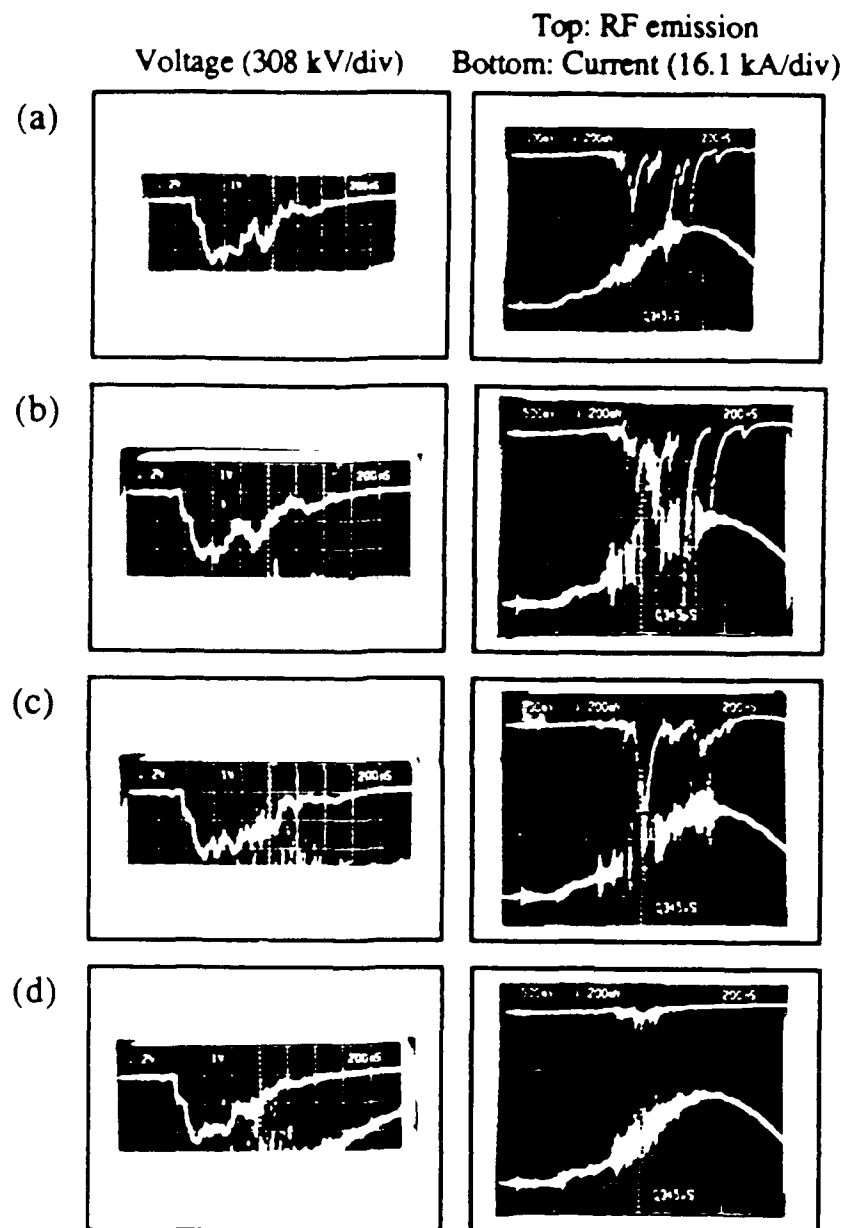


Figure 4.12. RF data from voltage peaking shots with voltage on left, RF emission and B-dot current monitor on right including the following cases: 20 MHz filtered B-dot, voltage peaking, no magnetic field (a), unfiltered B-dot, voltage peaking, no magnetic field (b), unfiltered B-dot, non-voltage-peaking, no magnetic field (c), unfiltered B-dot, voltage peaking, magnetic field case ($B \approx 900$ Gauss) (d).

Top: Voltage: 154 kV/div
Bottom: Camera Gate

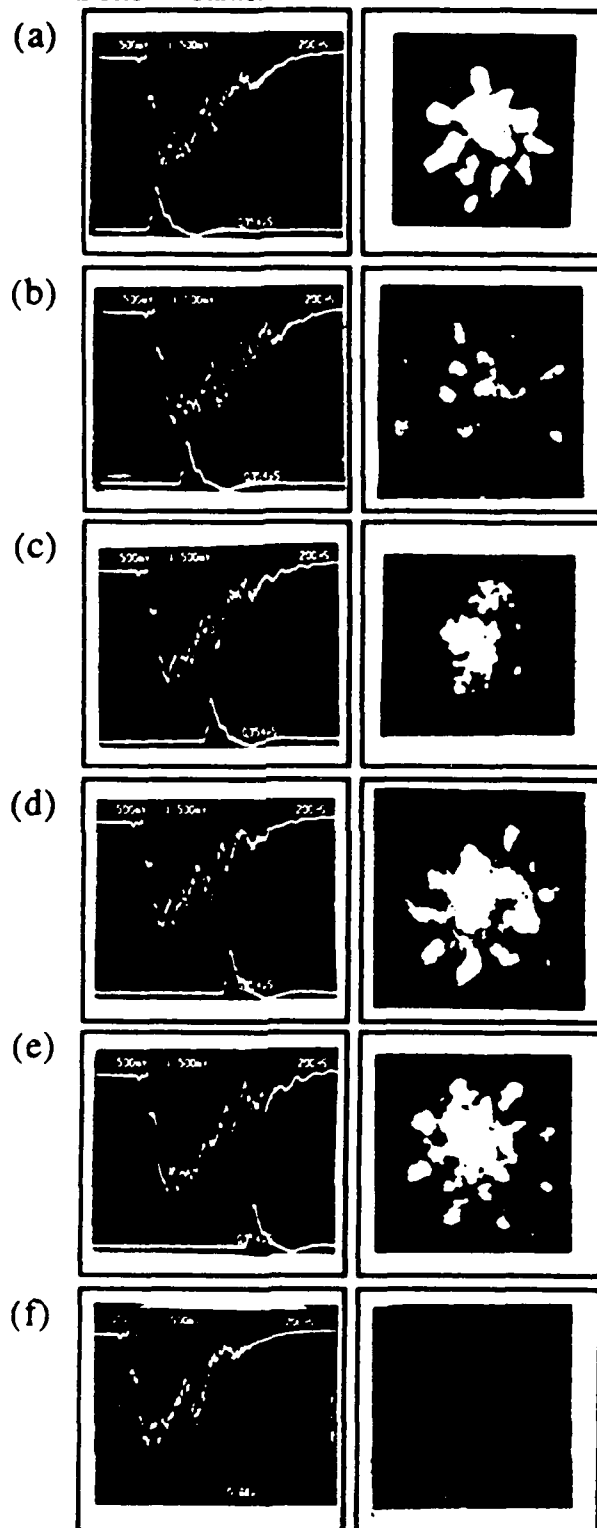


Figure 4.13. A time-resolved Cerenkov plate photograph series including: a) 50 ns, ND=2.0, b) 260 ns, ND = 2.2, c) 520 ns, ND = 1.5, d) 700 ns, ND = 1.0, e) 900 ns, ND = 1.0, f) 1100 ns, ND = 1.0.

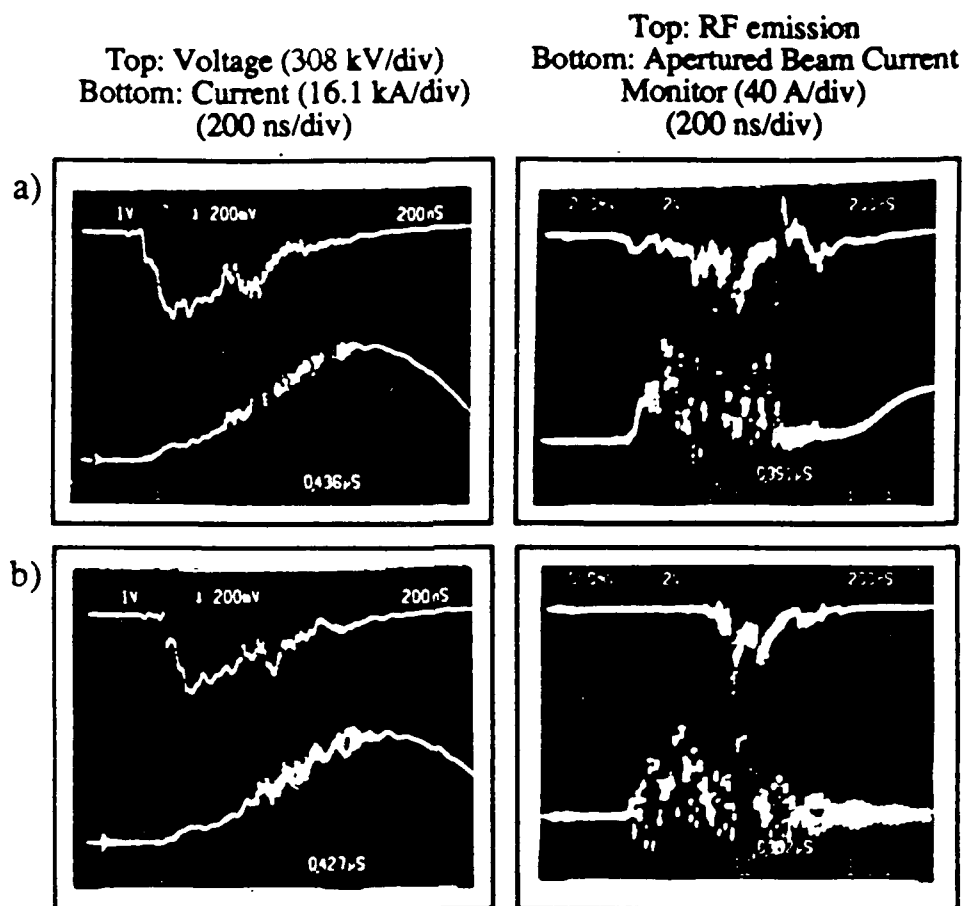


Figure 4.14. Apertured beam current monitor data a) without 200 kV foil filter (M1315), b) with 200 kV foil filter (M1331).

directions. Without going into all the details of the interpretation, it should be noted that the idealized picture in Figure 4.16 is consistent with the following physical explanation. The initial peak is due to a rapidly expanding cathode plasma. The negative deflection should be due to expanding anode plasma. The final positive excursion appears to be due to more dense late-time cathode plasma. These interpretations have been verified by moving the position of the probe laser beam away from the surface of the anode (from 0.1 cm to 0.4 cm) and noting the changes in the timing of the various peaks. Thus, from the laser deflection diagnostic it appears that the initial drop in the voltage (before voltage peaking) may be caused by on-axis A-K shorting from a fast component of cathode plasma. However, the voltage peaks back up, possibly due to plasma pinching or erosion, and an electron beam continues to be generated in a plasma filled diode system. This may explain the beam plasma instability which was observed beginning at voltage peaking. The experimental observations are summarized in Tables 4.1, 4.2, and 4.3.

Top: Voltage (716 kV/div)
 Bottom: He-Ne Deflection (0.27 mrad/div)
 $x_b = 0.4$ cm
 200 ns/div

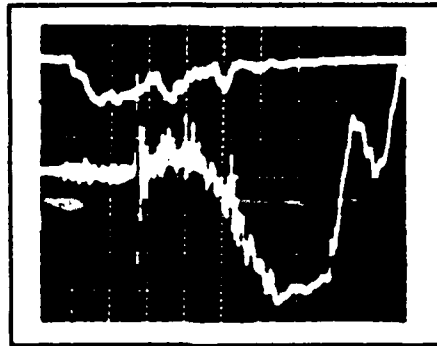


Figure 4.15. He-Ne deflection data with laser axis aligned on the cathode centerline axis.

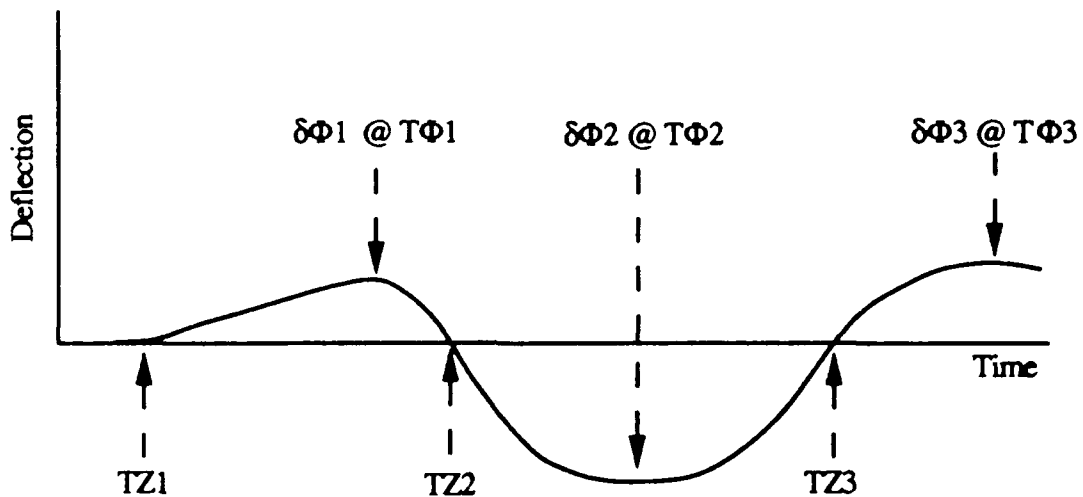


Figure 4.16. Idealized He-Ne deflection data, defining various times and deflection values to be used in the analysis. TZ1, TZ2, and TZ3 are the three zero crossings of the signal. $\delta\Phi_1$, $\delta\Phi_2$, and $\delta\Phi_3$ are the three peak values of the deflections, occurring at times $T\Phi_1$, $T\Phi_2$, and $T\Phi_3$.

Table 4.1. Summary of Electrical Characteristics, Observations.

Diagnostic	Period	Observations	Caveats
	Early: $t \leq 400$ ns Late: $t > 400$ ns		
	Early	Child-Langmuir behavior <i>implied</i> closure velocities: $(5.8 \pm 0.5 - 7.3 \pm 0.6)$ or $(7.5 \pm 0.5 - 10.0 \pm 0.8)$ cm/ μ s no RF emission/B-dot oscillations	initial non-CL regime during rise time
ELECTRICAL (section 4.1) <i>Voltage</i> <i>Currents</i> <i>RF Emission</i>	Late	<u>non-Child-Langmuir behavior: 'voltage peaking'</u> increase in diode impedance large increase in current flowing to the walls anode conditioning effects dependence on anode materials bounds on minimum anode dose: ($230 \pm 40 - 425 \pm 160$) J/gr <u>RF emission/large B-dot oscillations</u> reduced for cleaner anode materials reduced for larger anode-cathode gaps reduced for less severe voltage peaking reduced with external axial magnetic field	actual anode doses are higher RF bursts also detected at shorting

Table 4.2. Summary of Beam Diagnostics Experimental Observations.

Diagnostic	Period	Observations	Caveats
	Early: $t \leq 400$ ns Late: $t > 400$ ns		
BEAM (section 4.2) <i>Cerenkov</i> <i>Electrical</i>	Early	<i>Cerenkov</i> : stable, inward directed beamlets <i>Electrical</i> : behavior overall similar to C-L large inward directed angles $> 20^\circ$ non-reproducible from shot to shot evidence for cathode plasma instabilities or ion enhancements on axis large modulation γ of transported current	diagnostics used with 20 MHz filter due to large oscillations
	Late	<i>Cerenkov</i> : loss of stable beamlets, large emittance growth evidence for collective/inductive effects <i>Electrical</i> : current almost goes away after initial C-L period lower current than in early stage large, fast current spikes sometimes observed evidence for collective/inductive effects <i>effective</i> closure velocities: $10.1 \pm 1.3 - 11.3 \pm 1.6$ cm/ μ s	diagnostics used with 20 MHz filter due to large oscillations

Table 4.3. Summary of Plasma Diagnostics Observations.

Diagnostic	Period	Observations	Caveats
PLASMA (section 4.3) <i>Spectroscopy</i> <i>He-Ne Deflection</i>	Early: $t \leq 400$ ns Late: $t > 400$ ns		
	Early	<i>Spectroscopy:</i> Low average charge diode plasma: H, C_2, CH, CII <i>Deflection:</i> cathode plasma crossing at $\approx 0.4 \mu s$ <i>apparent</i> closure velocities: $7.8 \pm 0.6 - 11.4 \pm 0.4 \text{ cm}/\mu s$ lower bound on peak cathode plasma line densities: $(2-3) \times 10^{13} \text{ cm}^{-2}$ at shorting	unknown source for plasma in case of spectroscopy cathode or anode origin? Deflection observations actually depend on probe laser position rather than time. These given for 0.1 cm off of anode.
	Late	<i>Spectroscopy:</i> High average charge diode plasma: $CIV, CIII, CII$ $T_e \geq 7 \text{ ev}$ from CRE code <i>Deflection:</i> anode plasma observed from $0.6-1.2 \mu s$	

References for Section 4

1. A. K. Strignakov and I. V. Kurchatov, Tables of Spectral Lines of Neutral and Ionized Atoms, Plenum Press, NY, 1968
2. J. R. Pierce, The Identification of Molecular Spectra,
3. L. E. Thode, "Energy lost by a relativistic electron beam due to two-stream instability", Phys. Fluids, 19(2), 305, 1976.
4. G. Benford, "Radiation and ionization by relativistic electron beams", J. Plasma Physics, 10(2), 203, 1973.
5. S. Whetstone, Ph.D. thesis, University of Michigan.

5.0 Theoretical Progress on Electron Beam-Induced

Emission from Carbon Plasmas

We are concerned here with electron beam heated plasmas focusing on the CIV 5g-4f transition occurring at 2530 Angstroms. These studies were performed to provide theoretical support for experiments being conducted using the Michigan Electron Long-Pulse Beam Accelerator(MELBA).^{4,5} The theoretical model is discussed first to provide necessary background. Studies are then presented which identify two types of plasma response dependent upon the heating rate. Finally implications of the general studies upon MELBA experiments are discussed.

5.1 THEORETICAL MODEL

The CIV 2530 Angstrom line behavior cannot be addressed by considering only the plasma ionization dynamics (atomic physics). Heating and cooling rates are important and depend upon the plasma macroscopic evolution and electron beam-plasma interactions. The complete theoretical model consists of three coupled modules describing the plasma hydrodynamics, ionization dynamics, and electron beam-plasma interactions. Basic assumptions assume a one- dimensional geometry, no externally applied electromagnetic fields, and an optically thin plasma. The three modules are discussed below. Many theoretical models have been developed to describe plasma macroscopic motion. The slightly modified one-fluid, two-temperature hydrodynamics equations used have the form

$$\frac{Dv}{Dt} = v \frac{1}{x^{\delta-1}} \frac{d}{dx} x^{\delta-1} u \quad (1)$$

$$\frac{Du}{Dt} = -v \frac{\partial}{\partial x} (P + q) + \frac{v}{Vol} \frac{\partial \Delta MOM}{\partial t} \quad (2)$$

$$\frac{DE_i}{Dt} = -(P_i + q)\dot{v} + Q_i + R_{ei} + S_i \quad (3)$$

$$\frac{DE_e}{Dt} = -P_e\dot{v} + Q_e - R_{ei} + S_e - R - E_{ion} \quad (4)$$

where the convective derivative is defined as

$$\frac{Df}{Dt} = \frac{\partial f}{\partial t} + u \frac{1}{x^{\delta-1}} \frac{d}{dx} x^{\delta-1} f \quad (5)$$

and v is the specific volume, u is the bulk fluid velocity, P is the total specific plasma pressure, Vol is the plasma volume, ΔMOM is the momentum transferred in beam-plasma collisions, q is the Von Neumann⁶ artificial viscosity, R_{ei} the specific interspecies energy transfer, E_{ion} is the specific ionization energy, and R is the specific energy loss from line, recombination, and bremsstrahlung radiation. Also E_j is the specific thermal energy, P_j is the specific pressure, Q_j is the specific thermal conduction, and S_j is the specific external source or sink for species j which is either i for ions or e for electrons. The equations are described as slightly modified since the ionization energy is not absorbed into the electron internal energy term of Equation (4). This isolates effects of the ionization energy which represents a nonlinear coupling with the ionization dynamics model and requires use of special numerical techniques.⁷

The second module is the ionization dynamics which uses a Collisional-Radiative Equilibrium Model (CRE). The term equilibrium denotes neglect of the time derivative, thereby restricting the model's validity to timing regimes where the plasma hydrodynamic time scale is longer than the atomic relaxation time. The CRE model follows 104 quantum energy levels using 54 rate equations of the form

$$\frac{\partial n_j}{\partial t} = \sum_i W_{ji} n_i - \sum_i W_{ij} n_j \quad (6)$$

where n_j is the population of quantum state j and W_{ij} is the sum of the reaction rates representing transitions from state i to j . CRE models generally require one rate equation per energy level, but an averaging technique allows use of fewer equations than energy levels.⁸ Atomic processes included are collisional excitation and deexcitation, spontaneous emission, collisional ionization, three body recombination, radiative recombination and dielectronic recombination. Rate coefficients were obtained from the Naval Research Laboratory and the methods used to calculate them are catalogued by Duston et al.⁹ The energy level structure is that used by Thornhill et al.¹⁹

The third module describes both collisional and collective electron beam-plasma interactions. Collisional processes are standard coulomb collisions and bremsstrahlung emission. Collisional energy loss is described using a stopping power based upon a Fokker-Plank collision operator for a partially ionized plasma¹¹ and is given by

$$\frac{\partial}{\partial x} (n_b E_T) = -4\pi n_i r_o^2 E_o n_b \alpha_e \frac{E_T^2}{E_T^2 - E_o^2} \quad (7)$$

where

$$\alpha_e = Z \ln \left(\frac{\beta \gamma E_o \sqrt{\gamma - 1}}{I_z} \right) + Z_{eff} \ln \left(\frac{\lambda_D I_z}{2 \gamma E_o r_o} \right)$$

$$\gamma = \frac{1}{\sqrt{1 - (\frac{v}{c})^2}}, \quad \beta = \frac{v}{c}, \quad \lambda_D = \sqrt{\frac{T_p}{4\pi n e^2}}, \quad r_o = \frac{e^2}{m_e c^2}, \quad I_z = Z(11 \pm 3) \text{ eV}$$

and E_o is the electron rest mass energy, n_b is the beam number density, n_i is the plasma ion number density, E_T is the total beam electron energy, c is speed of light, I_z is the ionization energy

¹², T_p is the plasma temperature, v is the speed of the beam electrons, and α_e is the modified

coulomb logarithm which accounts for partial ionization effects. Comparison of collisional to bremsstrahlung energy loss reveals that in carbon bremsstrahlung is negligible for electron energies below 29 MeV.

Collective processes are difficult to model due to their inherent nonlinear nature. The primary concerns here are identification of possible processes, time required for saturation, and the amount of energy transferred. The first two questions are addressed using an instability classification developed by Lau¹³ which assumes a field free plasma and neglects beam electron self collisions. This classification utilizes the beam-plasma electron density ratio and relativistic measures of beam energy to divide the instability phase space into five domains. Each domain gives a critical wave number, frequency, and growth rate for the collective processes it encompasses.

The classification is used to identify which instabilities may occur. The critical wavelength yields a critical plasma size which is compared to the actual plasma size to determine occurrence. Growth rates indicate how quickly the instability saturates and affects the energy transfer. Simulations show that saturation occurs on time scales much shorter than the plasma hydrodynamic time scale, thus the plasma perceives saturation as instantaneous. The final question is how much energy is transferred through the collective interaction. This parameter is difficult to estimate, but studies show the maximum transfer is thirty percent of the beam energy.^{14,15} The model requires user specification of this percentage.

Equation of state definitions and transport laws complete the theoretical model and provide the coupling between modules. The plasma electron and ion number densities are coupled using an effective charge model. Thermal energies and pressures are calculated using the ideal gas law. The ionization dynamics model yields energy level populations necessary to calculate the ionization energy and the power lost through radiation. Fourier's law describes thermal conduction using Braginskii's¹⁶ thermal conductivities and interspecies energy transfer is modelled using the Spitzer collision frequency.¹⁷

5.2 GENERAL PARAMETER STUDIES

We first must decide exactly what parameter regime we desire to study, since the theoretical model allows variations in both plasma and beam parameters. We are primarily concerned with plasma response to the energy source nature. By nature we do not mean if the energy is transferred through collective or collisional processes since it turns out that collective processes always occur in the systems studied. Instead nature here refers to variations in beam parameters such as power density.

Figure 1 gives the problem geometry and the plasma initial conditions. The parameter studies use a square pulse, 1 MeV beam with power density and pulse length varied to maintain a consistent time integrated energy transfer. Instability strengths are set at low values to guard against unrealistic energy transfers.

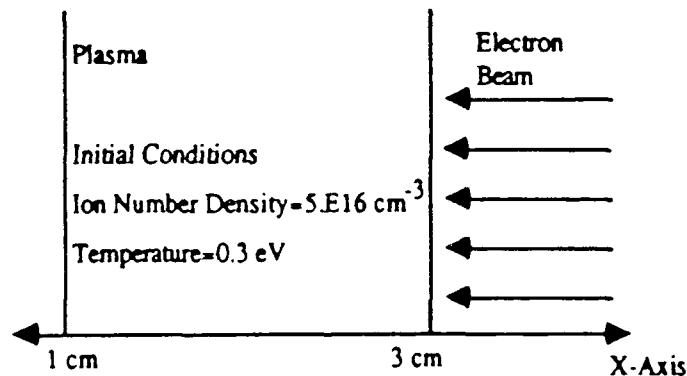


Figure 1. General simulation geometry and initial plasma conditions.

Explanation of a few concepts is useful before examining the results. Two figures per simulation are given, one giving the energy partitioning and the other the CIV 2530 Angstrom line evolution. The energy partitioning readily clarifies where the deposited energy goes. Recall that first phase of our objective is to heat the plasma to temperatures where CV is the dominant ion species. Therefore during heating we want to maximize the internal energy which is proportional to the plasma temperature. The second phase is plasma cooling which induces recombination reactions, hopefully populating the CIV 5g level faster than it can decay, thus producing a population inversion. During this phase we desire to quickly minimize internal energy.

The CIV 2530 Angstrom line evolution directly measures our success. The peak present during beam heating results from the plasma heating to temperatures where CIV is the dominant ion species. The peak after the beam pulse is from plasma cooling and the subsequent CV-free electron recombination reactions.

Studies examining energy transfer effects rate reveal two distinct plasma behaviors labeled Type A and Type B. Type A behavior occurs for "slow" heating rates and is illustrated by Figures 2 and 3. The Type A plasma converts most of the deposited energy into radiation thus experiencing little heating. This is not necessarily undesirable if the radiation is the type desired. Figure 3 shows an ionization peak late in the beam pulse and a recombination peak shortly after pulse ends. This is a desirable behavior but the intensity is fairly low, approximately an order of magnitude lower than Type B response. The low intensity results from nonuniform plasma heating with only the plasma edges heating to temperatures where CIV and CV is expected.

Type B response occurs for "fast" heating rates and is illustrated by Figures 4 and 5. Type B plasmas efficiently convert deposited energy into internal energy resulting in high plasma temperatures. The plasma then cools through radiation and expansion. The CIV 2530 Angstrom line exhibits a sharp ionization peak with recombination creating continuum rather than a peak. The intensity is approximately an order of magnitude greater than in a Type A response. The Type B plasma exhibits uniform heating with cooler edges due to expansion.

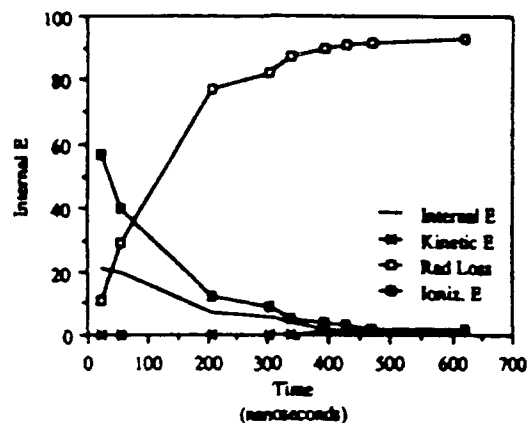


Figure 2. Type A energy partitioning in a 2 cm long plasma of ion number density $5 \times 10^{16} \text{ cm}^{-3}$ heated by 1.0 MeV, 10^6 Watt/cm^2 electron beam transferring of 3% of the beam energy for 300 nanoseconds.

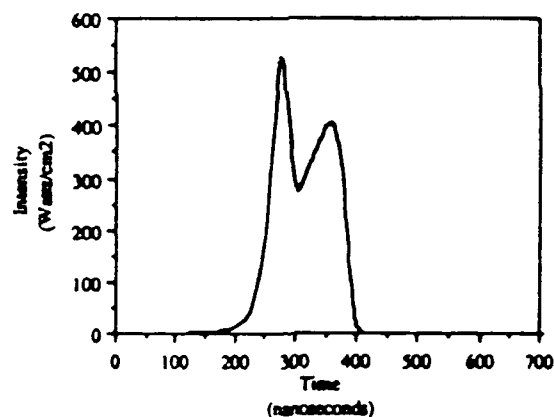


Figure 3. Type A CIV 2530 Å line emission in a 2 cm long plasma of ion number density $5 \times 10^{16} \text{ cm}^{-3}$ heated by 1.0 MeV, 10^6 Watt/cm^2 , electron beam transferring of 3% of the beam energy to the plasma for 300 nanoseconds.

The two different responses are explained by examining the radiative power variation with plasma density and temperature calculated with CRE model and given in Figure 6. There are two important trends to note. The first involves the temperature behavior of the radiated power, which peaks at approximately 8 eV. This peak represents a barrier which the plasma must "burn through" to efficiently convert deposited energy into forms other than radiative emission. The second is that the barrier height depends upon the ion number density. Thus for a given energy source, it is easier to burn through the barrier at lower number densities. Keep in mind during the following discussion that the time integrated total energy supplied to the plasma is the same in each case, only the rate varies. Also note that the plasma can only radiate away a certain amount of energy, any energy supplied in excess of this limit is converted into other forms such as internal energy.

The Type A response occurs in conjunction with "slow" heating rates which supply small amounts of energy over a long times. The energy supplied at any one time is only slightly greater than the radiative emission barrier height, therefore the plasma slowly burns through the barrier. Expansion produces lower ion densities at the plasma edges resulting in a lower barrier height and faster burn through. Thus the plasma edges reach higher temperatures than the center.

The Type B response occurs during "fast" heating rates where large amounts of energy are supplied very quickly. The amount of energy exceeding the radiative emission barrier height is very large allowing rapid increase of the internal energy and quick barrier burn through. The heating is uniform since little expansion occurs during the short beam pulse and the entire plasma burns through the barrier at approximately the same rate.

The heating rate may induce different plasma responses, with hotter plasmas arising from faster heating rates. The differentiation between "fast" or "slow" heating rates is determined by how quickly the energy source allows plasma burn through of the radiative emission barrier. Cooling rate effects were not investigated but faster cooling should result in sharper recombination peaks and shortening of the continuum produced by Type B plasmas.

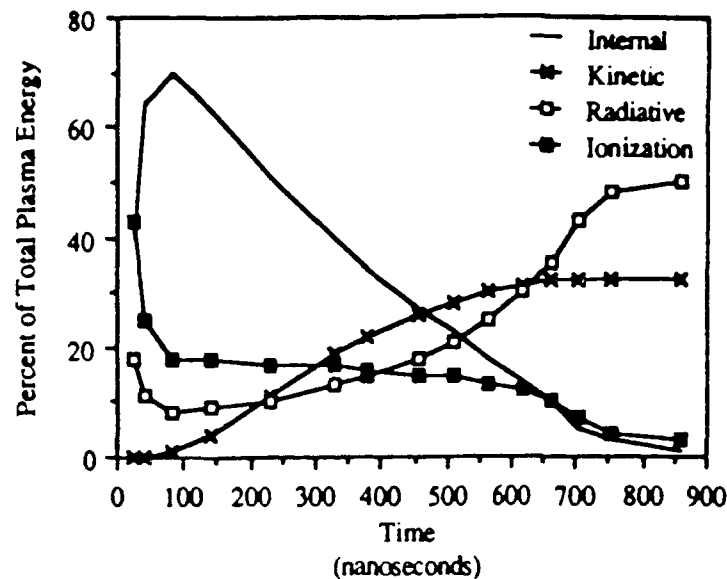


Figure 4. Type B energy partitioning in a 2 cm long plasma of ion number density $5 \times 10^{16} \text{ cm}^{-3}$ heated by 1.0 MeV, $5 \times 10^6 \text{ Watt/cm}^2$ electron beam transferring of 3% of the beam energy for 60 nanoseconds.

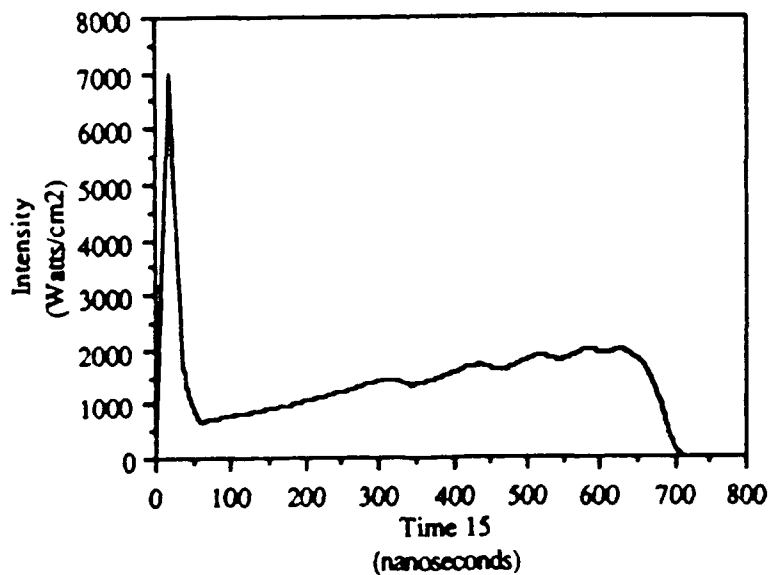


Figure 5. Type B CIV 2530 Å line emission in a 2 cm long plasma of ion number density $5 \times 10^{16} \text{ cm}^{-3}$ heated by 1.0 MeV, $5 \times 10^6 \text{ Watt/cm}^2$, electron beam transferring of 3% of the beam energy to the plasma for 60 nanoseconds.

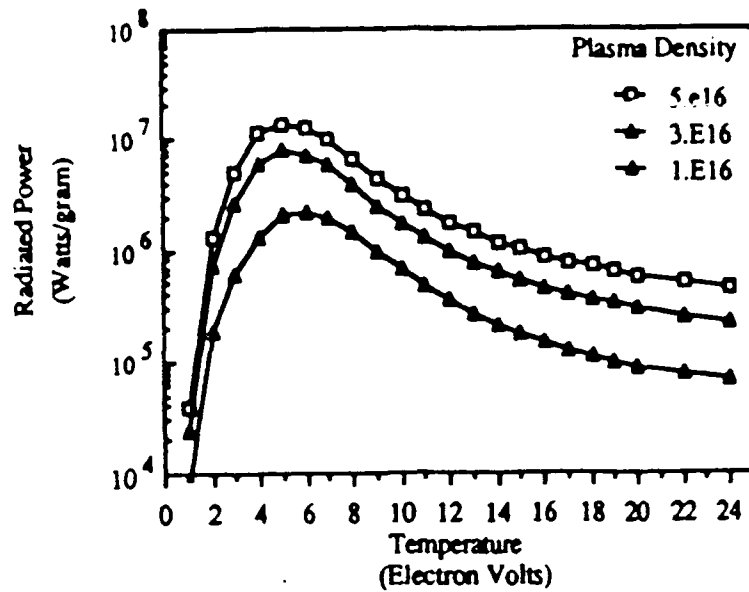


Figure 6. Carbon radiative emission as a function of electron temperature and ion number density calculated using the CRE Model.

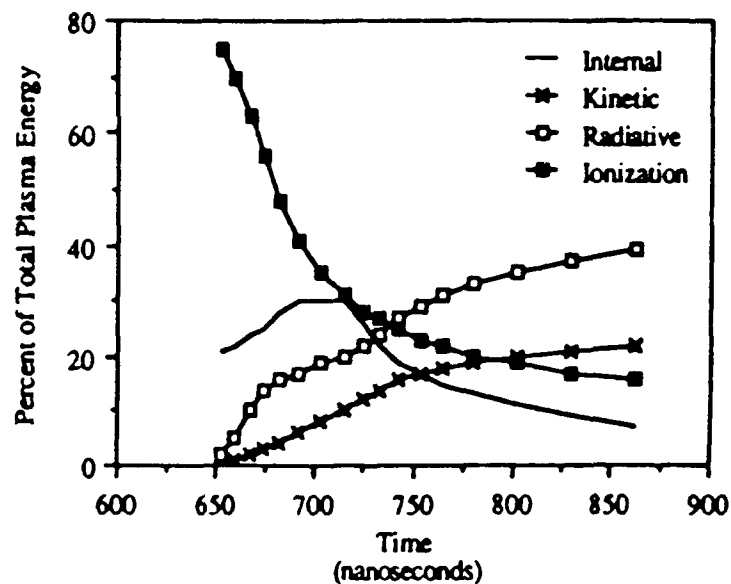


Figure 7. Typical energy partitioning for a MELBA electron beam-plasma system. This system had an initial ion density of $5 \times 10^{17} \text{ cm}^{-3}$ and an instability strength of 1 %. Beam pulse ends at 717 nanoseconds.

5.3 MELBA IMPLICATIONS

It was mentioned earlier that these studies were originally initiated to provide theoretical support for MELBA experiments. These experiments recently studied CIV 2530 Angstrom time behavior. Experimental observations indicate that the line coincides electron beam presence, disappearing shortly after the beam turns off.¹⁸ It should be noted that the lines evolution is not continuously observed, but is deduced from time integrated spectra taken at various times during experimental runs. The integration window varies from 50 to 100 nanoseconds yielding a general picture of the exact behavior. Bulk plasma temperature estimates are under 10 eV.^{4,5}

The expected temperature regime coupled with the quick 2530 Angstrom line disappearance at pulse ending indicate that MELBA could be inducing a Type A plasma response. The model was used to simulate typical MELBA runs and results are given for a plasma density of $5 \times 10^{17} \text{ cm}^{-3}$ and a one percent instability. Simulation of MELBA is a complex undertaking and details are given elsewhere.¹⁹

Simulations confirm that MELBA may indeed induce a predominantly Type A response. The evolution is interesting in that initial behavior is Type B with the internal energy growing faster than the radiative losses as shown in Figure 7. This initial behavior is dominated by the outer edges burning through the radiative emission barrier while the bulk of the plasma remains so cold that it has not begun to emit significant radiation. The Type A response becomes evident as the bulk plasma begins to heat and the radiative energy grows while the internal energy decreases.

The CIV 2530 Angstrom emission is given in Figure 8. The first peak is an ionization peak produced by the plasma edge heating past the CIV dominance threshold temperature. The second is not actually a peak, but instead is an increase in CIV emission from the bulk plasma interrupting the beam pulse ending. The emission essentially disappears after the pulse ends. The low level continuum after 717 nanoseconds results from recombination in the plasma edges. It corresponds to the Type B behavior the plasma edge was previously noted as exhibiting.

5.4 REFERENCES FOR THEORY SECTION

4. M. Cuneo, R. M. Gilgenbach, M. L. Brake, R. F. Lucey, L. Horton, S. Bidwell, J. Miller, K. Pierce, T. Repetti, and L. Smutek, Bull. Am. Phys. Soc. **30**, 1502 (1985).
5. M. Cuneo, R. M. Gilgenbach, and M. L. Brake, IEEE Trans. on Plasma Science **PS-15**, 375 (1987).
6. J. Von Neumann and R. D. Richtmeyer, Appl. Phys. **21**, 232 (1950).
7. D. Duston, Ph.D Dissertation, University of Michigan, 1977.
8. D. Duston and J. Davis, Phys. Rev. A **23**, 2602 (1981).
9. D. Duston, R. Clark, J. Davis, and J. Apruzese, Phys. Rev. A **27**, 1441 (1983).
10. J. Ward Thornhill, James J. Duderstadt, and Dwight P. Duston, J. Appl. Phys. **62**, 1181 (1987).
11. D. Mosher, Phys. of Fluids **18**, 846 (1975).
12. R. D. Evans, The Atomic Nucleus, (McGraw-Hill, New York 1955).
13. Y. Y. Lau, NRL Memorandum Report 5601, 1985.

14. M. Lampe and P. Sprangle, Phys. of Fluids 18, 475 (1974).
15. L. E. Thode and R. N. Sudan, Phys. of Fluids 18, 1552 (1975). and L. E. Thode and R. N. Sudan, Phys. of Fluids 18, 1564 (1975).
16. S. I. Braginskii, in Reviews of Plasma Physics, M. A. Leontovich, Ed., (Consultants Bureau, New York 1965), Vol. 1.
17. L. Spitzer, Physics of Fully Ionized Gases, (Interscience, New York 1962).
18. R. M. Gilgenbach, T. Kammash, and M. L. Brake, AFOSR 86-0012 Annual Progress Report, 1987.
19. S. C. Whetstone, Ph.D. Dissertation, University of Michigan, 1988.

6.0 Graduate Students and Doctoral Dissertations

Supported by This Contract

1) M. E. Cuneo, Ph. D. Dissertation Completed in 1988:

"Characterization of the Time Evolution of a Microsecond Electron Beam Diode with Anode Effects"

2) S. Whetstone, Ph.D. Dissertation completed in 1988:

"Radiation Hydrodynamics of an Electron Beam Heated Carbon Plasma"

3) T. Repetti, Dissertation in Progress

4) S. Swanekamp, Dissertation in progress

5) Y. Chung, Dissertation in progress.

7.0 Publications Resulting from this Grant

Refereed Journal Publications

- 1) "Spectroscopic Studies of Anode Plasmas in a Microsecond Electron Beam Diode", M.E. Cuneo, R. M. Gilgenbach, and M. L. Brake,
IEEE Transactions on Plasma Science, PS-15 375 (1987)
- 2) "Temporally Resolved Spectroscopy of Laser-Induced Carbon Ablation Plasmas", IEEE Transactions on Plasma Science PS-15 73 (1987)
- 3) "Effects of Helium upon Electron Beam Excitation of N_2^+ at 391.4 nm and 427.8 nm", M. L. Brake, R. M. Gilgenbach, R. F. Lucey, K. Pearce, and T. Repetti, Applied Physics Letters 49 696 (1986)
- 4) "Fast-Sensitive Laser Deflection Diagnostic Suitable for Transient Plasma Analysis", C. L. Enloe, R. M. Gilgenbach, and J. S. Meachum, Rev. Sci. Instr. 58 1597 (1987)
- 5) " Microscopic and Macroscopic Materials Properties Effects on Ultraviolet Laser induced Flashover of Angled Plastic insulators in Vacuum", C.L. Ensloe and R. M. Gilgenbach, IEEE Trans. on Plasma Science, 16 379 (1988)
- 6) "Ultraviolet-Induced Flashover of a Plastic insulator in Vacuum", C. L. Enloe and R. M. Gilgenbach, Plasma Chem. and Plasma Proc. 7 89 (1987)

Conference Papers

- 1) "UV Spectroscopy and non-Child-Langmuir Effects in Long Pulse Electron Beam Diodes",
M. E. Cuneo, R. M. Gilgenbach, J. E. Tucker, T. E. Repetti,
Bull. Am. Phys. Soc. **32** 1887 (1987)
- 2) "Hydrodynamic and Spectral Study of REB Produced Carbon Plasmas", S. Whetstone and T.
Kammash, Bull. Am. Phys. Soc. **32** 1887 (1987)
- 3) "Electron Beam Induced Emission from Carbon Plasmas", S. Whetstone and T. Kammash,
SPIE, Jan. 1989
- 4) "Spectroscopic Studies of Electron Beam Driven Anode Plasmas", Bull. Am. Phys. Soc. M.
Cuneo, R. M. Gilgenbach, M. L. Brake, T. Repetti, and J. E. Tucker, **31** 1478 (1986)

REFERENCES

- Abr77a E. A. Abramyan, B. A. Altercop, and G. D. Kuleshov, "Microsecond Intensive Electron Beams," in *Proc. of the 2nd Int. Topical Conf. on High Power Electron and Ion Beam Research and Technology*, vol. 2, (Cornell, NY), Oct. 3-5, 1977, pp. 755-760.
- Act57 E. W. V. Acton, "The Space-Charge Limited Flow of Charged Particles in Planar, Cylindrical and Spherical Diodes at Relativistic Velocities," _____, _____, 203(1957).
- Auc83 O. Auciello, A.A. Haasz, and P. G. Stangeby, "Methane Production from Carbon under Combined Electron and Atomic Hydrogen Bombardment: Evidence for a Synergistic Effect?," *Phys. Rev. Lett.*, 50(10), 783(1983).
- Bac75 F. M. Bacon, and H. A. Watts, "Vacuum arc anode plasma. II. Collisional-radiative model and comparison with experiment," *J. Appl. Phys.*, 46(11), 4758(1975).
- Bak73 R. B. Baksht, A. P. Kudinov, and E. A. Litvinov, "Cathode Plasma in the Initial Stage of a Vacuum Discharge," *Sov. Phys. Tech. Phys.*, 18(1), 94(1973).
- Bak78 R. B. Baksht, S. P. Bugaev, V. I. Koshelev, G. A. Mesyats, V. P. Stas'ev, K. N. Sukhushin, and M. N. Timofeev, "Cathode Plasma in a magnetically insulated diode," *Sov. Tech. Phys. Lett.*, 3(7), 243(1978).
- Baz77 G. P. Bazhenov, O. B. Ladyzhenskii, E. A. Litvinov, and S. M. Chesnokov, "Emission surface of the cathode plasma in explosive electron emission," *Sov. Phys. Tech. Phys.*, vol. 22, no. 10, pp. 1212-1215, Oct. 1977.
- Baz79 G. P. Bazhenov, O. B. Ladyzhenskii, S. M. Chesnokov, and V. G. Shpak, "Probe diagnostics of oscillations in the plasma potential in an explosive-emission diode," *Sov. Phys. Tech. Phys.*, vol. 24, no. 1, pp. 67-71, Jan. 1979.
- Bek87 G. Bekefi, F. Hartemann, and D. A. Kilpatrick, "Temporal evolution of beam emittance from a field-emission electron gun," *J. Appl. Phys.*, vol. 62, no. 5, pp. 1564-1567, Sep., 1987.
- Ben73 G. Benford, "Radiation and ionization by relativistic electron beams," *J. Plasma Physics*, 10(2), 203(1973).
- Ber77 K. D. Bergeron, "One-and two-species equilibria for magnetic insulation in coaxial geometry," *Phys. of Fluids*, 20(4), 688(1977).

- Bev69 P. R. Bevington, *Data Reduction and Error Analysis for the Physical Sciences*, McGraw Hill, 1969.
- Bla75 A. E. Blaugrund, and G. Cooperstein, "Intense Focusing of Relativistic Electrons by Collapsing Hollow Beams," *Phys. Rev. Lett.*, vol. 34, no. 8, pp. 461-464, Feb., 1975.
- Bla77 A. E. Blaugrund, G. Cooperstein, and S. A. Goldstein, "Relativistic electron beam pinch formation process in low impedance diodes," *Phys. Fluids*, vol. 20, no. 7, pp. 1185-1194, July, 1977.
- Boi84 V. A. Boiko, F. V. Bunkin, V. I. Derozhiev, and S. I. Yakovlenko, "Possibilities of Amplification of Ultraviolet and Soft X-ray Radiation on Multiply Charged Ion Transitions in a Recombining Plasma," *IEEE Jor. of Quantum Electron.*, QE-20, 206(1984).
- Bra86 M. L. Brake, T. E. Repetti, K. Pearce, and R. F. Lucey, "Emission Spectroscopy of Long Pulse Relativistic Electron Beam Produced Argon Plasmas," *J. Appl. Phys.*, July(1986).
- Bug75 S. P. Bugaev, V. I. Koshelev, and M. N. Timofeev, "Electron energy spectrum in a high-current vacuum diode," *Sov. Phys. Tech. Phys.*, vol. 19, no. 9, pp. 1193-1195, Mar. 1975.
- Bun83 F. V. Bunkin, V. M. Bystritskii, V. I. Derzhier, A. N. Didenko, et. al., "Observations of Stimulated Emission as a Result of Transitions in HeII Pumped by a Proton Beam," *Sov. Jor. of Quantum Electron.*, 13, 679(1983).
- Bur86 V. S. Burmasov, S. G. Voropaev, A. L. Dobrivskii, S. V. Lebedev, and M. A. Shcheglov, "Measurement of the plasma density in a microsecond-range vacuum diode by optical interferometry," *Sov. J. Plasma Phys.*, 12(4), 251(1986).
- But77a SAND78-0080, Apr.-Sep. 1977 Electron Beam Fusion Progress Report, pp. 179-185.
- But77b SAND77-0002, Oct. 77-Mar. 78 Particle Beam Fusion Progress Report, pp. 128-129.
- But78 SAND79-1011, Apr.-Dec. 1978 Particle Beam Fusion Progress Report, pp. 141-142.
- Cap84 G. J. Caporaso, and R. E. Melendez, "Relativistic Spherical Diode Solutions," ATA Beam Physics Note 232, 4/13/84.
- Chi11 C. D. Child, *Phys. Rev.* 32,492(1911).
- Cho87 E. H. Choi, H. M. Shin, D. I. Choi, and H. S. Uhm, "Influence of ion effects on high-current relativistic diodes," *J. Appl. Phys.* 61, 2160(1987).

- Coo75 G. Cooperstein, and J. J. Condon, "Impedance characteristics of diodes operating in the self-pinch mode," *J. Appl. Phys.*, vol. 46, no. 4, pp. 1535-1538, April, 1975.
- Cre77 J. M. Creedon, "Magnetic cutoff in high-current diodes," *J. Appl. Phys.*, 48, 1070(1977).
- Cre75 J. M. Creedon, "Relativistic Billouin flow in the high v/γ diode," *J. Appl. Phys.*, 46, 2946(1975).
- Cun86 M. E. Cuneo, R. M. Gilgenbach, M. L. Brake, "Spectroscopic Study of Anode Plasmas in a Microsecond Electron Beam Diode," *IEEE Trans. on Plasma Science*, PS-15(4),375(1986).
- Dak76 D. Dakin, J. Benford, Physics International Memo, "B_z Diodes," , 10/9/76.
- DCa76 M. Di Capua, J. Creedon, and R. Huff, "Experimental investigation of high-current relativistic electron flow in diodes," *J. Appl. Phys.*, vol. 47, no. 5, pp. 1887-1896, May, 1976.
- Enl87 C. L. Enloe, R. M. Gilgenbach, and J. S. Meachum, "Fast, sensitive laser deflection system suitable for transient plasma analysis," *Rev. Sci. Instrum.*, 58(9), 1597(1987).
- Enl88 C. L. Enloe, *Ultraviolet-Induced Flashover of Highly-Angled Polymeric Insulators in Vacuum*, Ph.D. Thesis, Dept. of Nuclear Engin., University of Michigan, May 1988.
- Far72 M. Farber, J. E. Robin, and R. D. Srivastava, "High-power electron beam deposition studies on aluminum and graphite," *J. Appl. Phys.*, vol. 43, no. 8, pp. 3313-3317, August, 1972.
- Fly56 P. T. G. Flynn, "The Discharge Mechanism in the High-Vacuum Cold-Cathode Pulsed X-ray Tube," *Proc. Phys. Soc. B*, 69, 748(1956).
- FreXX
- Fri68 F. Friedlander, R. Hechtel, H. Jory, and C. Mosher, Defense Nuclear Agency, Defense Nuclear Agency Final Report No. DASA 2173, 1968 (unpublished).
- Frd72 M. Friedman, and M. Ury, "Microsecond Duration Intense Relativistic Electron Beams," *Rev. Sci. Instrum.*, vol. 43, no. 11, pp. 1659-1661, Nov., 1972.
- Gil85 R. M. Gilgenbach, L. D. Horton, R. F. Lucey, Jr., S. Bidulko, M. Cuneo, J. Miller, and L. Smutek, "Microsecond Electro-Beam Diode Closure Experiments," Invited Paper in *Proc. 5th IEEE Pulsed Power Conf.*, (Arlington, Va.), June 10-12, 1985, pp. 126-132.

- Gol74 S. A. Goldstein, R. C. Davidson, J. G. Siambis, and R. Lee, "Focused-Flow Model of Relativistic Diodes," *Phys. Rev. Lett.*, vol. 33, no. 25, Dec., 1974.
- Gol75 S. A. Goldstein, and R. Lee, "Ion-Induced Pinch and the Enhancement of Ion Current by Pinched Electron Flow in Relativistic Diodes," *Phys. Rev. Lett.*, vol. 35, no. 26, Oct., 1975.
- Goy86 J. Goyer, J. Levine, and S. Wong, "Diodes with Electrode-Generated Plasmas As Opening Switches," *Bull. Amer. Phys. Soc.*, vol. 31, no. 9, p. 1395, paper 1V2, Oct. 1986.
- Gra85 E. W. Gray, and L. F. Rinehart, "Impedance Effects on Anode Formation of Microparticles in an Electron-Beam Diode," in *Proc. 5th IEEE Pulsed Power Conf.*, (Arlington, Va.), June 10-12, 1985, pp. 122-125.
- Gra86 E. W. Gray, "Microparticles and their effects in vacuum diodes," *J. Appl. Phys.*, vol. 59, no. 11, pp. 3708-3715, June, 1986.
- Gro46 F. W. Grover, *Inductance Calculations, Working Formulas and Tables*, Dover, N. Y., 1946.
- Gud63 L. I. Gudzenko, and L. A. Sheplin, *Sov. Phys. JETP*, 18, 988(1963).
- Gud77 L. I. Gudzenko, and L. A. Sheplin, in *Proceedings of the P. N. Lebedev Institute*, vol. 83, G. N. Basov, Ed., 1977.
- Ham72 D. A. Hammer, W. F. Oliphant, I. M. Vitkovitsky, and V. Fargo, "Interaction of Accelerating High-Current Electron Beams with External Magnetic Fields," *J. Appl. Phys.*, 43(1), 58(1972).
- Hau85 S. Hauver, R. E. Pechacek, J. R. Greig, D. P. Murphy, and M. Raleigh "A Gated Microchannel Plate Image Intensifier Packaged in a Reflex Camera Back," NRL Memorandum Report 5702, 1985.
- Her89 M. E. Herniter, "_____", Doctoral Thesis, University of Michigan, Dept. of Electrical Engineering, May 1989.
- Hin83 D. D. Hinshelwood, "Cathode Plasma Formation in Pulsed High Current Vacuum Diodes," *IEEE Trans. Plasma. Sci.*, vol. PS-11, no. 3, pp. 188-196, Sept., 1983.
- Hin84 D. D. Hinshelwood, "Explosive Emission Cathode Plasmas in Intense Relativistic Electron Beam Diodes," Ph. D. Thesis, MIT, 1984 (unpublished).
- How65a W. L. Howes, "Effect of Initial Velocity on One-Dimensional, Bipolar, Space-Charge Currents," *J. Appl. Phys.* 35(6), 2039(1965).
- How65b W. L. Howes, "One-Dimensional Space-Charge Theory. I. Generalization," *J. Appl. Phys.* 37, 437(1965).

- How65c W. L. Howes, "One-Dimensional Space-Charge Theory. II. Relativistic Child Law," *J. Appl. Phys.* 37, 438(1965).
- Ive52 H. F. Ivey, "Space Charge and Transit Time Considerations in Planar Diodes for Relativistic Velocities," *J. Appl. Phys.*, 23, 208(1952).
- Ive53 H. F. Ivey, "Approximate Solutions of the Space-Charge Problem for some Unusual Electrode Geometries," *J. Appl. Phys.*, 24(11), 1466(1953).
- Jel58 J. V. Jelley, *Cerenkov Radiation and its applications*, Pergamon Press, 1958.
- Joh77 D. J. Johnson, D. J. Nagel, and W. F. Oliphant, "VUV emission from high-intensity focused REB discharges into aluminum targets," *J. Appl. Phys.*, vol. 48, no. 3, pp. 1058-1060, March, 1977.
- Joh78a D.J. Johnson, "Impedance characteristics of heated REB diodes," *Appl. Phys. Lett.*, Vol. 32, no. 10, May, 1978.
- Joh78b D.J. Johnson, S. A. Goldstein, R. Lee, and W. F. Oliphant, "Time-dependent impedance behavior of low-impedance REB diodes during self-pinching," *J. Appl. Phys.*, vol. 49, no. 9, pp. 4634-4643, Sep., 1978.
- Jor69 H. R. Jory and A. W. Trivelpiece, "Exact Relativistic Solution for the One-Dimensional Diode," *J. Appl. Phys.* 40, 3294(1969).
- Kel75a J. G. Kelly, and L. P. Mix, "Measurements of high-current relativistic electron diode plasma properties with holographic interferometry," *J. Appl. Phys.*, 46(3), 1084(1975).
- Kel75b J. G. Kelly, S. A. Goldstein, and D. W. Swain, "Influence of anode composition on the electrical properties of relativistic electron-beam diodes," *J. Appl. Phys.*, 46(11), 4726(1975).
- Kir67 P. T. Kirstein, G. S. King, W. E. Waters, *Space Charge Flow*, McGraw Hill, 1967.
- Kli86 R. E. Klinkowstein, and R. E. Shefer, "Experimental Investigation of Cathode Plasma Formation in the SRL Long Pulse E-Beam Test Stand," *Bull. Amer. Phys. Soc.*, vol. 31, no. 9, p. 1396, paper 1V7, Oct., 1986.
- Kor71 E. D. Korop, and A. A. Plyutto, "Plasma Effects in the Emission of a Needle Cathode," *Sov. Phys. Tech. Phys.*, 16, 830(1971).
- Lan13 I. Langmuir, *Phys. Rev.* 2, 450(1913).
- Lan23 I. Langmuir, and K. B. Blodgett, "Currents Limited by Space Charge Between Concentric Cylinders," *Phys. Rev.*, 22, 347(1923).
- Lan24 I. Langmuir, and K. B. Blodgett, "Currents Limited by Space Charge Between Concentric Spheres," *Phys. Rev.*, 23, 49(1924).

- Lan29 I. Langmuir, "The Interaction of Electron and Positive Ion Space Charges in Cathode Sheaths," *Phys. Rev.*, vol. 33, no. 6, pp. 954-989, June, 1929.
- Lau85 Y. Y. Lau, "A Hybrid Mode and a Classification of Beam Plasma Instabilities," NRL Memorandum Report 5601, 1985.
- Lin71 J. J. Clark, and S. Linke, "Operating Modes of a Pulsed 50-GW Diodes," *IEEE Trans. Electron Devices ED-18*, 322(1971).
- Luc88 R. F. Lucey, "Long-Pulse Relativistic Electron Beam Generation and Propagation in Gases and in UV Laser Ionized Channels," Doctoral Thesis, Univ. of Mich., Dept. of Nuc. Eng., 1988.
- Mar87a Y. Maron, M. D. Coleman, D. A. Hammer, and H. S. Peng, "Experimental determination of the electric field and charge distribution in magnetically insulated ion diodes," *Phys. Rev. A*, 36(6), 2818(1987).
- Mar87b Y. Maron, M. D. Coleman, D. A. Hammer, and H. S. Peng, "Measurements of ion transverse-velocity distribution in the gap of an ion-beam diode," *J. Appl. Phys.*, 61(10), 4781(1987).
- Mar88 Y. Maron, L. Perelmutter, E. Sarid, M. E. Foord, and M. Sarfaty, "Spectroscopic Determinations of Particle Fluxes and Charge-State Distributions in a Pulsed-Diode Plasma," to be published, *Phys. Rev. A*.
- Mix73 L.P. Mix, J. G. Kelly, G. W. Kuswa, D. W. Swain, and J. N. Olsen, "Holographic Measurements of the Plasmas in a High-Current Field Emission Diode," *J. Vac. Sci. Technol.*, 10(6), 951(1973).
- Mül51 K. Müller-Lübek, "Über die ambipolare Raumladungsströmung bei ebenen Elektroden," *Z. Angew. Phys.* 3, 409(1951).
- Mrt76 T. H. Martin, and R. S. Clark, "Pulsed microsecond high-energy electron beam accelerator," *Rev. Sci. Instrum.*, vol. 47, no. 4, pp. 460-463, April, 1976.
- Nag81 L. Nagel, E. Cohen, A. Vladimirescu, K. Zhang, A. R. Newton, D. O. Pederson, A. Sangiovani-Vincentelli, "SPICE version 2G.5 User's Guide (10 Aug. 81)", Univ. of Calif., Berkeley.
- Nei87 J. R. Neighbours, F. R. Buskirk, and X. K. Maruyama, "Cerenkov and sub-Cerenkov radiation from a charged particle beam," *J. Appl. Phys.*, 61(5), 2741(1987).
- Par73 R. K. Parker, "Explosive Electron Emission and the Characteristics of High Current Electron Flow," Ph. D. Thesis, Univ. of NM, 1973, University Microfilms no. 74-11,800.
- Par74 R. K. Parker, R. E. Anderson, and C. V. Duncan, "Plasma-induced field emission and the characteristics of high current flow," *J. Appl. Phys.*, vol. 45, no. 6, pp. 2463 - 2479, June, 1974.

- Pat83 E. L. Patterson, R. A. Hamil, and G. E. Samlin, "Electron-beam uniformity of a large-area high current accelerator diode," *J. Appl. Phys.*, vol. 54, no. 2, pp. 515-518, Feb., 1983.
- Pel70 D. Pellinen, "A High Current, Subnanosecond Response Faraday Cup," *Rev. Sci. Instrum.*, 41, 1347(1970).
- Per86 J. D. Perkins, J. H. Jacob, R. E. Klinkowstein, R. E. Schefer, L. Friedland, G. Allen, and J. A. Sullivan, "Observation of Constant Impedance Operation of a High Voltage Electron Beam Diode with a Cold Cathode," *Bull. Amer. Phys. Soc.*, vol. 31, no. 9, p. 1396, paper 1V10, Oct., 1986.
- PieXX J. R. Pierce, *The Identification of Molecular Spectra*,
- Pou75a J. W. Poukey, "Ion effects in relativistic diodes," *Appl. Phys. Lett.*, 26(4), 145(1975)
- Pou75b J. W. Poukey, "Two-dimensional ion effects in relativistic diodes," *J. Vac. Sci. Technol.*, 12, 1214(1975).
- Pro75 D.I. Proskurovskii, V. P. Rotshtein, A. F. Shubin, and E. B. Yankelevich, "Processes in a vacuum diode during a current burst," *Sov. Phys. Tech. Phys.*, vol. 20, no. 10, pp. 1342-1346.
- Prn81 D. S. Prono, H. Ishizuka, E. P. Lee, B. W. Stallard, and W. C. Turner, "Charge-exchange neutral-atom filling of ion diodes: Its effect on diode performance and A-K shorting," *J. Appl. Phys.*, 52(4), 3004(1981).
- Pul83 Pulse Sciences Report, "Electron Beam Accelerator," PSI-P-83-105, 7/84.
- Ram80 J. J. Ramirez, and D. L. Cook, "A study of low-current-density microsecond electron beam diodes," *J. Appl. Phys.*, vol. 51, no. 9, pp. 4602-4611, Sept., 1980.
- Rob68 T. G. Roberts, and W. H. Bennett, "The Pinch Effect in Pulsed Streams at Relativistic Energies," *Plasma Physics*, vol. 10, pp. 381-389, 1968.
- Ros86 L. A. Rosocha, and K. B. Riepe, "Electron-Beam Sources for Pumping Large Aperture KrF Lasers," *Fusion Tech.*, 11, 576(1986).
- Sam87 G. E. Samlin, "Evaluation of Cerenkov convertors for measuring current density distribution in large-area electron beams," *J. Appl. Phys.*, vol. 62, no. 6, pp. 2169-2172, Sep., 1987.
- San78 SAND78-0080, Apr.-Sep. 1977 Electron Beam Fusion Progress Report, pp. 188-191.

- Sch75 R. Schneider, C. Stallings, and D. Cummings, "Generation and extraction of microsecond intense relativistic electron beams," *J. Vac. Sci. Technol.*, vol. 12, no. 6, pp. 1191-1193, Nov./Dec., 1975.
- Sc184 L. G. Schlitt, S. Humphries, Jr., J. M. Potter, Pulse Sciences Report, "The Scantron Microwave Source," PSI-FR-174, 7/84.
- She88 R. E. Shefer, L. Friedland, and R. E. Klinkowstein, "Evolution of high current, cold cathode diodes to steady state," *Phys. Fluids*, vol. 31, no. 4, pp. 930-939, April, 1988.
- Sim88 J. E. Simpkins, and P. K. Mioduszewski, "Automated outgassing facility with inductive heating," *Rev. Sci. Instrum.*, 59(2), 276(1988).
- Sla79 W. B. Herrmannsfeldt, "Electron Trajectory Program," SLAC-226, November, 1979.
- Smi79 Ian Smith, "Pulse Power for 0.3 - 0.5 μ s Durations," UCID-18318, July 1979.
- Smu86 L. Smutek, Masters Thesis, University of Michigan, Dept. of Nuclear Engineering, May 1986.
- Snf87 T. W. L. Sanford, J. A. Halbleib, J. W. Poukey, R. C. Pate, C. E. Heath, J. A. Alexander, T. Roemer, R. Mock, P. W. Spence, G. A. Proulx, V. Bailey, "Measurement of Electron Energy Deposition Necessary to Form an Anode Plasma in Ta, Ti, and C for Coaxial Bremsstrahlung Diodes," *Bull. Amer. Phys. Soc.*, 32, 1786(1987).
- Spn75 P. Spence, K. Triebes, R. Genuario, and D. Pellinen, "REB Focusing in High Aspect Ratio Diodes," in *Proc. of the Int. Topical Conf. on Electron Beam Research and Technology*, vol. 1, (Albuquerque, NM), Nov. 3-6, 1975, pp. 346-363.
- Str68 A. R. Strigakov and I. V. Kurchatov, *Tables of Spectral Lines of Neutral and Ionized Atoms*, New York: Plenum, 1968.
- Swa75 D. W. Swain, S. A. Goldstein, J. G. Kelly, and G. R. Hadley, "Observations of anode ions associated with pinching in a relativistic electron beam diode," *J. Appl. Phys.*, 46(10), 4604, (1975).
- Swa77a D. W. Swain, L. P. Mix, L. W. Kruse, and J. W. Poukey, "Measurements of large ion currents in a pinched relativistic electron beam diode," *J. Appl. Phys.*, 48(1), 118, (1977).
- Swa77b D. W. Swain, S. A. Goldstein, L. P. Mix, J. G. Kelly, and G. R. Hadley, "The characteristics of a medium current relativistic electron-beam diode," *J. Appl. Phys.*, 48(3), 1085(1977).
- Tho76 L. E. Thode, "Energy lost by a relativistic electron beam due to two-stream instability," *Phys. of Fluids*, 19(2), 305(1976).

- Thr85 W. Thornhill, The Hydrodynamics and Ionization Dynamics of Particle Beam Heated Carbon Ablation Plasmas, Ph.D. Dissertation, University of Michigan, Department of Nuclear Engineering, 1985.
- Vas81 M. A. Vasilevskii, I. M. Roife, and V. I. Engel'ko, "Operating characteristics of explosive-emission multipoint cathodes with microsecond pulse lengths," *Sov. Phys. Tech. Phys.*, 26(6), 671(1981).
- Wea83 R.C. Weast, Ed., *Handbook of Chemistry and Physics*, Boca Raton, FL: CRC Press, 1983.
- Wei74 P. S. P. Wei, W. M. Leavens, and J. L. Adamski, "Near-ultraviolet emission spectrum from an intense relativistic electron-beam discharge," *J. Appl. Phys.*, 45(5), 2163(1974).
- Wei86 R. Wei, and P. J. Wilbur, "Space-charge-limited current flow in a spherical double sheath," *J. Appl. Phys.*, 60(7), 2280(1986).
- Whe88 S. C. Whetstone, "Radiation Hydrodynamics of an Electron Beam Heated Carbon Plasma," Ph. D. Thesis, The University of Michigan, Department of Nuclear Engineering, 1988.

**Spectroscopic Study of Anode Plasmas in a
Microsecond Electron Beam Diode**

M. E. Cuneo, R. M. Gilgenbach, and M. L. Brake

Reprinted from
IEEE TRANSACTIONS ON PLASMA SCIENCE
Vol. PS-15, No. 4, AUGUST 1987

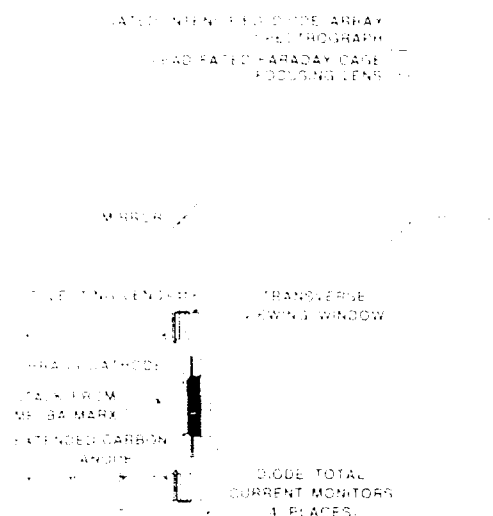


Fig. 1. Schematic view of the experimental configuration of the microtron, spectrometer, and measurement system.

flow became clouded with a film of carbon after multiple pulses, this did not significantly affect the light output.

Typically 5–15 shots were fired in a series. The vacuum windows were completely replaced after each individual series. The diode chamber was cleaned after approximately 20–25 shots (about two series). This involved cleaning carbon off of the plastic insulators and interior surfaces with freon and revoiling the insulators. In order to refurbish the diode after a series, the carbon anode was faced off with a lathe to remove pitting from arc damage. No special cleaning techniques were used for the carbon anode. In order to remove a heavy carbon coating, the cathodes were polished with sandpaper and fine steel wool, cleaned, and degreased.

The light from the anode plasma was imaged onto the entrance slit of a 0.275-m spectrograph (Hamamatsu Monospec 27) coupled to an optical multichannel analyzer (OMA) (Tricon-Northern TN 6500 series) via mirrors and a final focusing lens. This configuration was able to resolve individual peaks when they were about 1 nm or greater apart. The optical axis for these experiments was aligned 0.1 cm off of the anode face, directly at the diode axis. The magnification of the optical system was about 0.7. Even though the dimensions of the actual plasma may be greater than 150 cm² (from open shutter picture), the volume of light collected by the various optical elements was less than 0.5 cm³. This volume was in the center of the diode radially, about 0.1 cm away from the anode axially.

The spectroscopic equipment was located in a lead-lined Faraday cage. The OMA consisted of a 1674-channel intensified diode array. OMA gates could be set with arbitrary delay relative to some starting time, with widths as small as 50 ns. In order to obtain high signal-to-noise ratios, however, gate widths of 500 ns are generally required. The optical system was calibrated through the use of a standard source with a known filament temperature

account for the wavelength-dependent response of the acrylic window, optics, grating, and OMA detector diodes. The detector diodes were calibrated for wavelength using a krypton gas discharge lamp.

III. EXPERIMENTAL RESULTS AND DISCUSSION

We observed different types of optical emission behavior from the anode region depending on the relative timing of the OMA gate and the voltage pulse. When the OMA was gated early in the pulse, no light was detected. Gating later in the pulse, when the anode dose had increased sufficiently, but before diode shorting, low-intensity atomic emission was detected. Intense optical emission was detected by gating after voltage collapse had occurred. For the purposes of modeling and discussion, this is roughly equivalent to the evolution of the diode through three different stages, which we define here by the deposited dose and diode closure. These stages represent the following: stage I—Child-Langmuir mode early in time before the dose was high enough for anode plasma formation and emission; stage II—a low-impedance transition mode with an anode plasma later in time after the dose was high enough; and stage III—an intense vacuum-arc mode after diode shorting. Depending on the crowbar setting, closure velocity, and dose, shots may not necessarily have stage II. We discuss the data in terms of the timing of the OMA gate relative to the diode evolution through these stages. In this section, examples of these different types of spectra with diode voltage and current data will be presented for a series of crowbarred and noncrowbarred shots.

Typical data from these experiments are summarized in Table I. The spectroscopic observations classify the data in one of the three possible stages as referred to above. The accelerator can be operated in the crowbarred mode or in the noncrowbarred mode. The crowbarred mode limited the dose by short-circuiting the generator before diode shorting. The figures presented below, and referred to in Table I, consist of four parts: (a) diode voltage; (b) diode current compared to Child-Langmuir current model; (c) conventional empirical closure velocity plot; and (d) optical emission spectra. The OMA gate is shown on parts (a) through (c); $t = 0$ for the OMA gate is referenced from the initial rise of the voltage. The closure plot is a linear best fit of $(1 - P)^{-1/2}$, where P is the experimental perveance $(I/V^{3/2})$. The extrapolation of the linear portion of $(1 - P)^{-1/2}$ gives a prediction of the diode shorting time. Note that we refer to $(1 - P)^{-1/2}$ as the "effective gap." The effective gap is expected to be linear when the diode current and voltage are following Child-Langmuir scaling. The spectra are labeled with the peak identification [26] and all spectra are presented on the same relative intensity scale. We list the total dose by the end of the OMA gate or at deviation of the experimental current from Child-Langmuir scaling in Table I.

Shots with no light detected during the OMA gate are classified as stage I. These shots were not correlated with the OMA gate. Shots with light detected during the OMA gate are

Spectroscopic Study of Anode Plasmas in a Microsecond Electron Beam Diode

M. E. CUNEO, STUDENT MEMBER, IEEE, R. M. GILGENBACH, MEMBER, IEEE, AND
M. L. BRAKE, MEMBER, IEEE

Abstract—Experiments have been performed to investigate the visible emissions (370–600 nm) from long-pulse electron-beam-driven carbon anode plasmas, and to correlate the spectroscopic evidence for ions with deviations of the diode current and voltage from Child-Langmuir behavior. Electron beams had peak voltages of ~ 0.8 MV, current densities approaching 10^3 A/cm², and pulselengths of about 1 μ s. Diode closure resulted in three phases of the beam/plasma evolution. In stage I the deposited electron dose was smaller than that required for anode plasma optical emission (≤ 250 J/gr). No deviations of the diode operation from conventional Child-Langmuir scaling were observed. In stage II, the electron dose was large enough for anode plasma formation before shorting (≥ 350 J/gr), and low-intensity optical emission was primarily from CII and CIII. During stage II, two types of non-Child-Langmuir diode behavior occurred due to the presence of an anode plasma. An anomalous voltage peaking behavior occurred at an average dose of 740 J/gr, at about 80 percent of the diode shorting time. The diode impedance was constant during this voltage peaking behavior, contrary to the impedance collapse expected from Child-Langmuir behavior in a closing diode. This voltage peaking was accompanied by an increase in continuum emission, particularly at shorter wavelengths. A bipolar impedance level was occasionally observed before voltage peaking, at an average dose of 410 J/gr, at about 66 percent of the predicted shorting time. During stage III, an intense vacuum arc mode, the cathode plasma shorted the anode-cathode (A-K) gap, resulting in intense optical emission from CI through CIV on noncrowbarred pulses, and from CII, C₂, CH, and H on crowbarred pulses.

I. INTRODUCTION

NUMEROUS researchers have investigated the physics of cathode and anode plasmas in intense electron beam diodes. An understanding of both cathode and anode plasmas is crucial in achieving the efficient conversion of stored energy into well-characterized electron beams. Short-pulsed beams ($\tau \leq$ few 100 ns) have typically been used in applications such as flash X-ray generation or ICF, where high peak powers and electron current densities are desired. Long-pulse beams (τ from a few hundred nanoseconds to a few microseconds) are generally used for applications where total delivered energy, pulselength, and voltage flatness are critical factors.

Manuscript received January 13, 1987; revised May 22, 1987. This work was supported by the Air Force Office of Scientific Research and by the National Science Foundation. M. E. Cuneo was supported by the Department of Energy under Grant DE-FC05-82ER75041 during part of his study at the University of Michigan. Any opinions, findings, conclusions, or recommendations expressed herein are those of the authors, and do not necessarily reflect the views of the DOE.

The authors are with the Intense Energy Beam Interaction Laboratory, Department of Nuclear Engineering, University of Michigan, Ann Arbor, MI 48109-2104.

IEEE Log Number 87-276700.

Long-pulse applications include gas or plasma laser excitation, high-power microwave generation, and free-electron lasers. In both pulselength regimes, cathode plasma closure in explosive-emission cold-cathode diodes typically limits electron beam pulselengths and total delivered beam energy. At large doses, however, anode plasma formation can also limit the pulselength, modify the impedance and stability of the diode, and affect the generator-to-diode power coupling.

This paper addresses the role of anode plasma in microsecond diode physics by correlating spectroscopic evidence for ions with changes in the diode electrical behavior. We have performed time-resolved visible (370–600 nm) spectroscopic emission measurements at the surface of a carbon anode in a long-pulse ($\sim \mu$ s) diode. These experiments were motivated by a previous experimental study [1] which showed two types of non-Child-Langmuir behavior in a microsecond diode with large anode-cathode (A-K) gaps (8–10 cm). In the first, the current showed enhancements consistent with bipolar [2] effects, while in the second, the rate of current rise was extremely rapid and the late-time voltage (≥ 600 ns) increased anomalously. The second type occurred much more frequently than the first. Ion effects in the diode were inferred from current modeling. In those experiments energies of up to 1.5×10^4 J were delivered to the anode before shorting at modest current densities (less than 20 A/cm² initially), yielding doses less than 100 J/gr. Possible sources of ions were intense vacuum arc anode phenomena [3], [4] as well as impact ionization of the residual background gas [5], both particularly important for the long pulselengths obtained (2.5–4 μ s). Thus, in this previous work, the presence of ions was strongly suspected but not experimentally verified.

The present experiments were performed with higher current densities (initially ~ 100 A/cm²) at intermediate A-K gaps (3–4 cm) and delivered energies typically between 4×10^3 and 7×10^3 J to the anode before shorting. Closure of the A-K gap resulted in late-time current densities approaching 10^3 A/cm², with total doses on the order of 10^3 J/gr by the end of the electron pulse.

Several investigators have performed comprehensive experimental studies of electron diode plasmas and closure in the short-pulse regime. Cathode plasmas have been studied using empirical modeling of closure [6]–[8], interferometry [7], [8], and time-resolved spectroscopy [7].

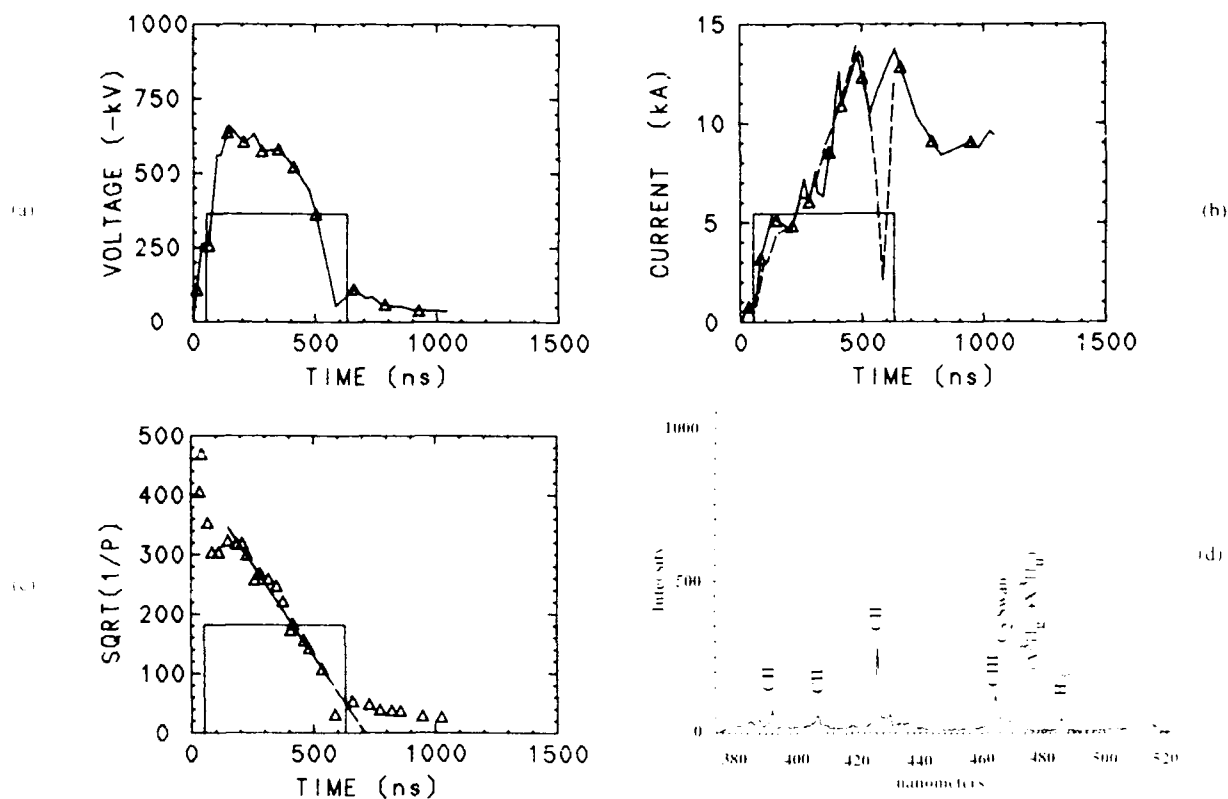


Fig. 3. (a) Voltage data and OMA gate from 50 to 630 ns on a crowbarred shot. (b) Current data (solid line), Child-Langmuir model (dashed line), with OMA gate. (c) Effective gap plot (units of $(1/P)^{1/2}$ are $\text{volt}^{-1/2} \text{amps}^{1/2}$), with OMA gate where P = experimental perveance, fitted portion (solid line), extrapolated portion (dashed line). (d) Emission spectrum.

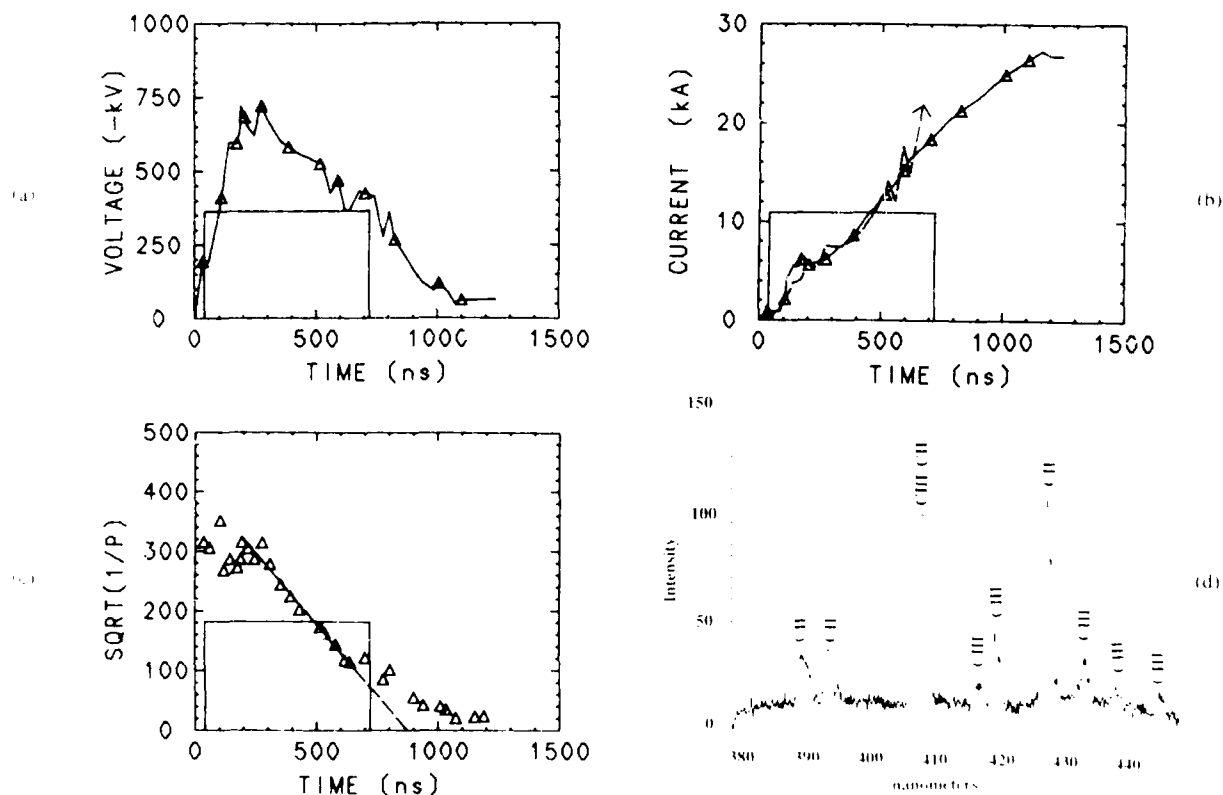


Fig. 4. (a) Voltage data and OMA gate from 40 to 720 ns on a noncrowbarred shot. (b) Current data (solid line), Child-Langmuir model (dashed line), with OMA gate. (c) Effective gap plot (units of $(1/P)^{1/2}$ are $\text{volt}^{-1/2} \text{amps}^{1/2}$), with OMA gate where P = experimental perveance, fitted portion (solid line), extrapolated portion (dashed line). (d) Emission spectrum.

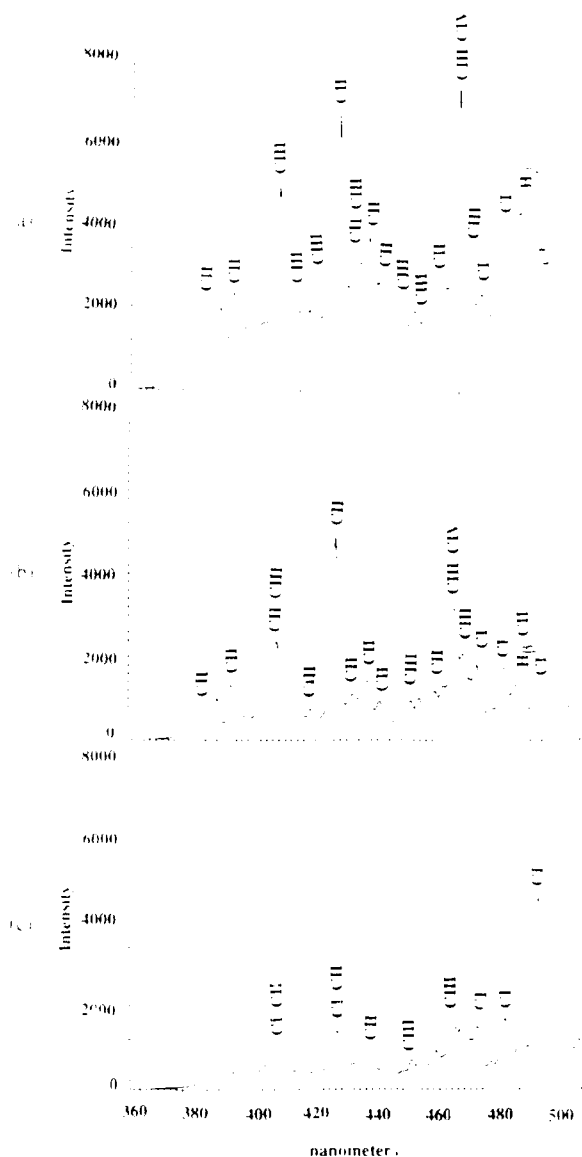


Fig. 7. Spectra from three noncrowbarred shots in which the OMA was gated after shorting. (a) OMA gate: 1.0–2.0 μ s, predicted shorting time = 1000 ns. (b) OMA gate: 2.1–3.1 μ s, predicted shorting time = 720 ns. (c) OMA gate: 3.0–4.1 μ s, predicted shorting time = 1000 ns.

The error estimate was based on the uncertainties in transition probability and peak intensity. The electron temperature appears to be constant with time for the first ~ 1.8 μ s after shorting, within experimental error; at a later time the temperature has decreased.

The electronic temperature may equal the electron temperature if the free electrons are in equilibrium with the bound (radiating) electrons. To exactly determine the equilibrium nature of our plasma would require a detailed model of all the possible kinetic mechanisms. It is important to note, however, that in our experiments, the electronic temperature of CII and the electronic temperature of CIII were equal within experimental error for the first 1.8 μ s following shorting. Also, the volume of plasma which was examined spectroscopically was small compared to the overall plasma dimensions.

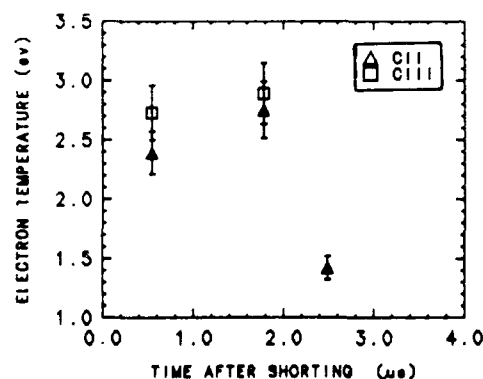


Fig. 8. Electron temperatures versus time after predicted diode shorting for spectra in Fig. 7.

IV. SUMMARY AND CONCLUSIONS

No anode plasma light was detected in any electron beam pulse when the OMA was gated well before predicted shorting and during the portions of the pulse where the dose was smaller than 250 J/gr. For this case, no deviations from Child–Langmuir scaling were observed (stage I). We observed low-intensity emission from carbon ions (CII and CIII) when the OMA gate occurred during portions of the electron beam pulse when the dose was greater than 350 J/gr, but before predicted shorting (stage II). The doses required for the formation of anode plasma in these experiments were consistent with those found in previous work, corresponding to an outgassing anode. The spectroscopic emission observed in these experiments was consistent with hydrocarbon surface impurities introduced by the diffusion pump, ionized outgassed anode components, and cool-cathode plasma constituents (which are primarily hydrocarbons [8]).

Due to the presence of ions, two types of non-Child–Langmuir behavior were observed. On a large fraction of the noncrowbarred shots the voltage displayed a peaking behavior late in time. This occurred at about 740 J/gr at about 80 percent of the predicted shorting time. The diode impedance during the peaking behavior was constant, and was not consistent with Child–Langmuir or bipolar levels. In some noncrowbarred shots an impedance consistent with bipolar current enhancement was observed before voltage peaking. This occurred at doses of about 410 J/gr at about 66 percent of the predicted shorting time. There were two different types of spectra observed, corresponding to different voltage behavior. The spectra obtained when gating the OMA during the voltage peaking behavior had continuum emission peaking at shorter wavelengths. The spectra obtained when the OMA gate occurred during normal voltage behavior or slight voltage peaking displayed a lower intensity uniform continuum. Further study is required to determine the cause of this voltage peaking mode, and to explain these other features.

When the OMA was gated during or after predicted diode shorting (stage III), we always measured intense light emission (15–60 times that of stage II), with the maximum detected emissions occurring just after short-

ing. In crowbarred pulses we detected optical emissions from CH, C⁺, CH⁺, and H. In noncrowbarred pulses, we detected atomic charge states of carbon up to CIV (at 580 and 581 nm) during the first microsecond following shorting. (Higher ionization states can be detected only at shorter wavelengths than we have explored.) The high currents and low voltages in stage III resulted in substantial coupling, giving very intense light emission from a 2–3 eV plasma. This is probably due to both heating of stage II plasma constituents from the anode and cathode plasma and the creation of new plasma through other vaporization processes and anode spot mechanisms. Noncrowbarred pulses (arc current ~20–30 kA) gave a more highly ionized plasma than the crowbarred pulses (arc current ~10 kA), and higher emission intensity.

Although the current densities in these microsecond pulselength diodes are smaller than in many short-pulse experiments, ion effects still play a role. Ion effects observed in previous experiments obtained at lower doses [1]–[3] are also important and seem to indicate that anode spot mechanisms and background gas ionization may also be involved. Vacuum arc mechanisms are of particular concern as they point toward a continually degrading diode performance due to anode erosion as described in [2]. Long pulse diodes operate on an intermediate time scale between short pulse diodes and vacuum arcs. Thus it is expected that both types of phenomenon become important. These effects must be addressed before stable reproducible diode performance can be obtained in the microsecond pulselength regime.

ACKNOWLEDGMENTS

The authors acknowledge experimental assistance from R. A. Lukew, Jr., E. E. Repetti, and J. E. Tucker.

REFERENCES

- [illegible]

Temporally Resolved Spectroscopy of Laser-Induced Carbon Ablation Plasmas

M. L. Brake
J. Meachum
R. M. Gilgenbach
W. Thornhill

AD-A205 716

POPULATION INVERSIONS IN ABLATION PLASMAS GENERATED BY
INTENSE ELECTRON B. (U) MICHIGAN UNIV ANN ARBOR DEPT OF
NUCLEAR ENGINEERING R M GILGENBACH ET AL NOV 88

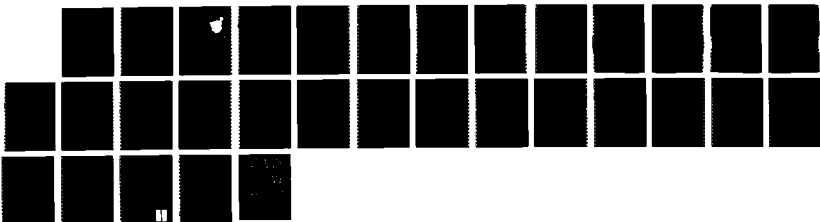
2/2

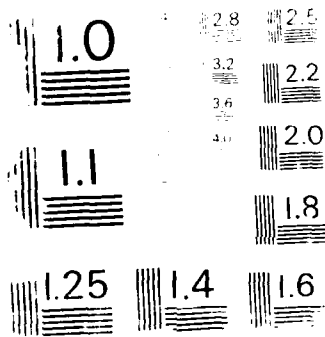
UNCLASSIFIED

AFOSR-TR-89-0294 AFOSR-86-0012

F/G 20/9

NL





Temporally Resolved Spectroscopy of Laser-Induced Carbon Ablation Plasmas

M. L. BRAKE, ASSOCIATE MEMBER, IEEE, J. MEACHUM, R. M. GILGENBACH, MEMBER, IEEE,
AND W. THORNHILL

Abstract—Temporally resolved emission spectra (360–630 nm) of carbon ablation plasmas produced during laser hole boring by a 25-ns duration 1-J ruby laser pulse are presented. The emitted line radiation originates from C^{III} to C^{II} depending upon the time relative to the laser pulse. Plasma temperatures of 12–14 eV during the laser pulse to about 4 eV, 140 ns after the laser pulse are obtained by comparing the spectroscopic results to a collisional-radiative equilibrium (CRE) model which bridges the gap between the local thermodynamic equilibrium (LTE) model and the coronal model.

I. INTRODUCTION

SURFACE ablation plasmas have an important role in the coupling of laser energy to materials in applications such as machining, welding, and hole boring [1]. Such plasmas have also been employed as the lasing medium in soft X-ray laser experiments [2]. In all of these applications the temporal evolution of the ablation plasma is particularly crucial. Spectroscopy provides an ideal noninvasive plasma diagnostic in the harsh environment of intense laser-plasma interactions.

In this paper we employ a spectrograph coupled to a gated optical multichannel analyzer (OMA) in order to obtain temporally resolved optical spectra of laser-induced ablation plasmas. This is in contrast to most previous spectroscopy measurements [3], [4] which have been time integration of tens of shots, as recorded on film. Since the gates to the OMA can be moved by 10 ns relative to the laser output, we can follow the temporal evolution of the rapidly varying ablation plasma.

Usually (see [3] and [4]) laser-produced plasmas are described by the corona model or by the local thermodynamic equilibrium (LTE) model. In the LTE model [6], it is assumed that the distribution of population densities of the electrons is determined by particle collision processes where each process is balanced by its inverse collisional process. The distribution of population densities of electron energy levels is the same as if the levels were in thermodynamic equilibrium. The LTE model can easily give temperature information from spectroscopic re-

sults if the plasma is dense enough for LTE to be valid (greater than approximately 10^{18} cm⁻³ depending upon plasma conditions). The corona model [6] on the other hand includes a balance between collisional ionization and radiative recombination. This model is used to describe low density plasmas (less than about 10^{11} cm⁻³) where atom-atom collisions are negligible. Unfortunately, many laser-produced plasmas fall between the regions of validity for the corona model and LTE. In this paper the spectroscopic results are compared to a comprehensive collisional-radiative equilibrium (CRE) model which describes plasmas not covered by the corona model or LTE.

II. EXPERIMENTAL CONFIGURATION

The experimental system is depicted schematically in Fig. 1. A Q-switched ruby laser was incident on a graphite target located in an evacuated (10^{-4} -torr) chamber. This eliminated complications due to air breakdown in the vicinity of the laser focal spot. A calorimeter measured the laser energy while a p-i-n diode monitored the pulse shape. These measurements yielded a ruby laser incident energy (on target) of about 1 J in a 25-ns full-width-at-half-maximum (FWHM) pulse. The laser was focused by a 25-cm focal length lens to the spot size of 300 μ m.

The target was a 0.9- by 0.9- by 0.238-cm-thick block of POCO graphite (type DFP-2), positioned such that the laser was incident perpendicular to the surface. The graphite target was mounted at the end of a lucite rod in the vacuum chamber. The spectroscopic system viewed the laser ablation plasma at 90° from the incident laser. Ablation plasma light was imaged onto the entrance slit of a 0.275-m spectrograph which was coupled to a 1024-element OMA. Two gratings were used in the spectrograph; the first had 1200 g/mm, blazed at 400- and 70-nm dispersion over the detector array length, and the second had 600 g/mm, blazed at 450- and 140-nm dispersion. Due to the limited light intensity and the limits of the pulse generator which produced the gate used by the OMA, the minimum gatewidth was about 50 ns. However, by delaying the gate in 10-ns intervals, time-resolved spectra were obtained. A small light bulb (3-mm diameter) was used to align the spectroscopy optics. Thus the spectra were obtained from light emitted about 1.5 mm from the target surface (which was as close as we could place the filament in our small alignment light bulb).

Manuscript received July 1, 1986; revised October 2, 1986. This work was supported by the Office of Naval Research, Grant N00014-85-1-0001, and the National Science Foundation, Grant PHY-85-10909.

M. L. Brake, J. Meachum, and R. M. Gilgenbach are with the Naval Air Engineering Department, Naval Air Station, Ann Arbor, MI 48109. W. Thornhill is with the Naval Research Laboratory, Washington, DC 20340.

IEEE Log Number 86-1067.

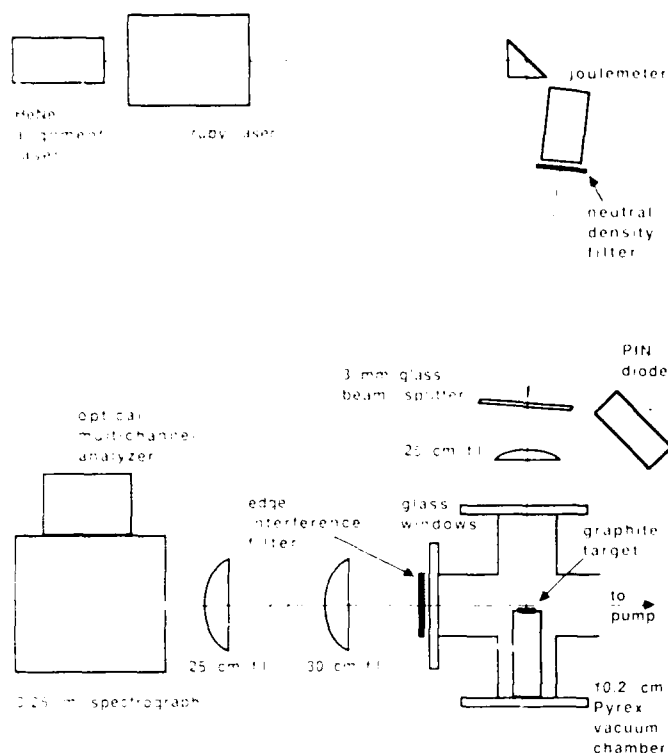


Fig. 1. Experimental configuration.

III. RESULTS

Neither the laser optics nor the target's position were altered during the course of the experiment, which involved firing the laser 50 times, resulting in a deep crater in the block of graphite. A microscope photograph ($100\times$) of the graphite surface is shown in Fig. 2. The small shallow hole beside the main hole has been observed in other laser target experiments [5] and is believed to result from imperfect alignment and focusing of the nonideal laser beam and from splattered material. Using a fixed target for many shots does change the effective distance by a microscopic amount, but using the same spot on the target eliminates the effect of gas desorption which would occur if the focal position on the target were changed between shots.

The total damage was produced by 50 ruby laser pulses of average FWHM of 25 ns and an average of 1 J/shot delivered to the target. For a simple lens of focal length 25.4 cm and diameter 3.8 cm, we estimate a beam waist of $300\text{ }\mu\text{m}$ in the focal plane with a 4-mm depth of focus. The average focused irradiance per shot was thus $5 \times 10^{10}\text{ W/cm}^2$.

The graticule on a microscope eyepiece was used to measure both the mean diameter of the hole at the surface and the lengths of 175- μm -diameter wire used to probe the depth of the hole. Due to the inability to measure the true dimensions of the hole, it is assumed that the hole volume is bounded by a right circular cylinder having a diameter equal to the mean diameter of the hole at the surface. The volume of the small shallow secondary hole was considered negligible compared to the volume of the main hole.



Fig. 2. Enlargement of the laser-damaged POCO graphite target.

TABLE I
HOLE DIMENSIONS AND TARGET DAMAGE ANALYSIS

hole depth = $2225 \pm 20\text{ }\mu\text{m}$
mean diameter at surface = $542 \pm 24\text{ }\mu\text{m}$
avg. volume lost per shot = $0.0076 \pm 0.0006\text{ mm}^3$
avg. mass lost per shot = $14.0 \pm 1.3\text{ }\mu\text{g}$
avg. number of carbon atoms lost per shot = $(7.0 \pm 0.7) \times 10^{17}\text{ atoms}$
avg. target thickness ablated per shot = $44.5 \pm 0.4\text{ }\mu\text{m}$

Using the above measurements, the average calculated hole volume over 50 shots can be used to determine the average volume lost per shot. Using the published mass density of 1.84 g/cm^3 for POCO graphite, the average target mass lost per shot was $14.0\text{ }\mu\text{g}$. Finally, neglecting impurities in the graphite ($<5\text{ ppm}$) yields a value for the average number of carbon atoms ablated per shot. Table I summarizes the results of the above measurements and calculations. It should be noted that most of the carbon is ejected long after the laser plasma, composed of low-energy neutrals expanding with an acoustic velocity (see [4]), and would not affect the spectra obtained.

Typical emission spectra are shown in Figs. 3 and 4. Note that each individual spectra is the result of one 50-ns-long OMA gate, centered at the time indicated relative to the peak of the ruby laser pulse. The specific line identifications for Figs. 3 and 4 are given in Tables II and



Fig. 3. Emission spectra of ruby laser produced carbon ablation plasma. Each spectra is the result of one gatewidth, 50 ns long, centered at the times indicated relative to the peak of the ruby laser pulse.

III. In Fig. 3, the CIII lines predominate during the laser pulse (CIV is masked by the major CIII line at 464.7 nm) and then diminish while the CII lines predominate. The CII remains long after the laser pulse, as much as 200 ns for typical cases in the 400- to 500-nm region. The lines originating from the neutral CI were not observed, and this is consistent with the collisional-radiative model discussed in the next section. In Fig. 4, the strong CIV line (at 580.1 nm) is observed during the laser pulse as well as CIII (569.6 nm). Again CII predominates after the laser pulse and then eventually decays.

IV. MODELING

The corona model has sometimes been used to describe the ionization states of laser produced plasmas and their



Fig. 4. Emission spectra of ruby laser produced carbon ablation plasma. Each spectra is the result of one gatewidth, 50 ns long, centered at the times indicated relative to the peak of the ruby laser pulse.

TABLE II
SPECTRAL LINE TRANSITIONS OF FIG. 3

Wavelength		Transition
407.5 nm	CII	$3a^4D^0 \rightarrow 4f^4F$
416.3 nm	CIII	$3p^3D \rightarrow 5f^3F^0$
418.7 nm	CIII	$4f^1F^0 \rightarrow 5g^1G$
426.7 nm	CII	$3a^2D \rightarrow 4f^2F^0$
432.6 nm	CIII	$3e^1P^0 \rightarrow 3a^1D$
437.4 nm	CII	$3a^4P^0 \rightarrow 4f^4D$
451.6 nm	CIII	$4p^3P^0 \rightarrow 5s^3S$
461.9 nm	CII	$3a^2F^0 \rightarrow 4f^2G$
464.6 nm	CIV	$5d^2D \rightarrow 6f^2F^0$
464.7 nm	CIII	$3s^3S \rightarrow 3p^3P^0$
465.8 nm	CIV	$5f^2F^0 \rightarrow 6g^2G$

blow-off regions [3]. Since the corona model is independent of electron density, one cannot determine the electron density from spectroscopic measurements, unlike the LTE where the Saha equation can lead to electron density estimates by comparing intensities of lines resulting from subsequent ionization states. In an experiment by Boland

TABLE III
SOME WAVELENGTH TRANSITIONS (Fig. 4)

Wavelength		Transition
514.5 nm	CII	$3s^4F^o \rightarrow 3p^4P$
564.8 nm	CII	$3s^4F^o \rightarrow 3p^4S$
569.6 nm	CIII	$3p^2P^o \rightarrow 3d^1D$
580.1 nm	CIV	$3s^2S \rightarrow 3p^2P^o$
581.2 nm	CIV	$3s^2S \rightarrow 3p^2P^o$
589.0 nm	CII	$3d^2D \rightarrow 4p^2P^o$

et al. [4], they used a 5-J ruby laser with a pulsewidth of 17 ns to produce ablation plasmas from polyethylene. Assuming LTE conditions, they estimated their electron density to be about 10^{17} to 10^{18} cm^{-3} 1-mm away from their target using absolute intensity measurements. Since our laser pulse was much less energetic than their pulse, we estimate that our electron density is much less than 10^{17} cm^{-3} and that LTE is not valid for our results.

To fill the void between the predominantly collisional LTE model and the corona model, the collisional-radiative model was developed [7]. The CRE model is a comprehensive model that can accommodate lower density plasmas, where radiative effects become significant in determining the ion populations, as well as account for the transitions to higher density LTE conditions. The essential difference between this and the coronal model is that as plasma density increases, the collisional processes become more significant in determining the excited state structure. To account for this, collisional excitation and recombination are included.

A collisional-radiative model for carbon ablation plasmas was developed [8]. The atomic states that provide the basis for the model are the ground state and typically six to 12 of the lowest excited levels of each ion species. In some cases the included levels are representative of a combination of nearby degenerate states. For example, most levels of carbon IV, V, and VI are modeled according to principal quantum number n , that is, the properties of the various nl sublevels have been averaged over angular momentum and magnetic quantum numbers.

The atomic processes that are represented are collisional ionization, three-body recombination, collisional excitation, collisional deexcitation, spontaneous emission, radiative recombination, and dielectronic recombination. They are shown schematically for a simple three-level ion, along with their corresponding transition in Fig. 5. A more detailed discussion of this model is given in [8].

The atomic processes are manifested in a set of rate equations, one for each atomic state, having the form

$$\frac{dn_i}{dt} = \sum_j C_{ji} n_j - \sum_k C_{ik} n_i \quad (1)$$

where n_i is the population density of atomic level i and C_{ij}

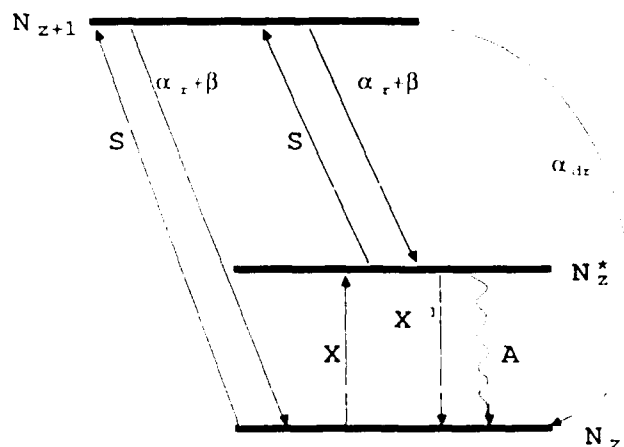


Fig. 5. Three level diagram displaying the atomic processes represented in the collisional radiative model. S is collisional ionization, α_r is radiative recombination, β is three body recombination, α_{dr} is dielectronic recombination, X is collisional deexcitation, and A is spontaneous emission.

is the sum of the reaction rates representing the atomic processes for transitions from state j to i . The rate coefficients C_{ij} 's were obtained from the Naval Research Laboratory data base. The processes and methods used to calculate the rate coefficients have been previously documented by Duston *et al.* [9]. It is assumed that the equilibrium nature of the CRE model is valid for this experiment; i.e., the left-hand side of (1) is a set equal to zero. This assumption is justified because the hydrodynamic time scales estimated from the time-resolved emission spectra studies are long in comparison to the relaxation times of atomic states.

Once the equations are solved for the population densities, it is a straightforward calculation to find the effective charge, specific states, ionization energy, radiation field, and other information that depends upon knowledge of the populations.

We have included radiative cooling due to line recombination and bremsstrahlung radiation for the simulations described in this paper; however, since no transport of radiation is performed, the model is only strictly valid for optically thin plasmas. It should also be mentioned that we have neglected the explicit effect of reduced ionization potentials. This approximation could have an impact upon higher density results.

V. Discussion

Fig. 5 shows the ion concentration of successive ionization stages of carbon for an overall electron density of 10^{17} cm^{-3} calculated using the CRE model. A rough estimate of the temperature can be made by noting the absence and presence of certain ionization stages. For example, in Fig. 4, CIV dominated during the pulse and CII after the pulse, with the presence of CIII occurring at times in between. From Fig. 6 one can estimate the range of the electron temperature to be about 10–12 eV during the pulse (based upon the fact that CIV predominates over CIII), decreasing to 3–5 eV within 50 ns. At electron

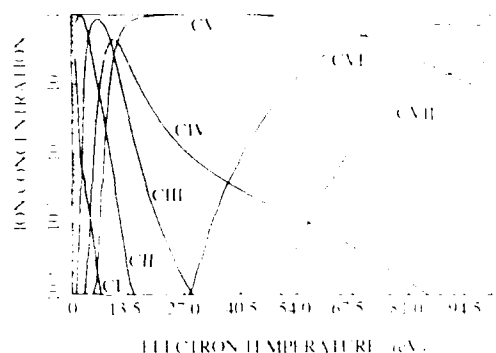


Fig. 6. Ion abundance curves for a total ion density of $1 \times 10^{17} \text{ cm}^{-3}$ as calculated from the collisional-radiative equilibrium model.

densities between 10^{12} and 10^{15} cm^{-3} the ion concentrations do not change significantly with temperature and thus these temperature estimates remain about the same regardless of the density in this region. Note that even at 4 eV, the CI concentration is 0.01 that of CII, so it is not surprising that CI is never observed. By the time the plasma has cooled and recombined to the point that CI would be observed, the plasma has moved out of the field of view of the spectrograph.

A more accurate estimate of the electron temperature as a function of time was made by comparing the intensities of two experimentally measured lines to intensities calculated from the population densities predicted by the CRE model for a plasma with $n_e = 10^{12} \text{ cm}^{-3}$. The digitally integrated intensities of the two largest lines (CII at 427 nm and CIII and 465 nm) were used. The results are illustrated in Fig. 7. The resolution of the optical system was not adequate to determine if any other species contributed to these lines, so we assumed that these states were the sole contributors to the observed lines. Nevertheless, the temperatures do fit an exponential decay (denoted with the smooth line) after a peak value, as would be expected. The e-folding time for the decay of the plasma temperature was found to be about 90 ns. Also, the approximately 20-ns delay in the peak temperature corresponds to a streaming velocity of $7.5 \times 10^6 \text{ cm/s}$ which agrees very well with the streaming velocity of $8.4 \times 10^6 \text{ cm/s}$ obtained for conditions similar to this experiment using a Faraday cup [10]. The temperatures shown in Fig. 7 are well within the range of those expected for a laser irradiance of 10^{10} W/cm^2 [11].

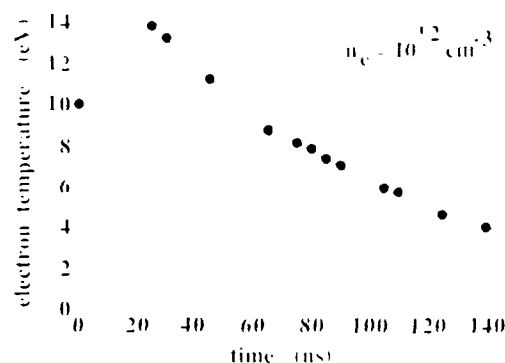


Fig. 7. Electron temperature of the laser-ablated carbon plasma versus time relative to the peak of the ruby laser output, obtained by comparing the CII (427 nm) and CIII (465 nm) intensities to those calculated from excited state densities predicted from the CRE model. The curve describes an exponential fit to the data.

This paper has shown that plasma temperature can be obtained from plasmas whose parameters fall between the region of validity for the LTE and corona models by comparing spectroscopic data to excited state densities predicted by the comprehensive CRE model. This opens up the possibility of diagnosing a variety of plasmas that traditionally have been difficult to diagnose because of their plasma parameters.

REFERENCES

- [1] M. Brake, R. Gilgenbach, L. Horton, and J. Tucker, *Plasma Chem. Plasma Proc.*, vol. 3, no. 4, p. 367, 1983.
- [2] H. Milchberg, C. Skinner, S. Suckewer, and D. Voorhees, *Appl. Phys. Lett.*, vol. 47, p. 115, 1985.
- [3] B. Sinha, *J. Appl. Phys.*, vol. 52, p. 5010, 1981.
- [4] B. Boland, F. Irons, and R. McWhirter, *J. Phys. B*, vol. 1, p. 1180, 1968.
- [5] J. Ready, *Effects of High-Power Laser Radiation*. New York: Academic, 1971, p. 121.
- [6] R. McWhirter, "Spectral intensities," in *Plasma Diagnostic Techniques*, R. Huddleston and S. Leonard, Eds. New York: Academic, 1965.
- [7] D. R. Bates, A. E. Kingston, and R. W. P. McWhirter, *Proc. Roy. Soc.*, vol. A257, p. 297, 1962.
- [8] W. Thornhill, Ph.D. dissertation, Univ. of Michigan, Ann Arbor, MI, 1985.
- [9] D. Duston, R. Clark, J. Davis, and J. Apruzese, *Phys. Rev. A*, vol. 27, p. 1441, 1983.
- [10] J. Meachum, Ph.D. dissertation, Univ. of Michigan, Ann Arbor, MI, 1986.
- [11] J. Ready, *Effects of High-Power Laser Radiation*. New York: Academic, 1971, p. 194.

Effects of helium upon electron beam excitation of N_2^+ at 391.4 and 427.8 nm

M. L. Drake, R. M. Gilgenbach, R. E. Lucy, Jr., K. Pearce, and T. Repetti
Intense Energy Beam Interaction Laboratory, Department of Nuclear Engineering, University of Michigan,
Ann Arbor, Michigan 48109

P. E. Sojka
Department of Mechanical Engineering, Purdue University, West Lafayette, Indiana 47907

(Received 20 June 1986; accepted for publication 23 July 1986)

Relativistic electron beam interactions with very small ratios of nitrogen to helium (10^{-1} – 10^{-3}) have been found to produce extremely large N_2^+ ($B^2\Sigma_u^+ \rightarrow X^2\Sigma_g^+$) intensities at 391.4 and 427.8 nm, compared to line intensities originating from helium. These results occurred in the total pressure regime of 0.1–500 Torr. The pressure scaling results presented here are inconsistent with previously proposed kinetic mechanisms for the N_2^+ laser pumped by helium. With a simple model of the chemical kinetics, we show that this effect is due to the collisional transfer of energy between excited states of helium atoms and the ground state of N_2^+ .

It is well known that population inversions of the $B^2\Sigma_u^+ \rightarrow X^2\Sigma_g^+$ electronic transition of N_2^+ can be achieved in the presence of helium.¹ Two possible mechanisms have been used to describe the pumping process. Collins¹ believes the upper laser level is pumped by charge transfer from He_2^+ to N_2 . Kokawa *et al.*² believe that electron impact excitation is the dominant pump mechanism. Most of the research performed on the N_2^+ laser has involved large overall He– N_2 discharge pressures (1–36 atm)^{1–3} where the presence of He_2^+ may be feasible. Investigations of lower (< 50 Torr) overall pressures, however, have observed population inversions in atomic nitrogen^{4–6} rather than in molecular nitrogen. Population mechanisms proposed for atomic nitrogen lasers range from excitation of nitrogen atoms by collisions between metastable excited atoms of helium (2^1S) and nitrogen molecules⁵ to the recombination of electron-ion pairs.⁴ In this letter, we present intensity measurements for a wide range of helium to nitrogen ratios for relativistic electron beam pumped gases in the intermediate pressure range of 0.1–500 Torr and show that these results are inconsistent with the above mentioned mechanisms. We also present a simple chemical kinetic model which is consistent with our experimental observations.

The experimental apparatus has been described previously.⁷ The experiment consisted of a relativistic electron beam at a peak voltage of 300 keV, a peak current of 1 kA, and a pulse width of 300 ns. The diode consisted of a 2.5-cm-diam carbon brush cathode and a 0.025-mm titanium anode foil. The beam was injected into an aluminum vacuum vessel with lucite windows on the sides and end. The emitted light at several helium partial pressures each with nitrogen partial pressures of 0.1, 1, and 10 Torr was sampled axially. The light was analyzed by a 0.275-m spectrograph coupled to an optical multichannel analyzer (OMA). The OMA was gated with pulses of 50 and 500 ns.

For all experiments where helium was present with small to large amounts of nitrogen, two very intense lines were observed at 391.4 and 427.8 nm. These lines correspond to the $(0,0)$ and $(0,1)$ vibrational transitions in the first

negative band of N_2^+ , $B^2\Sigma_u^+ \rightarrow X^2\Sigma_g^+$. Lines originating from atomic or molecular helium had negligible intensities for these cases. When no nitrogen was present, the major lines were attributed to neutral atomic helium at 388.8, 447.1, 501.5, and 587.5 nm. In time-resolved studies performed with OMA gates of 50 ns delayed by 20 ns for each pulse, the N_2^+ light emission was found to follow the beam voltage after the initial rise time (see Fig. 1). During the time-resolved studies, no other lines were observed except for the 391.4- and 427.8-nm nitrogen lines. Figure 2 shows the relative intensity of the 391.4-nm band as a function of helium to nitrogen ratio for nitrogen partial pressures of 0.1, 1, and 10 Torr. Figure 3 shows similar results for the 427.8-nm band.

As seen in Figs. 2 and 3, the largest light intensities at 391.4 and 427.8 nm for a given pressure of nitrogen occur for the largest ratio of He/ N_2 . That is, the more helium present, the more light is produced up to total pressures of about 300 Torr where the intensity levels off. The linear portion of the curves corresponds to a slope of about 1 for the range of total

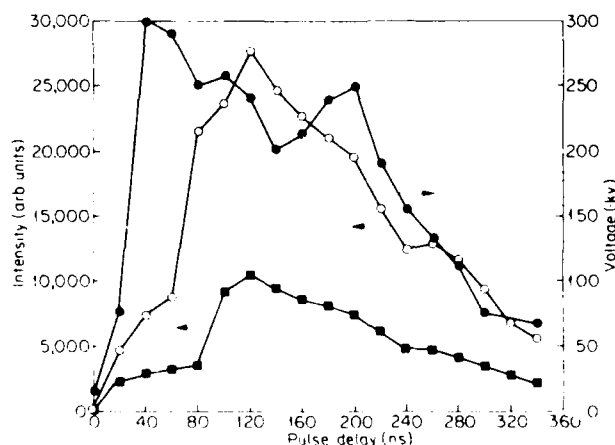


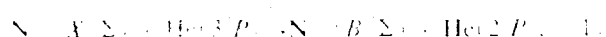
FIG. 1. Beam voltage (●) and 391.4 nm (○) and 427.8 nm (■) emission band intensities as a function of time. The partial pressures of N_2 and helium were 0.5 and 100 Torr. Optical multichannel analyzer gates were 50 ns and times plotted are for the center of the gate.



FIG. 2. Intensity of the 394.4 nm emission as a function of the He/N ratio for N_2 pressures of 0.1 Torr (\circ), 1 Torr (\square), and 10 Torr (\triangle). The slopes of the linear portions of the curves are indicated.

pressure, 10–300 Torr, the case where the N_2 partial pressure was 1 and 0.1 Torr. The slope was 0.5 when the partial pressure of N_2 was 10 Torr. For cases where the helium partial pressure is smaller or about the same as the nitrogen partial pressure, there is very little increase in the intensity of the N_2 lines compared to the case of nitrogen alone.

As mentioned previously, the largest intensity lines observed when no added nitrogen was present were 388.3, 447.1, 501.5, and 587.5 nm. In the case of the 388.8 nm line, the energy of this transition is very close to that of the N_2 501.4-nm band. Therefore, a possible mechanism for the excitation of this band is



where k_1 is the reaction rate constant. Since the slope of the log of the intensity as a function of the log of He/ N_2 is close to 1 for the small N_2 partial pressure cases, there appears to be a one-to-one correspondence between the number of photons emitted for the given bands and the number of helium atoms present, above a particular helium to nitrogen threshold. This one-to-one correspondence is consistent with reac-

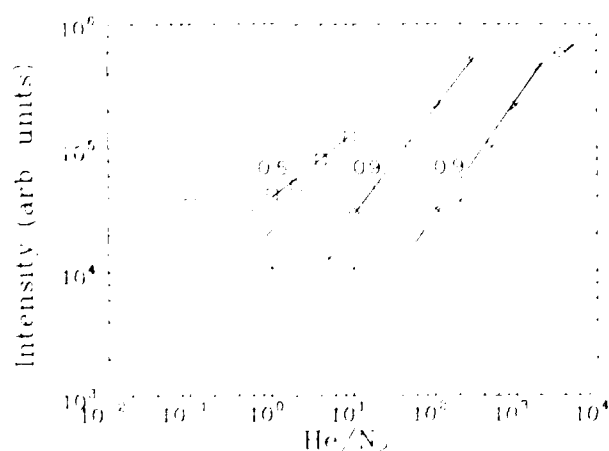
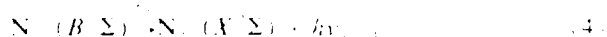


FIG. 3. Intensity of the 427.8 nm band emission as a function of He/ N_2 ratio for N_2 pressures of 0.1 Torr (\circ), 1 Torr (\square), and 10 Torr (\triangle). The slopes of the linear portions of the curves are indicated.

tion (1) as illustrated by a simple kinetic model. Assume that the electron beam excites the helium from the ground state to the 3^1S state as follows:



where k_2 is the rate constant for reaction (2) and is a function of the electron beam energy. At low pressures, the main deactivation mechanism of $He(3^1P)$ and $N_2(B^2\Sigma)$ is radiative decay:



Note that $He(2^1S)$ is a metastable state. We also make the following assumptions: all back reactions are negligible; collisional decay of $He(3^1P)$ is unimportant because the exchange reaction $He(3^1P) + He(2^1S) \rightarrow He(2^1S) + He(3^1P)$ does not alter the $He(3^1P)$ concentration; the collisional quenching of $N_2(B^2\Sigma)$ is unimportant for low pressures (although this assumption is discussed later); and that the electron beam density can be approximated by an exponential of the form $[e^-] = [e^-]_0 e^{-wz}$, where $[e^-]_0$ is some constant characteristic of the beam density and w and z are constants which describe the beam current temporal profile. We now write a differential equation for $He(3^1P)$ as

$$\frac{d[He(3^1P)]}{dt} = k_2[He(1^1S)]\{[e^-]_0(e^{-wz} - e^{-wz_0})\} - k_1[He(3^1P)] - k_1[He(3^1P)][N_2(X^2\Sigma)] \quad (5)$$

Now assume that the ground-state populations $He(1^1S)$ and $N_2(X^2\Sigma)$ stay approximately constant. Then a linear, homogeneous, ordinary differential equation exists for $[He(3^1P)]$ and can be solved using standard techniques. The solution is

$$[He(3^1P)] = A \left(\frac{e^{-wz_0} - e^{-wz}}{k_1 - w_1} - \frac{e^{-wz_0}}{k_1 - w_1} + \frac{e^{-wz}}{k_1 - w_1} - \frac{e^{-wz}}{w_1} \right) \quad (6)$$

where $k_1 = k_1[N_2(X^2\Sigma)] + k_1$ and $A = k_2[He(1^1S)] \cdot [e^-]_0$. We can also write the rate equation for $[N_2(B^2\Sigma)]$:

$$\frac{d[N_2(B^2\Sigma)]}{dt} = k_1[N_2(X^2\Sigma)][He(3^1P)] - k_1[N_2(B^2\Sigma)] \quad (7)$$

Substituting $[He(3^1P)]$ from Eq. (6) and solving for $[N_2(B^2\Sigma)]$ gives

$$[N_2(B^2\Sigma)] = k_1[N_2(X^2\Sigma)][He(1^1S)][e^-]_0 \cdot \left(\frac{(w_1 - w_1)(e^{-wz_0} - e^{-wz})}{(k_1 - w_1)(k_1 - w_1)(k_1 - k_1)} + \frac{e^{-wz_0} - e^{-wz}}{(k_1 - w_1)(k_1 - w_1)} - \frac{e^{-wz_0} - e^{-wz}}{(k_1 - w_1)(k_1 - w_1)} \right) \quad (8)$$

A rate equation for the time rate of change of the photon emission at 391.4 nm can be written as

$$\frac{d[\dot{N}(391.4)]}{dt} = k_1[N_2(B^3\Sigma)] - k_2[\dot{N}(391.4)] \quad (9)$$

Substituting the results of Eq. (8) gives

$$\frac{d[\dot{N}(391.4)]}{dt} = k_1 \left(\frac{1}{k_3 + k_4} \right) \left(\frac{1}{k_5 + k_6} \right) [N_2(B^3\Sigma)] [\text{He}(1S)] [e^-] - k_2[\dot{N}(391.4)] \quad (10)$$

It is seen that $\dot{N}(391.4)$ is linearly proportional to $[\text{He}(1S)]$ and that, because of the electron beam, the $N_2(B^3\Sigma)$ is a constant population. If $N_2(B^3\Sigma)$ is included as

$$N_2(B^3\Sigma) = M/(k_3 + k_4) \quad (11)$$

then the rate equation becomes $\dot{N}(391.4) = k_1 k_5 / (k_2 k_3 + k_2 k_4 + k_1 k_5) [M] [\text{He}(1S)]$. The rate of change of M is a function of the partial pressures of He or N_2 . Equation (11) shows that the rate of change of M has a complicated dependence on the partial pressures of the gases. In the simple linear case shown in Fig. 1, the rate of change of M is due to the effects of collisional excitation of $N_2(B^3\Sigma)$. If the assumption that $N_2(B^3\Sigma)$ is constant would require accurate rate constants for the depopulation of the differential equation.

Another important result of the data shown in Figs. 2 and 3 is that as the nitrogen partial pressure increases, the overall amount of line enhancement decreases, as well as the slope of the linear part of the intensity versus pressure ratio curves. For nitrogen partial pressures of 0.1 Torr, the emitted intensity increases by almost a factor of 100 whereas for nitrogen partial pressures of 10 Torr, the overall increase is less than a factor of 10 compared to the no helium case. It appears that a very important collisional depopulating mechanism of $N_2(B^3\Sigma)$ is collisions with other nitrogen molecules.

Never at any time was emission due to He^+ or postulated He^- (see Ref. 6) observed. This, in addition to the fact that the highest overall pressure examined was 500 Torr, leads to

the conclusion that charge transfer between He^+ was probably negligible, also since for example the 388.8-nm helium line which populates the metastable state of helium was not observed to increase or decrease with the 391.4-nm band, in contrast to the results of Atkinson and Sanders.⁷ Instead, the 388.8-nm helium line was observed only in the absence of nitrogen, thus it is doubtful that direct transfer between the metastable state of helium (2^3S) and the $N_2(B^3\Sigma)$ was significant. Kokawa *et al.*⁸ claim that electron impact ionization is the major pumping process and that the presence of helium only helps to raise the electron temperature rather than supplying reactants for the pumping process. The results presented here show a definite helium dependency, particularly since we have shown previously⁷ that the electron temperature is pressure insensitive for our e-beam produced discharges.

Relativistic electron beam produced plasmas in helium-nitrogen mixtures produce very large intensity lines at 391.4 and 427.8 nm. These lines originate from the vibrational transition of (0,0) and (0,1) in the first negative system of N^+ . The line intensities increase as the ratio of helium to nitrogen increases. The greatest increase is seen for the lowest nitrogen concentrations. The increased intensity is linear with helium pressure between the total pressure of 10–300 Torr for small partial pressures (0.1–1.0 Torr) of nitrogen. This increase is believed to be due to collisional transfer of energy between helium excited states and the N^+ ground state as shown by the agreement between our simple kinetic model and experimental results.

This project was funded by National Science Foundation grants No. ECS-8504483 and No. ECS-8351837 and Air Force Office of Scientific Research 86-0012. The authors acknowledge equipment assistance from the Naval Research Laboratories.

⁷C. Collins, IEEE J. Quantum Electron., **QE-20**, 47 (1984).

⁸M. Kokawa, M. Saito, S. Horiguchi, and T. Nakaya, J. Phys. D, **18**, 177 (1985).

⁹J. Atkinson and J. Sanders, J. Phys. B (Proc. Phys. Soc.), Ser. 2, **1**, 117 (1968).

¹⁰G. Cooper and J. Verdeyen, J. Appl. Phys., **48**, 1170 (1977).

¹¹M. Brake, T. Repetti, K. Pearce, and R. E. Lucey, Jr., J. Appl. Phys., **60**, 99 (1986).

¹²J. Lucker, M. Brake, and R. Gilgenbach, J. Appl. Phys., **59**, 2251 (1986).

Fast, sensitive laser deflection system suitable for transient plasma analysis

C. L. Enloe, R. M. Gilgenbach, and J. S. Meachum

*Intense Energy Beam Interaction Laboratory, Department of Nuclear Engineering,
The University of Michigan, Ann Arbor, Michigan 48109-2104*

(Received 11 May 1987; accepted for publication 26 May 1987)

A laser deflection measurement system has been developed which is both fast ($\tau \approx 20$ ns) and sensitive ($\delta\theta \approx 0.5 \mu\text{rad}$). This diagnostic is capable of sensing and discriminating between electrons and neutral particles in a multicomponent plasma, and yields quantitative results. The technique allows continuous measurements in time. Construction is inexpensive and simple to field. This system is, therefore, highly competitive with traditional techniques in diagnosing the development of transient plasmas.

INTRODUCTION

Investigation of the time evolution of the plasma produced by the interaction of a high-power laser with a target is an example of a situation in which a fast, versatile probe of plasma density is desirable. Such a plasma is short lived, since the plasma is expanding with a velocity on the order of $10 \text{ cm } \mu\text{s}$, and composed of different components. In particular, at early times a dense plasma exists, whereas at late times the presence of a neutral component is significant.

The common technique of pulsed laser schlieren photography¹ is inadequate to diagnose the temporal evolution of such a plasma in a single shot. Although fast (20-ns) "shuttering times" can be obtained by employing a Q -switched ruby laser, many identical plasma shots are required, varying the timing of the probe laser, to observe the plasma evolve in time. In many cases, difficulties arise because of the neutral component, since the presence of a plasma is a negative perturbation in the index of refraction while the presence of neutral particles is a positive perturbation. If a pinhole is used as a spatial filter in a schlieren system, the technique can simultaneously detect both plasmas and neutrals, but cannot distinguish between them. If a knife edge is used as a spatial filter, the technique can distinguish between the two but cannot detect them simultaneously. Further, it is difficult to obtain quantitative results from schlieren photography.¹ Applying the technique of holographic interferometry² eliminates these difficulties, but at the expense of a large increase in cost and complexity, since not only are the laser optics required to make the hologram more complex, but the hologram must be reconstructed in order to interpret the results.

Diagnosing density by measuring the deflection of a laser beam³⁻⁵ is an analogous technique to schlieren photography, in that both techniques are sensitive to index of refraction gradients. The technique has been successfully applied to a number of fields,⁶ the chief impediment to its application to transient plasmas has been one of speed. In this article, we present a laser deflection system capable of detecting deflections of $0.5 \mu\text{rad}$ on a time scale of 20 ns. Hence, its speed is comparable to Q -switched ruby laser schlieren, while its sensitivity is over two orders of magnitude greater. It is inher-

ently quantitative, while at the same time being much simpler and less expensive to implement than a ruby laser and associated optics.

I. LASER DEFLECTION TECHNIQUE

Figure 1 illustrates the laser deflection technique applied to a laser-produced plasma. The target material is produced by focusing the output of a Q -switched ruby laser on a graphite surface. A 5-mW He-Ne probe laser (Jodon Laser model HN-2SHP) is deflected by index of refraction gradients as it passes through the laser-produced plasma. The angular deflection is given by⁶

$$\delta\theta = \frac{1}{\bar{n}_0} \int_{\text{path}} ds \nabla \cdot \hat{n} = \frac{D \langle \nabla \cdot \hat{n} \rangle}{\bar{n}_0}, \quad (1)$$

where \hat{n} is the index of refraction, \bar{n}_0 is the unperturbed index of refraction (approximately equal to 1), $\nabla \cdot \hat{n}$ is the gradient in the index of refraction perpendicular to the path of the beam, D is the thickness of the plasma, and $\langle \rangle$ indicates a line average taken over the path of the probe laser in the plasma. Since deflections are small, this average is taken over the straightline unperturbed path. The deflection of the

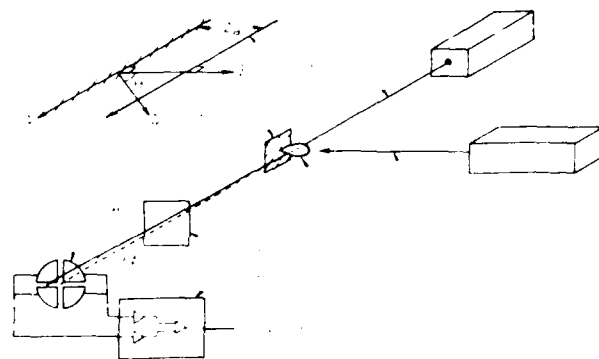


Fig. 1. Experimental configuration and coordinate system used for analysis. (a) He-Ne probe laser beam, (b) carbon target, (c) Ruby laser beam, (d) Laser produced plasma, (e) Quadrant detector, (f) Differencing and amplifying circuitry, (g) He-Ne laser line filter.

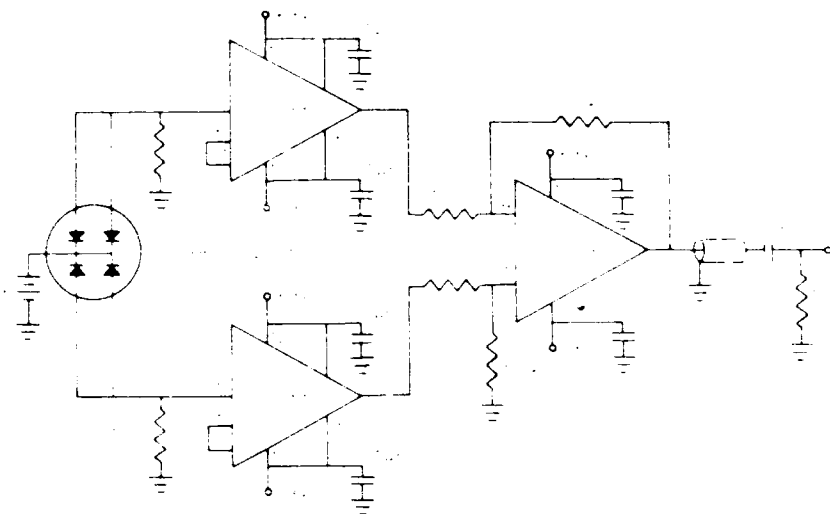


Fig. 2. Detector circuit. Input impedance is $100\text{ k}\Omega$. Output impedance is $200\text{ k}\Omega$. $H = 50\text{ }\Omega$.

beam is detected by a position sensor, specifically a quadrant detector (Silicon Detector Corporation model SD-380-23, 21% 50° class) for its fast response time. The sensor and its associated electronics are located a distance L from the plasma. Although the design of the detector circuit is inherently neutral, a standard He-Ne laser line filter is used in front of the position sensor to maximize detector sensitivity by eliminating ricker and halft. The output of the detector is proportional to the deflection δl , $V_{out} = G\delta l/l$, where the constant G is readily calibrated.

For plasmas, the change in index of refraction δn is proportional to the electron density n_e and is given by

$$\delta n = \left(\frac{e^2}{2\pi m} \right) \frac{1}{\omega^2} n_e = K_e n_e, \quad (2)$$

where e is the electron charge, m is the electron mass, and ω is the laser frequency, so that $K_e = 1.79 \times 10^{-11} \text{ cm}^3$ for He-Ne laser light. For neutral particles, δn is proportional to the neutral density n_n and is given by

$$\delta n = \left(\frac{n_n - 1}{n} \right) n_n = K_n n_n. \quad (3)$$

At STP, the neutral density $n_n = 2.6868 \times 10^{19} \text{ cm}^{-3}$ and $(n_n - 1)/n = 2.76 \times 10^{-4}$ for He-Ne laser light, so that $K_n = 1.0272 \times 10^{-11} \text{ cm}^3$.

The key to the performance of this system is the detector circuit, shown in Fig. 2. The quadrant detector is essentially four photodiodes on one substrate. Each pair of anodes on either side of the vertical midplane are connected, so that the detector is sensitive only to horizontal deflections of the probe laser. A bias voltage of 30 V applied to the common connection reduces the output capacitance, and hence the response time, of the detector. Voltage is developed across a $275\text{-}\Omega$ resistor on each side. This resistance value was chosen to optimize the gain-bandwidth product of the system. The signal from each side is buffered and passed on to a $15\text{-}\mu\text{V}$ -gain differential amplifier. Since a differential configuration is used, the detector is insensitive to common-mode noise such as variation in probe laser power. The amplifier is capable of driving a $50\text{-}\Omega$ load to approximately $\pm 1\text{ V}$. A high-pass

filter is used to eliminate the effects of mechanical vibrations ($< 20\text{ Hz}$) from the output.

The sensitivity of the system is a function of laser power and spot size. It generally increases as the moment arm L ; however, for large L , the effect of beam divergence is large and the advantage of the long arm diminishes. For the laser employed, $L \approx 3\text{ m}$ appears to be optimum, yielding $dV/d\theta = 4.2\text{ mV}/\mu\text{rad}$. Since the output noise level is approximately 2 mV , the resolution of the system is approximately $0.5\text{ }\mu\text{rad}$. For comparison, consider a typical schlieren system with a 500-mm focal length lens and a $100\text{-}\mu\text{m}$ pinhole. If we assume that the minimum detectable deflection is equivalent to a one- f -stop change in density on the film, then the resolution of this schlieren system is approximately $100\text{ }\mu\text{rad}$. Therefore, the laser deflection technique offers higher resolution than the schlieren technique by over two orders of magnitude.

The time response of the system was tested by masking one side of the detector at a time and using the detector to view a highly attenuated ruby laser pulse, comparing the output to that of a fast (2-ns rise time) PIN diode. The results are shown in Fig. 3. Using the formula for the addition of rise times,

$$\tau_{out} = \left(\sum_i \tau_{ti}^2 \right)^{1/2} = (\tau_{laser}^2 + \tau_{detector}^2)^{1/2}, \quad (4)$$

we find that the response time of the circuit itself is approximately 20 ns. Differences in light path lengths to the detec-

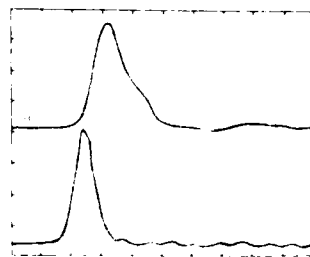


Fig. 3. Response of one side of the position sensor to a ruby laser pulse, 50 mV/div , compared to the response of a fast PIN diode to the same pulse, 100 mV/div . The response of the other side of the position sensor is approximately 10 ns slower than the other side, due to the difference in light path lengths.

tors, cable lengths from the detectors to the oscilloscope, and relative timing between the oscilloscope channels account for less than 1 ns in the timing difference between the signals. A fixed circuit delay of approximately 30 ns is, therefore, apparent.

II. APPLYING THE TECHNIQUE TO A MULTICOMPONENT PLASMA

Since the laser deflection technique yields information about density gradients, for any arbitrary configuration, it is possible to probe the plasma at a number of positions over a number of shots and integrate $d\delta/dx$ over space to obtain the density distribution. However, in many cases, it is possible to obtain density information on a single shot, if the density as a function of time can be cast in the form of

$$n(x, y, z, t) = S(x, y, z) f(t), \quad (5)$$

where n is the density as a function of space and time, S is a scaling factor, and f is a function which describes the shape of the plasma as a function of time. For example, in the case of a laser-produced plasma, a self-similar expansion model¹² can be used and applied to each species:

$$n_i = \frac{N_i}{V_i} \frac{V_i^3}{(V_i + v_i t)^3} \exp\left\{-\frac{R^2}{(V_i + v_i t)^2}\right\} \left[1 + \frac{1}{2} \left(\frac{v_i}{V_i}\right)^2 \sin^2 \theta + 1\right], \quad (6)$$

where n_i is the density of the i th species, N_i is the total number of that species produced by the laser, v_i is the characteristic expansion velocity of that species normal to the target surface, and θ is the ratio of parallel to perpendicular velocities for that species. Figure 1 illustrates the coordinate system. The characteristic expansion velocity is largely independent of the number of each species produced in a given pulse; therefore, V_i is the scaling factor, and the remainder of the expression describes the spatial and temporal shape of the plasma. For the plasma under consideration, k_\parallel has been measured¹³ and is equal to 2, while k_\perp is taken to be 1. Using the transformation applicable to this geometry,

$$\nabla n = \frac{Z}{R} \frac{dn}{dR}, \quad (7)$$

where Z is the distance from the laser to the target, Eq. (1) becomes

$$\delta\theta = 2Z \int_{-\pi/2}^{\pi/2} d\theta \frac{1}{V_i + v_i t} \frac{dn}{n dR}. \quad (8)$$

Using the transformation

$$R = [(\theta + 1) \sin^2 \theta + 1]^{1/2} Z, \quad Z_\parallel = k_\parallel Z, \quad (9)$$

and using Eqs. (5) and (6), the angular deflection is given by

$$\delta\theta = \frac{2Z}{V_i + v_i t} \frac{4\pi k_\parallel Z K}{(V_i + v_i t)^2} \exp\left[-\frac{4Z^2}{(V_i + v_i t)^2}\right] f(t). \quad (10)$$

Defining τ with respect to time, the peak deflection will occur when $t = t_p$, where

$$\frac{d}{dt} \left(\frac{1}{V_i + v_i t} \right) = 0. \quad (11)$$

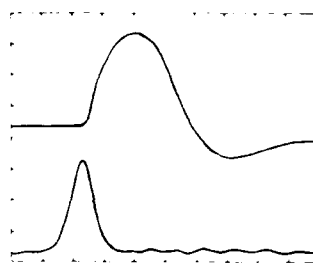


Fig. 4. (a) Position sensor output (50 mV/div). Positive excursion is due to plasma, while negative excursion is due to neutral particles. Light attenuation is used to limit sensitivity of the sensor to 0.80 mV/ μ rad in this case. (b) PIN diode signal of the ruby laser pulse producing the plasma under investigation (100 mV/div).

Hence, the expansion velocity for each species can be determined from the timing of the peak deflection due to that species, and using that velocity in Eq. (10), the number of each species produced by the laser is given by

$$N_i = \delta\theta \left(\frac{\pi \exp(2)}{16} \right) \frac{Z_\parallel^2}{K k_\parallel} = 1.45 \delta\theta \frac{Z_\parallel^2}{K k_\parallel}, \quad (12)$$

where $\delta\theta_i$ is the peak angular deflection for each species.

An example of the experimental data is shown in Fig. 4. In this case, the orientation of the detector is such that the plasma electrons produce a positive deflection, while the neutral particles produce a negative deflection. (On shots where the ruby laser power fell below the threshold for plasma production, only the negative deflection was observed.) The detector was mounted 3.18 m from the target, and the detector sensitivity was calibrated at 4.0 mV/ μ rad; however, because of the large gradients involved, light attenuating filters were used in front of the detector to derate the sensitivity to 0.80 mV/ μ rad. For this particular shot, $Z_\parallel = 0.192$ cm. One sees that the initial plasma peak is distinct from the later neutral peak, and that the plasma velocity is significantly higher than the neutral velocity. Using Eqs. (11) and (12), one finds that the characteristic velocities are $v_p = 3.0$ cm/ μ s and $v_n = 0.42$ cm/ μ s, while the number of particles produced by the laser are $N_p = 8.09 \times 10^{14}$, and $N_n = 3.76 \times 10^{16}$. The latter data correspond to peak densities along the path of the probe laser of $n_p = 6.3 \times 10^{16}$ cm⁻³ and $n_n = 7.3 \times 10^{17}$ cm⁻³ for the plasma and the neutral particles, respectively. These data are consistent with Faraday cup measurements of charged particles¹² and estimates of plasma density obtained spectroscopically as well as neutral particle density estimated from the size of the hole bored in the target by the ruby laser.¹

ACKNOWLEDGMENTS

This research was supported by NSF, ONR, and AFOSR. One of the authors (C.L.F.) was supported by AFH/CIRD. The authors especially thank R. Spears for assistance in design and construction of the detector circuit.

1. M. J. Berger, J. S. MacGowan, R. M. Golombek, and W. H. Gold, *IEEE Trans. Plasma Sci.*, **PS-15**, 73 (1987).
2. R. H. Hordless et al. and S. L. Leonard, *Plasma Diagnostics Technology*, Academic, New York, 1987.
3. J. D. Horton and R. M. Golombek, *Phys. Fluids* **25**, 1702 (1982).

- 1600

**Microscopic and Macroscopic Material Property Effects
on Ultraviolet-Laser-Induced Flashover of Angled
Insulators in Vacuum**

**C. L. Enloe
Ronald M. Gilgenbach**

Reprinted from
IEEE TRANSACTIONS ON PLASMA SCIENCE
Vol. 16, No. 3, June 1988

Microscopic and Macroscopic Material Property Effects on Ultraviolet-Laser-Induced Flashover of Angled Insulators in Vacuum

C. L. ENLOE AND RONALD M. GILGENBACH, MEMBER, IEEE

Abstract—Flashover of electrically stressed polymeric insulators in vacuum has been induced by ultraviolet radiation from an excimer laser (KrF). Flashover behavior is a relatively strong function of integrated fluence up to the time of flashover initiation, and virtually independent of applied power or pulse time. Flashover is induced by moderate fluence (10–150 mJ/cm²) of intense (0.4–6 MW/cm²) ultraviolet at 248 nm at electric field stress considerably below the static breakdown stress. The critical fluence required to initiate flashover is a function of the electric field stress, the insulating material, and the geometry of the dielectric vacuum interface. The unconventional insulator geometry (in which electrons are accelerated toward the insulator surface) is more tolerant than the conventional geometry by nearly a factor of 2 in fluence. Insulator materials tested were polyethylene, polystyrene, acrylic, nylon-6, acetal, PVC, and teflon. The critical fluence is correlated to the microscopic and macroscopic material properties; results show that insulating materials with high dielectric constants and low secondary electron emission coefficients exhibit superior tolerance to ultraviolet radiation. Of the materials tested, nylon exhibited the highest critical fluence in both the conventional and the unconventional geometries. A theory of ultraviolet-induced insulator flashover is developed.

I. INTRODUCTION

THE PHENOMENON of flashover at the electrically stressed interface of a solid dielectric and vacuum has been well-characterized [1]–[7], although investigations continue into the mechanisms involved. It is an important phenomenon to understand, since the dielectric/vacuum interface is electrically weaker than either the dielectric or the vacuum gap alone and hence may be the limiting element in a high-voltage power transport system. Numerous factors affect the flashover of insulators in vacuum, including the composition of the dielectric material [6], insulator surface conditioning and modification [4]–[11], and the time history of the voltage pulse (whether nanosecond or microsecond duration or dc, unipolar or bipolar) [11], [13]–[15], but the chief factor in determining insulator flashover performance is the geometry of the dielectric vacuum interface [3]–[7], [16].

A large number of insulator and electrode geometries

have been investigated [16], but the most common in application is the plane insulator/vacuum interface between plane parallel electrodes. In this configuration, flashover strength is a strong function of the acute angle θ between the insulator surface and the normal to the electrode surfaces ($-90^\circ < \theta < 90^\circ$). A wide variety of dielectric materials, including polymers, glasses, metal oxides, and composites, exhibit similar behavior; flashover strength is at a minimum for $\theta \approx 0^\circ$ and has two maxima at $\theta \approx \pm 45^\circ$ [3]–[6]. Since flashover strength is typically greater for $\theta = +45^\circ$ than for $\theta = -45^\circ$, the positive angle configuration is conventionally employed. The sign convention is illustrated in Fig. 1. For $\theta > 0$, electrons originating on or near the insulator surface are accelerated away from the insulator surface, while for $\theta < 0$ they are drawn toward the insulator surface. Note that because of the presence of the dielectric, the angle θ_k between the local electric field and the insulator surface is in general neither equal to θ nor constant over the surface of the insulator. The local electric field may be significantly altered by the presence of charge on the insulator surface.

The flashover performance of polymeric insulators in vacuum is seriously degraded if the dielectric/vacuum interface is exposed to ultraviolet radiation while voltage is applied [17]–[21]. Unlike visible light, ultraviolet radiation penetrates a very short distance into the surface of a polymer [22], so that interaction products (electrons and neutral particles) are readily ejected into the vacuum. Flashover has been induced over angled insulators exposed to modest fluence (10–150 mJ/cm²) of intense (0.4–6 MW/cm²) ultraviolet radiation even at low electric field stress (10–80 kV/cm). Further, the reverse of the behavior one might expect is observed—insulators at negative angle are more tolerant to ultraviolet illumination than are insulators at positive angle.

In this work, we present the results of an experiment which 1) quantifies the effects of ultraviolet illumination on polymeric insulators, 2) characterizes in detail ultraviolet-induced flashover over insulators at positive and negative angles, and 3) correlates microscopic and macroscopic material properties to flashover behavior. A theory of ultraviolet-induced insulator flashover is developed, which explains the unexpected variation of flashover strength with geometry in view of the current understanding of flashover in vacuum.

Manuscript received September 24, 1987; revised January 27, 1988. This work was supported in part by the National Science Foundation, the Office of Naval Research, the Air Force Office of Scientific Research, and SDIO/STL. C. L. Enloe was supported by AFH-CRD.

The authors are with the Intense Energy Beam Interaction Laboratory, Department of Nuclear Engineering, University of Michigan, Ann Arbor, MI 48106-1204.

IEEE Log Number 8820931.

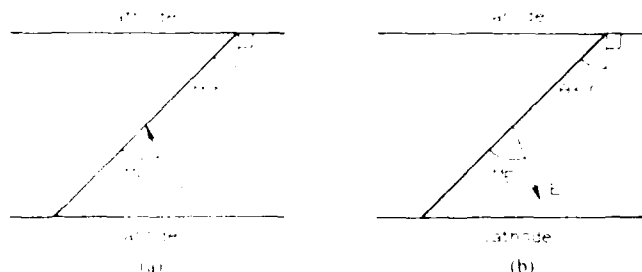


Fig. 1. Sign convention for angled insulators. In the positively angled configuration (a), electrons are accelerated away from the insulator surface, while the reverse is true for the negatively angled configuration (b).

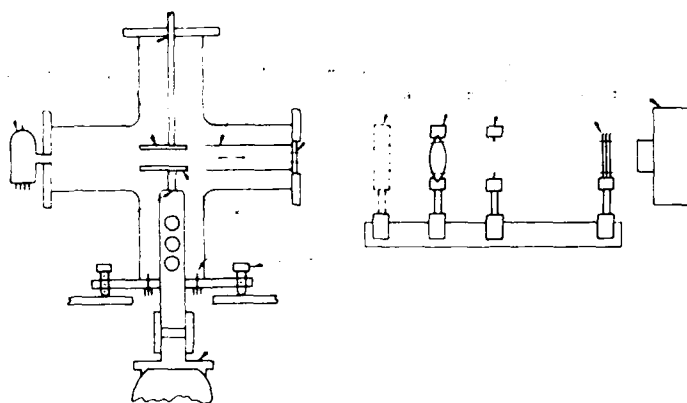


Fig. 2. Experimental configuration. (a) Calorimeter. (b) Quartz lens. (c) Plastic attenuators. (d) Excimer laser. (e) Quartz window. (f) Optional collimator. (g) Top electrode. (h) Ionization gauge. (i) Slip seal. (j) Screw thread adjustment. (k) Bottom electrode. (l) Vacuum feedthrough. (m) Adjustable feet. (n) Turbomolecular pump. (o) Carbon aperture.

II. EXPERIMENTAL CONFIGURATION

The present configuration of the experiment has been described in detail elsewhere [21], and is illustrated in Fig. 2. The apparatus consists of an illumination source (a rare gas excimer laser and associated optics), a test chamber, and various diagnostics. For data presented here, the laser is operated with KrF (248 nm), delivering a maximum of 1.0 J over 60 ns with a 24-ns FWHM. The pulse shape is the same for all shots; however, the beam was typically attenuated by passing it through several thicknesses of absorbing film. The laser produces a uniform rectangular beam which is imaged onto the surface of the insulator sample under test, so that the surface is uniformly illuminated from the anode triple point to the cathode triple point, but without illuminating the electrode surfaces.

A quartz window allows laser light to enter the test chamber. The test chamber is evacuated to $<1.0 \times 10^{-4}$ torr. A turbomolecular pump is employed to minimize backstreaming, since previous results indicated that impurities could significantly alter ultraviolet-induced flashover performance [20]. The insulator sample under test is held between two brass electrodes. The electrodes may be configured as part of a charged particle collector, as shown in Fig. 3(a), to study charged particle emission under ultraviolet illumination in the absence of applied high voltage. Typically, the electrodes are configured as is shown in Fig. 3(b), with a capacitive voltage monitor and a Ro-

gowski coil to monitor voltage and current, respectively, in the interelectrode region. The chamber also allows access parallel to the insulator surface so that the flashover event may be photographed or neutral particle emission monitored. The latter is accomplished through a laser deflection technique which has been described in detail elsewhere [23].

Insulator samples with $\theta = \pm 45^\circ$ have been tested. Materials under test are polyethylene, polystyrene, acrylic (polymethylmethacrylate, specifically Lucite), nylon (specifically nylon-6 or polycaprolactam), acetal (specifically Delrin), teflon (tetrafluoroethylene), and PVC (polyvinylchloride). The chemical formulas for each of these materials are shown in Fig. 4. The first two are simple hydrocarbons, the last two are polymers containing halogens, while the remaining three are more complex polymers containing oxygen and nitrogen. A maximum of 25-kV dc may be applied to the electrodes, which corresponds to 78 kV/cm across a 0.318-cm sample. This is far below the dc flashover electric field at either angle for most materials tested [5]. Nevertheless, flashover is readily induced over all materials when ultraviolet illumination is applied.

III. MICROSCOPIC CHARACTERIZATION

Each insulator material was tested for its response to ultraviolet illumination without applied high voltage. Emission of electrons and neutral particles was quantified

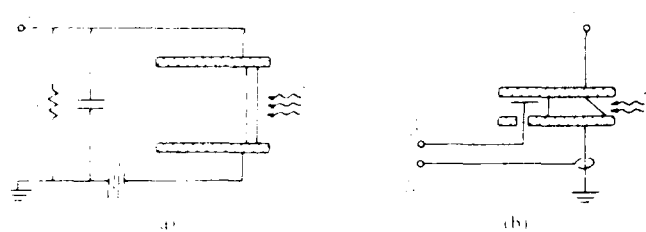


Fig. 3. Electrode configurations: (a) Charged particle collector; (b) Typical configuration with voltage and current monitors.

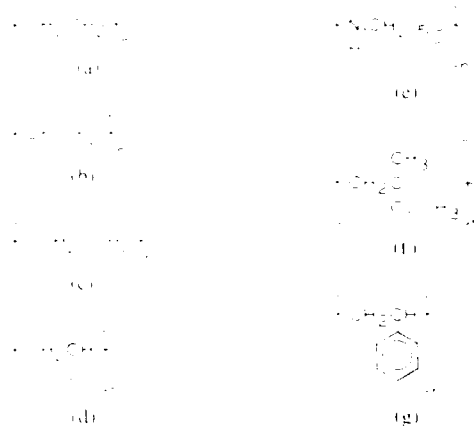


Fig. 4. Chemical formulas of the insulator materials under test: (a) Polyethylene; (b) Teflon; (c) Acetal; (d) PVC; (e) Nylon; (f) Acrylic; (g) Polystyrene [34], [35].

as a function of laser energy or fluence. The behavior of the insulators under ultraviolet illumination presented in this work indicates that fluence or energy is the critical quantity determining flashover initiation.

4. Charged Particle Emission

With the electrodes configured as a charged particle collector, since the RC decay time of the circuit is large compared to the collection time for the electrons, the charge collected, Q , is found from the peak output signal V_p from the simple relation [24]

$$Q = V_p C \quad (1)$$

where C is the capacitance of the circuit, which is readily obtained from the RC decay time of the signal and the circuit resistance R . It is necessary to apply a small electric field to the sample to sweep the electrons into the anode. A field of approximately 50 V/cm is sufficient to accomplish this. (The applied voltage was increased until the charge collected was independent of voltage.)

The charge emitted from the insulator surface during laser illumination as a function of ultraviolet energy deposited is shown in Fig. 5. Photoemission is higher for insulator samples which have not been previously exposed to ultraviolet illumination than for conditioned samples. Exposure to ten pulses of 100-mJ/cm^2 fluence is sufficient to condition each of the materials considered, and all data shown here are for conditioned samples. Photoemission is highly nonlinear in pulse energy; especially, below a certain threshold energy, it is negligible. Pho-

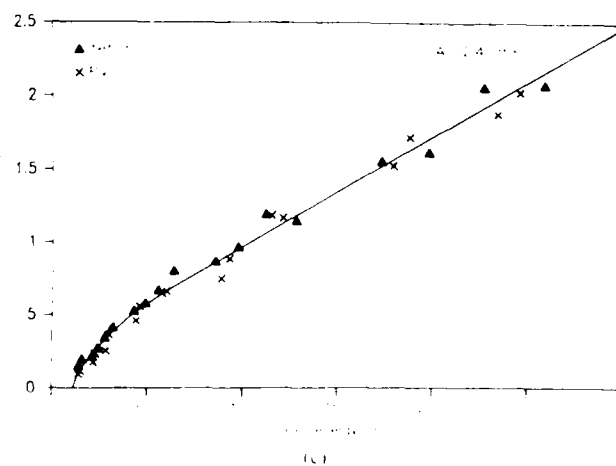
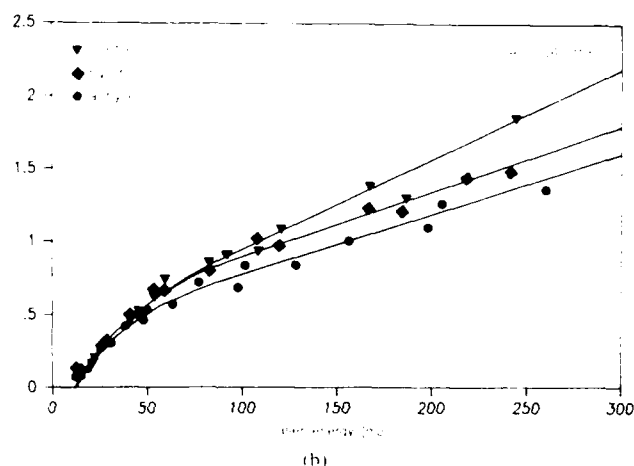
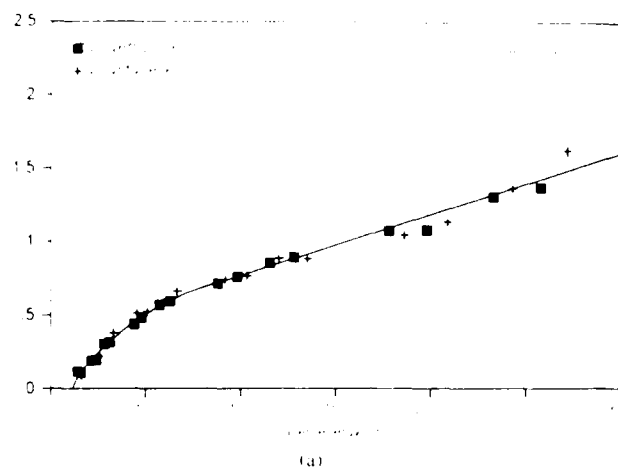


Fig. 5. Charged particle emission from the surface of insulators under ultraviolet illumination in vacuum as a function of illumination pulse energy: (a) Polyethylene and polystyrene; (b) Acrylic, nylon, and acetal; (c) Teflon and PVC.

toemission is lowest for simple hydrocarbons, highest for polymers containing halogens, and somewhere between these bounds for more complex polymers.

The bandgap between the valence band and the vacuum level is, for most polymers, approximately 9 eV . The photon energy at KrF wavelength is 5 eV . Therefore, any photoionization must take place via a multiphoton inter-

action. All of the materials under consideration fluoresce under KrF laser illumination; further, the fluorescence persists for many tens of nanoseconds after the end of the laser pulse. This implies that there are states in the band-gap region which may be excited by the ultraviolet radiation and subsequently ionized [25]. Since the shape of the output fluorescence pulse will be a convolution of the input laser pulse and the exponential decay of the excited states, comparing the input pulse width to the output pulse width yields a lifetime of approximately 13 ns, which is a significant fraction of the input pulse width. Hence, a two-step photoionization event is plausible. Fig. 6 is the result of modeling the two-step ionization process with three coupled rate equations. Three populations are considered: the ground state n_0 , the excited state n^* , and the ionized state n . The equations were solved numerically with all units normalized. The result is similar to the experimental results in that 1) at very low pulse energy, photoionization is negligible, since the probability of a photon's interaction with an excited electron is small, 2) at moderate pulse energy, photoionization increases rapidly as the intermediate state is populated, and 3) at high pulse energy, the increase in ionization with fluence is reduced as the process becomes saturated. Clearly, the results of the simple model do not match the experimental results exactly, but a real polymer is unlikely to be such a simple system. Comparing the major features supports the hypothesis that two-step photoionization is indeed the active process. Photoemission due to three or more photons can be discounted, because lower energy visible light photons do not cause significant fluorescence, which implies that their energy is too low to excite the intermediate states.

B. Neutral Particle Emission

By observing the deflection of a He-Ne probe laser [23], and by making certain assumptions about the profile of the expanding neutrals, the neutral emission from the insulator surface may be determined. One may show that if N particles are emitted from a surface area A with a Maxwellian velocity distribution, then the neutral emission is related to the peak angular deflection of the probing laser beam $\delta\phi_p$ by [23]

$$\frac{N}{A} = \frac{1.08 v_h^2}{K_n D} (\delta\phi_p)^2 \quad (2)$$

where D is the path length of the probe laser through the neutrals, v_h is the distance of the beam away from the surface, and K_n is a constant relating the change in index of refraction to the neutral density: $K_n = 1.03 \times 10^{-23} \text{ cm}^3$ for He-Ne laser light. Since the presence of neutrals is a positive perturbation in the index of refraction, while the presence of electrons is a negative perturbation, it is easily verified from the sign of $\delta\phi$ that the deflection is caused by neutral emission. The average expansion velocity may be found from the time t_p at which the peak

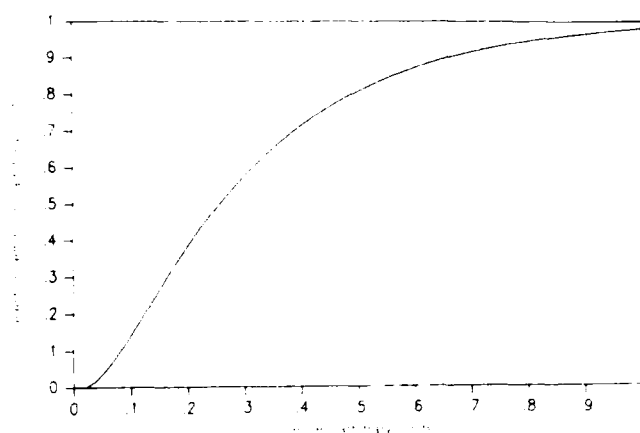


Fig. 6. Results of a simple two-state model of multiphoton ionization in polymers.

deflection occurs [23]:

$$v = \left(\frac{2}{3\pi} \right)^{1/2} \frac{x_h}{t_p} \quad (3)$$

This analysis is valid if $t_p \gg \tau$, the width of the laser pulse. For this experiment, with $x_h = 1 \text{ mm}$, $t_p = 1 \mu\text{s}$, and $\tau = 60 \text{ ns}$, the analysis is indeed applicable.

Neutral emission per unit area of the insulator surface as a function of fluence deposited is shown in Fig. 7. The data are consistent with those found in the literature [26], obtained from measuring the ablation of the insulator surface over many shots. Below a particular threshold fluence which varies with material (on the order of 100 mJ/cm^2), neutral particle emission is negligible. In studying flashover behavior under high voltage, the ultraviolet fluence was typically kept below this threshold value; thus, neutral particle effects do not play a significant role in the results presented, except perhaps a very low field stress ($\sim 10 \text{ kV/cm}$) where the fluences required to initiate flashover are high.

IV. FLASHOVER BEHAVIOR UNDER ULTRAVIOLET ILLUMINATION

A. Observations

To determine the flashover behavior of insulators under ultraviolet illumination, dc high voltage is applied to the electrodes and the insulator surface is illuminated by a single pulse of excimer laser light. The laser beam is imaged onto the insulator so that the laser uniformly illuminates the insulator surface from the anode to the cathode; however, the electrode surfaces themselves are unilluminated. The beam has a cross-sectional area A and a total pulse energy \mathcal{E} . Although the electric field E is not uniform in space, the electric field stress E listed in the data is simply taken as $E = V/L$, where V is the applied voltage and L is the thickness of the insulator sample. Numerical solutions to the Poisson equation which show the potential distribution in the interelectrode region will be presented later in this article.

Current and voltage in the interelectrode region are monitored as the ultraviolet illumination is applied. Typ-

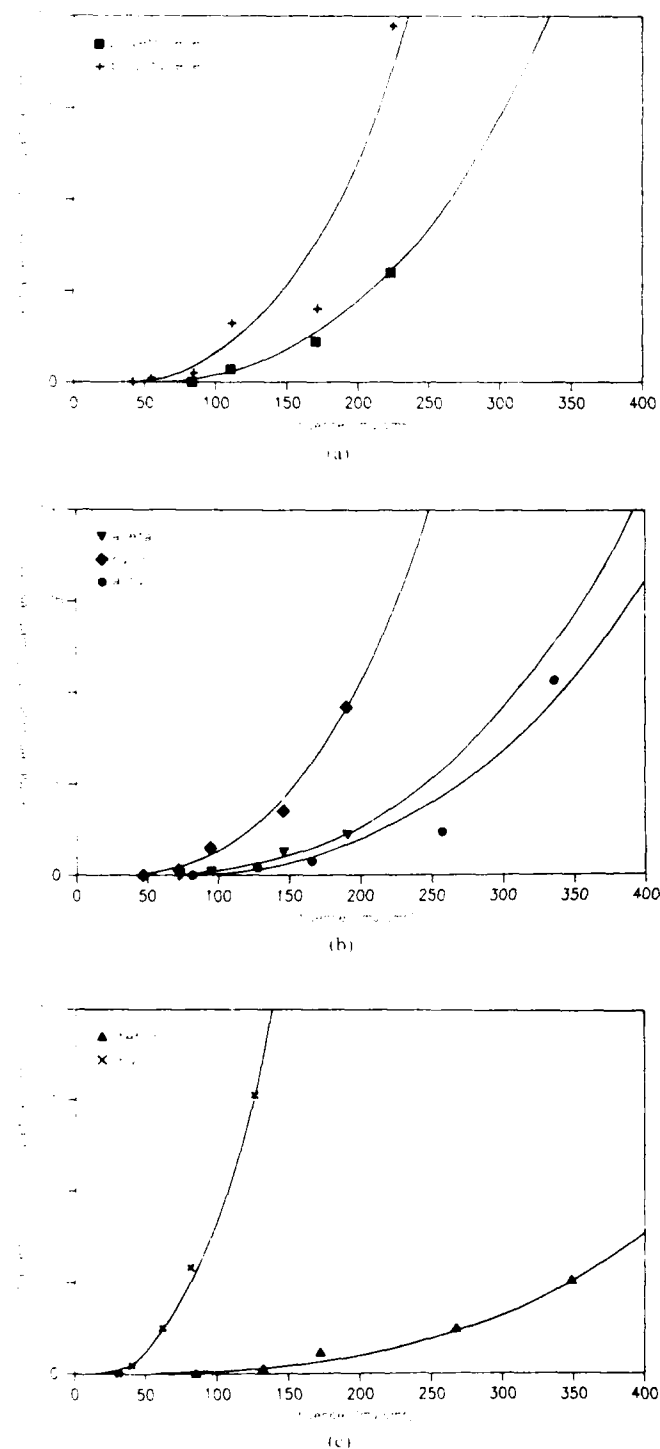


Fig. 7. Neutral particle emission per unit area from the surface of insulators under ultraviolet illumination in vacuum as a function of illumination fluence: (a) Polyethylene and polystyrene; (b) Acrylic, nylon, and acetal; (c) Teflon and PVC.

ical data are shown in Fig. 8. Although significant prebreakdown activity is evident, flashover is identified as the discontinuity in the voltage and current indicating the sudden collapse of the impedance in the gap. With time $t = 0$ taken as the start of the laser pulse, the time t_f at which flashover occurs is noted. In these experiments, the laser beam is attenuated, reducing \mathcal{E} , and again t_f is noted.

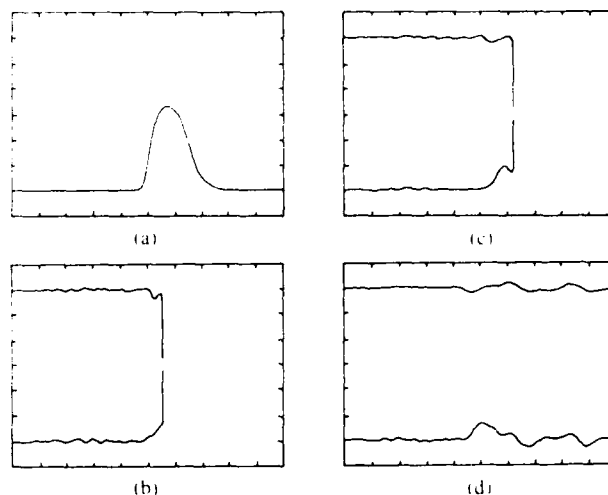


Fig. 8. Sample data, all traces 20 ns/div: (a) Laser pulse; (b)-(d) Voltage (top), 0.35 kV/div; current (bottom), 0.44 A/div; dc charge voltage 12 kV: (b) Strongly induced flashover; (c) Weakly induced flashover; (d) Stable.

As more attenuation is added, t_f increases until flashover is no longer observed ($t_f = \infty$).

The prebreakdown current $i(t)$ is nearly proportional to the illumination intensity $I(t)$, and the flashover event may be roughly characterized according to the prebreakdown current behavior as 1) strongly induced flashover, in which both $I(t)$ and $i(t)$ increase continuously until flashover occurs, 2) weakly induced flashover, in which $I(t)$ and $i(t)$ reach a maximum and are actually decreasing at the time of flashover, or 3) stable, in which no flashover is observed, even though $i(t)$ is not zero during the illumination pulse.

There is no correlation of the time of the flashover event with either the instantaneous value of the illumination intensity or the prebreakdown current. Depending on the pulse energy \mathcal{E} , flashover is observed with equal regularity on the rising as well as the falling edge of the illumination pulse, even late in time when the illumination is significantly less than its peak value. Flashover occurring after the illumination ceases entirely, however ($t_f > \tau$), is rare, observed in fewer than 1 percent of the flashover events. This simple observation leads to the conclusion that it is ultraviolet fluence, rather than power density, which governs the initiation of flashover. If there were a critical power density required to initiate flashover, then that power density would be achieved, if at all, on the rising edge of the illumination pulse first, and flashover would be observed on the rising edge of the pulse, or not at all. Since flashover is indeed observed even late on the falling edge of the pulse, fluence, rather than power density, must be the determining quantity.

B. Analysis

The normalized pulse shape $f(t)$ of the ultraviolet illumination and its integral, which are the same for all shots, are shown in Fig. 9. The normalization is that

$$\int_0^{\infty} f(t) dt = 1. \quad (4)$$

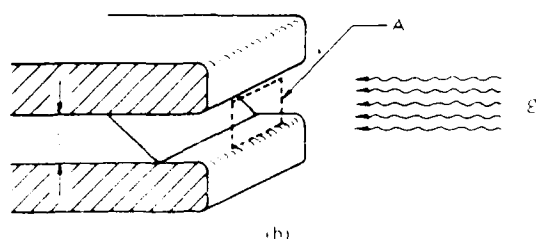
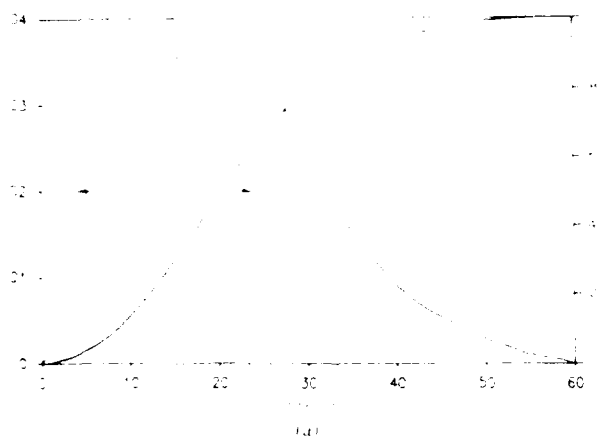


Fig. 9. (a) Normalized power and energy of the illuminating pulse. (b) Illuminated area of the insulator surface.

Thus, for any time t , the instantaneous illumination intensity $I(t)$ can be expressed in terms of the pulse energy \mathcal{E} and the cross-sectional area A of the beam, and is defined to be

$$I(t) = \frac{\mathcal{E}f(t)}{A} \quad (5)$$

while the fluence deposited at time t , $F(t)$, is

$$F(t) = \int_0^t I(t') dt'. \quad (6)$$

From (4), it follows that the total fluence is simply $F(\tau) = \mathcal{E}/A$. However, it is clear that any ultraviolet illumination of the surface *after* flashover occurs can have no effect on the process of flashover *initiation*. Therefore, it is the fluence deposited at the time of flashover $F(t_f)$ which is appropriate to consider in investigating the initiation process.

The results shown in Fig. 10 are typical of the phenomenon of induced insulator flashover. As the total fluence $F(\tau)$ (or equivalently, the pulse energy \mathcal{E}) decreases, the time to flash t_f increases, as shown in Fig. 10. However, it appears that there is a critical value of the fluence F_c which governs the initiation of flashover by ultraviolet illumination, irrespective of the illumination intensity. Specifically, if the total fluence $F(\tau) < F_c$, then flashover is not induced although some current may be observed in the interelectrode region. If $F(\tau) > F_c$, then flashover is induced at a time t_f such that $F(t_f) = F_c$. This is illustrated in Fig. 10, which shows that as the total fluence $F(\tau)$ is changed by nearly a factor of 10 by changing the

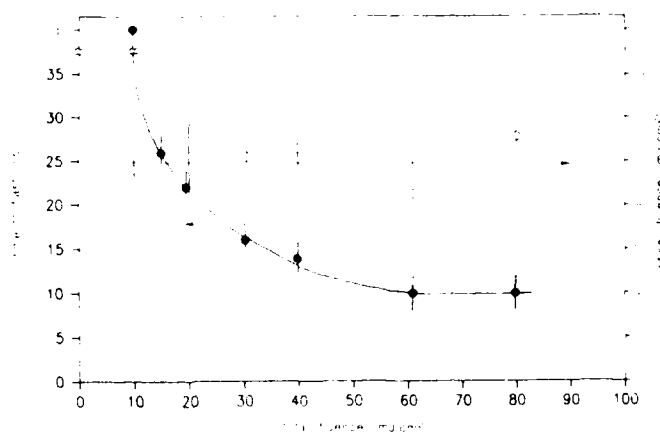


Fig. 10. Flashover behavior of a single material (polyethylene, conventional configuration) at constant electric field stress ($E = 50$ kV/cm). Solid line: time to flash as a function of total fluence (pulse energy divided by illuminated area). Broken line: critical fluence (fluence at the time of flashover) as a function of total fluence. The critical fluence is nearly constant, although the total fluence varies.

pulse energy \mathcal{E} , the critical fluence at which flashover occurs remains essentially constant.

The critical fluence is, however, a strong function of the insulator geometry and the electric field stress. Insulator samples were tested over a range of electric field stress from 10 to 80 kV/cm in both conventional and unconventional configurations. The critical fluence is displayed in Fig. 11 as a function of electric field stress for each of the insulator materials tested in both conventional and unconventional configurations. Several trends are evident: 1) the critical fluence decreases with increasing electric field stress for $E < 40$ kV/cm, 2) the critical fluence is approximately constant for $E > 40$ kV/cm, and 3) the unconventional configuration is more tolerant to ultraviolet fluence by nearly a factor of 2 in fluence, except for some materials at very low field stress and correspondingly high fluence.

C. Correlations

The critical fluence at high electric field stress (the constant portion of each of the curves in Fig. 11) displays various degrees of correlation to the macroscopic and microscopic properties of the insulating materials. Neutral particle emission characteristics can be eliminated as a cause of ultraviolet-induced insulator flashover at high field stress, since the fluence involved is too low to produce significant neutral emission. Neutral emission may be a cause of the crossover in some of the curves in Fig. 11 at high fluence.

The critical fluence is only weakly correlated to the electron photoemission shown in Fig. 5, although to a slight degree the more readily a material emits photoelectrons, the less tolerant it is to ultraviolet radiation. The critical fluence shows a much greater correlation to secondary electron emission, as in Fig. 12. The secondary electron emission coefficient K is that adopted by Burke [27], who found that for many polymers the secondary

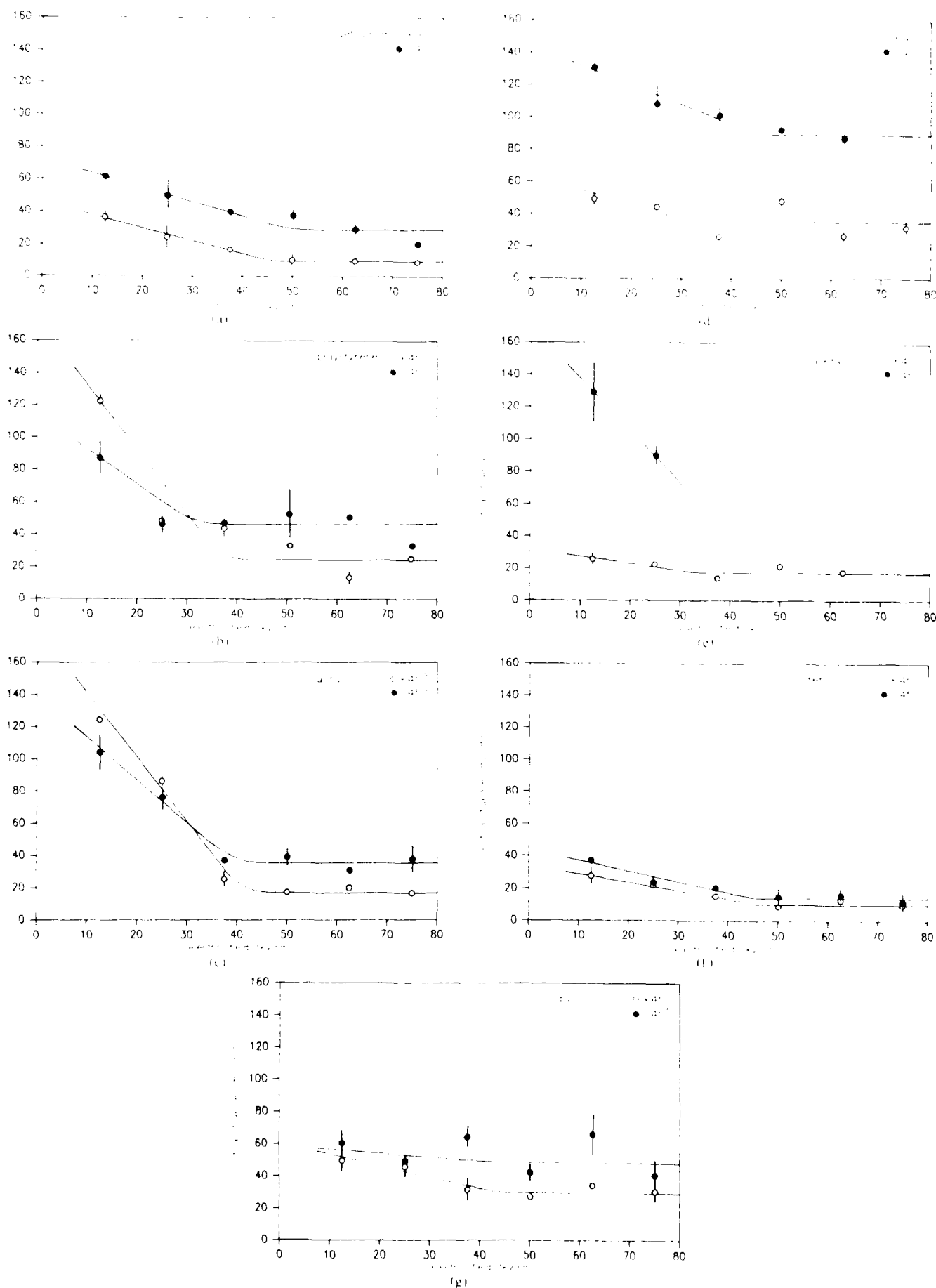


Fig. 11. Critical fluence required to initiate flashover as a function of electric field stress and insulating material: (a) Polyethylene, (b) Polystyrene, (c) Acrylic, (d) Nylon, (e) Acetal, (f) Teflon, (g) PVC.

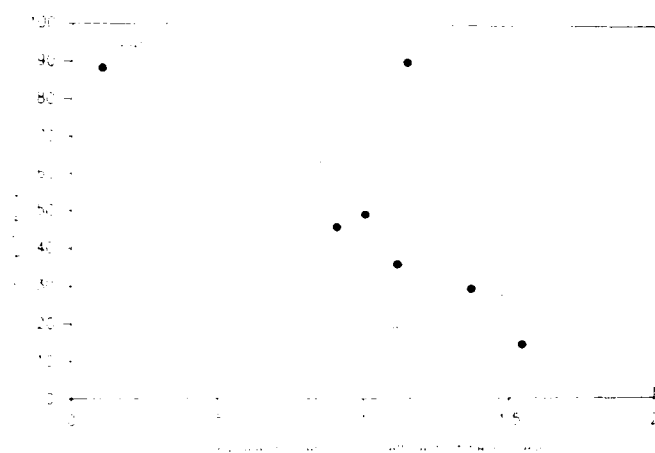


Fig. 12. Critical fluence ($E_0 = 40$ kV/cm) versus secondary electron emission coefficient for all materials tested. Broken line: positive angle (conventional) configuration. Solid line: negative angle (unconventional) configuration.

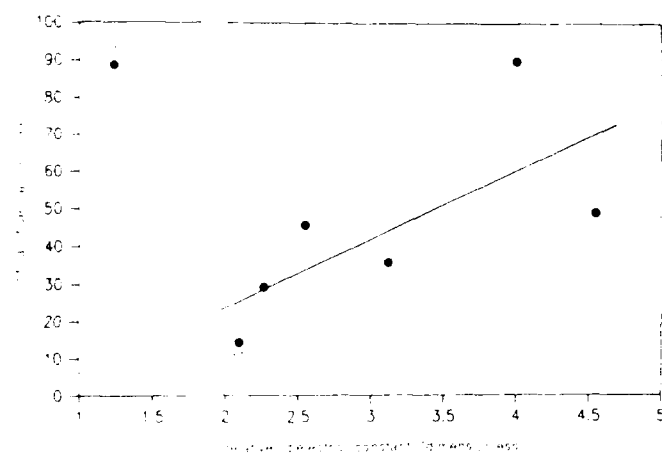


Fig. 13. Critical fluence ($E_0 = 40$ kV/cm) versus relative dielectric constant for all materials tested. Broken line: positive angle (conventional) configuration. Solid line: negative angle (unconventional) configuration.

TABLE I
SUMMARY OF DIELECTRIC MATERIAL PROPERTIES

Material	Relative dielectric constant	Secondary electron emission coefficient	Critical fluence, $\theta = +45^\circ$	Critical fluence, $\theta = -45^\circ$
	[kV/cm]	[27]	(J/cm ²)	(J/cm ²)
polyethylene	2.25	1.1	49.3	29.3
polytetrafluoroethylene	2.1	1.087	45.7	21.7
quartz	4.5	1.115	38.8	17.8
glass	4.0	1.148	39.9	35.5
ceramic	6.7	1.116*	19.6	13.6
epoxy	3.5	1.1546	14.4	11.6
oil	2.2	1.16**	49.1	3.2

* Calculated from Brinkley's formula [17].

** Assumed to be Brinkley's data [17].

Again, the more readily a material emits secondary electrons, the less tolerant it is to ultraviolet radiation. The critical fluence also shows a positive correlation to the dielectric constant of the material, as in Fig. 13. The greater the dielectric constant, the more tolerant the material is to ultraviolet radiation. The properties of each of the insulating materials are summarized in Table I.

V. THEORY OF ULTRAVIOLET-INDUCED INSULATOR FLASHOVER

The observations and analysis of the phenomenon of ultraviolet-induced insulator flashover point to a particular mechanism of flashover initiation. To summarize the results, ultraviolet-induced flashover depends neither on the instantaneous value of the intensity of the ultraviolet illumination nor on the prebreakdown current, but rather on the time-integrated ultraviolet fluence on the insulator surface. The critical fluence required to initiate flashover is a function of the insulator material, and is less in the positive-angle (conventional) configuration than in the negative-angle (unconventional) configuration by approximately a factor of 2. The critical fluence increases with increasing dielectric constant and decreases with increasing secondary (and to a slight degree, primary) electron emission.

The evidence indicates that the effect of the ultraviolet illumination is to prepare the dielectric/vacuum interface by causing a buildup of surface charge, making it more susceptible to flashover than the unilluminated, uncharged state. The flashover event itself is quite distinct from the prebreakdown phenomenon; the time scale of the former is on the order of 1 ns, while the time scale of the latter is tens of nanoseconds. If this disparity were due entirely to some formative time lag, then one would expect to regularly see flashover occurring a significant time after the end of the illumination pulse. In fact, such events are rare. Also consistent with this inference is the observation that fluence, independent of illumination intensity, is the quantity which determines flashover behavior.

The geometry-dependent behavior of the flashover strength of vacuum insulators without ultraviolet illumination has been well established by Watson [3] and Milton [5], among others. Their results are familiar and have formed the basis for most high-voltage vacuum insulator designs in practical systems. Their results show that flashover strength is maximum near $\theta = \pm 45^\circ$ and minimum near $\theta = 0^\circ$, and that in general the local maximum at positive angle is greater than that at negative angle. More recently, Brainard [28] has analyzed Milton and Watson's data, and has determined that surface charging plays a significant role in the flashover process for $-30^\circ < \theta < 0^\circ$, but is negligible for $\theta = \pm 45^\circ$.

The theory of surface charging of vacuum insulators via secondary electron emission is similarly well-developed [29]-[31]. For any material, the secondary electron emission coefficient δ is a function of the incident electron energy E_0 . If the local electric field is such that an electron which is emitted from the surface returns with an energy such that $\delta(E_0) > 1$, the surface charges positively. On

electron yield δ follows a universal curve and scales as

$$\delta(E_0) = KE_0^{-0.735} \quad (7)$$

where E_0 is the impact energy of the primary electron,

the other hand, if $\delta(E) < 1$, a stable situation results: the surface neither gains nor loses charge. The local electric field is a superposition of the applied electric field (which itself is modified by the polarization charge in the dielectric) and the field due to the surface charge on the insulator. The stability condition is equivalent to the requirement that the local electric field be inclined at some critical angle θ_c which varies with material. For many insulating materials, $\theta_c \approx -30^\circ$ [28], where the negative sign indicates that the electrons return to the insulator surface. If, neglecting surface charge, the electric field angle θ_f is greater than θ_c (as in the conventional configuration), then the stable surface charge distribution is positive; otherwise (as in the unconventional configuration) the stable surface charge density is negative [30]. By a numerical solution to the Poisson equation (in this case, using the charge simulation technique [32]), it is straightforward to show that for an uncharged interface, the electric field is enhanced near the narrow end of the insulator, while if a sufficient surface charge is present, the electric field is enhanced near the wide (or pointed) end of the insulator. This effect is illustrated in Fig. 14 for the case in which $\theta_f = \theta_c$ everywhere on the insulator surface. The situation is not entirely symmetrical; with surface charge present, the field enhancement near the wide end is much greater for the conventional than for the unconventional configuration. This is readily explained, since in the unconventional configuration, neglecting surface charge, the uncharged electric field angle is much nearer the critical angle.

If, however, surface charging is to occur via secondary electron emission, there must be a source of primary electrons. For $\theta \approx 0^\circ$, the cathode triple point is a ready source of primary electrons. As Fig. 15(a) and (c) shows, however, the cathode triple point is a poor source of primary electrons for large values of θ . For $\theta = +45^\circ$, electrons miss the insulator surface entirely. For $\theta = -45^\circ$, since $\delta < 1$ over the insulator surface and the path length along the insulator of the electron trajectories is small (a few microns) [30], charging cannot propagate from the cathode triple point. It is not surprising, then, that insulators at large angles, whether positive or negative, do not charge under an applied electric field alone [28]. Ultraviolet illumination, however, provides a source of electrons which is distributed over the insulator surface, as in Fig. 15(b) and (d). Therefore, it is possible for the electric field configuration in the interelectrode region to be significantly modified under ultraviolet illumination, due to charging of the insulator surface.

The magnitude of the surface charge required to significantly affect the interelectrode electric field varies with the dielectric constant of the insulating material. Fig. 16 shows the dependence of the electric field angle θ_f on the surface charge density for insulators of two dielectric constants, as determined from a numerical solution to the Poisson equation (in this case, using the code LAPLACE [29]). The results presented are for uniform positive surface charge on a positively angled insulator; the results are analogous for negative surface charge on a negatively

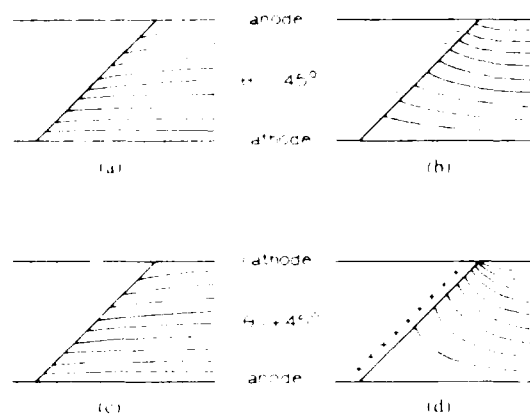


Fig. 14. Equipotential contours of (a), (c) uncharged and (b), (d) charged insulators in vacuum, for $\epsilon_r = 2.0$ and $\theta_c = 30^\circ$.

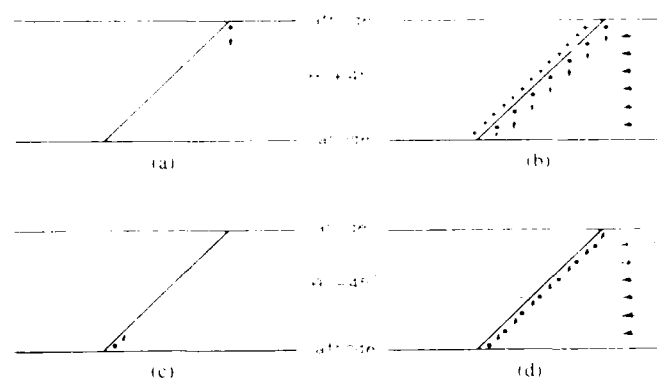


Fig. 15. Surface charging for insulators at $\pm 45^\circ$ is unlikely (a), (c) unless a source of primary electrons other than emission from the triple point is available (b), (d).

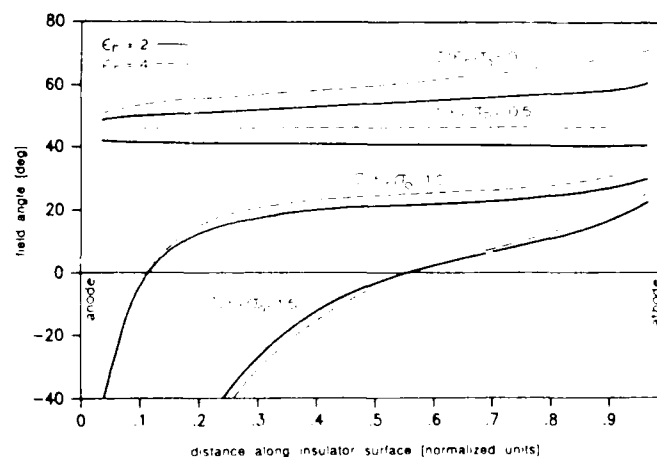


Fig. 16. Angle θ_f between the electric field and the insulator surface as a function of position on the surface and surface charge density. Solid line $\epsilon_r = 2$. Broken line $\epsilon_r = 4$.

angled insulator with the sign of θ_f reversed. The surface charge density is given in units of the charge density on the vacuum electrodes. Treating the vacuum electrodes as a capacitance, the surface charge Q on an area A of the electrode surface is just $Q = CV$, where C is the capacitance of the parallel-plate electrodes and V is the applied voltage. Now, $C = \epsilon_0 A/L$, where L is the interelectrode distance. The surface charge density on the vacuum electrodes is then $\sigma_0 = CV/A = \epsilon_0 E$ since $E = V/L$. From

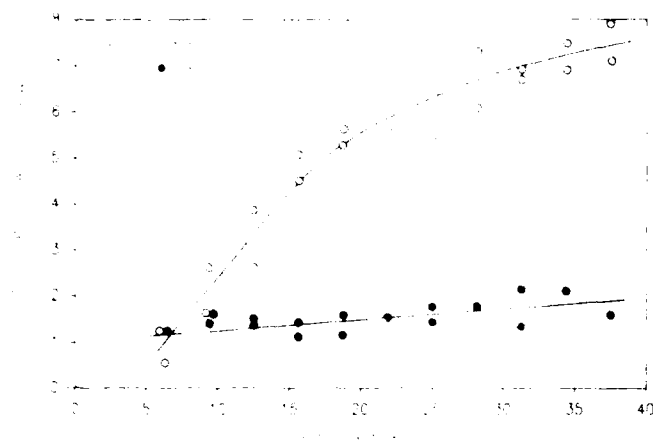


Fig. 17. Prebreakdown current per unit illumination intensity as a function of electric field stress.

Fig. 16, the surface charge density required to modify the electric field so that $\theta_f \approx 0^\circ$ is proportional to the dielectric constant of the material, and is on the order of

$$\sigma'_{m, \theta=0} = \epsilon_r \sigma_0 \quad (8)$$

The magnitude of surface charging of insulators prior to flashover may be estimated from prebreakdown current measurements. For the polymers under consideration, $2 < \epsilon_r < 5$. For $E = 50 \text{ kV/cm}$, $\sigma_0 \approx 4.4 \text{ nC/cm}^2$. Prebreakdown currents observed are on the order of 0.5 A for 60 ns , so that the charge transferred in the interelectrode gap is on the order of 30 nC . The illuminated surface area of the insulator is approximately 1.5 cm^2 , which corresponds to $\sigma = 20 \text{ nC/cm}^2$. Therefore, the condition implied by (8) is readily satisfied under ultraviolet illumination.

The induced surface charging theory of ultraviolet-induced insulator flashover in vacuum is consistent with the observation that fluence is the critical quantity in determining when flashover occurs. Since the surface charge density required to modify the interelectrode field is proportional to ϵ_r , it explains the dependence of F_c on ϵ_r . Since charging proceeds by secondary electron emission, it explains the dependence of F_c on K . The explanation of the fact that the unconventional configuration is more tolerant than the conventional is twofold. As Brainard has shown [28], if the insulator surface is charged, it is the conventional configuration which is the weaker of the two configurations. Also, since initially $\delta < 1$ for $\theta = -45^\circ$ and effectively $\delta = 1$ for $\theta = +45^\circ$ (all charges are removed from the insulator surface), the conventional configuration should be more readily charged than the unconventional. This is borne out by the results shown in Fig. 17, which indicate that for the same illumination, the prebreakdown current is greater for the conventional than for the unconventional configuration. Field enhancement at the wide end of the insulator, as is the case for a charged insulator surface, is also consistent with indications of explosive emission at that point from open shutter photographs of the induced flashover process [20].

VI. CONCLUSIONS

Ultraviolet-induced flashover over polymeric insulators in vacuum depends on the ultraviolet fluence incident on the insulator surface. The negative-angle (unconventional) configuration is superior in ultraviolet tolerance to the positive-angle (conventional) configuration by approximately a factor of 2 in fluence. Insulating materials with high dielectric constants and low secondary electron emission coefficients exhibit superior ultraviolet tolerance. A model of ultraviolet-induced insulator flashover based on induced charging of the insulator surface is sufficient to explain the observed phenomena. The ultraviolet fluences required to initiate flashover are sufficiently low that the contribution of neutral particle emission to the initiation of flashover may be disregarded, except perhaps at very low field stress ($\sim 10 \text{ kV/cm}$) where the critical fluences required to initiate flashover are correspondingly higher.

It is important to note that this work was conducted using a monochromatic ultraviolet source. Previous studies by one of the authors using a broad-band ultraviolet source [18], [19] found critical fluences which were much smaller than those reported here. In those experiments, however, there was a significant component of ultraviolet illumination at wavelengths shorter than the 248-nm KrF laser line. At these short wavelengths, the penetration depth of ultraviolet light in the materials is a strong function of wavelength and decreases sharply as wavelength decreases. Therefore, shorter wavelength ultraviolet should have a correspondingly larger effect on surface phenomena, and thus induce flashover more readily. The previous measurements are therefore consistent with the data presented here.

REFERENCES

- [1] P. H. Gleichauf, "Electrical breakdown over insulators in high vacuum," *J. Appl. Phys.*, vol. 22, no. 6, pp. 766-771, June 1951.
- [2] E. S. Borovik and B. P. Batrakov, "Investigation of breakdown in vacuum," *Sov. Phys. Tech. Phys.*, vol. 3, no. 9, pp. 1811-1817, Sept. 1958.
- [3] A. Watson, "Pulsed flashover of insulators in vacuum," *J. Appl. Phys.*, vol. 38, no. 5, pp. 2019-2023, Apr. 1967.
- [4] R. Hawley, "Solid insulators in vacuum: A review," *Vacuum*, vol. 18, no. 7, pp. 383-390, Nov. 1968.
- [5] O. Milton, "Pulsed flashover of insulators in vacuum," *IEEE Trans. Elec. Insul.*, vol. EI-7, no. 1, pp. 9-15, Mar. 1972.
- [6] A. A. Avdienko, "Surface breakdown of solid dielectrics in vacuum. I. Characteristics for breakdown of insulators along the vacuum surface," *Sov. Phys. Tech. Phys.*, vol. 22, no. 8, pp. 982-985, Aug. 1977.
- [7] R. V. Latham, *High Voltage Vacuum Insulation*. London: Academic, 1981.
- [8] H. C. Miller, "Improving the voltage holdoff performance of alumina insulators in vacuum through quasimetallizing," *IEEE Trans. Elec. Insul.*, vol. EI-15, no. 5, pp. 419-428, Oct. 1980.
- [9] G. L. Jackson et al., "Pulse flashover of solid dielectrics in vacuum," *IEEE Trans. Elec. Insul.*, vol. EI-18, no. 3, pp. 310-314, June 1983.
- [10] H. C. Miller, "The effect of doping in the voltage holdoff performance of alumina insulators in vacuum," *IEEE Trans. Elec. Insul.*, vol. EI-20, no. 3, pp. 505-509, June 1985.
- [11] L. L. Hatfield et al., "A treatment which inhibits surface flashover in vacuum," in *Proc. XIIIth Int. Symp. Discharge and Electrical Insulation in Vacuum*, vol. 1 (Shoreham, Israel), Sept. 1986, pp. 79-83.
- [12] S. Grzybowski, E. Kuffel, and J. P. C. McMath, "The flashover volt-

- [illegible]

Ultraviolet-Induced Flashover of a Plastic Insulator Using a Pulsed Excimer Laser

C. L. Enloe¹ and R. M. Gilgenbach¹

Received July 10, 1986; revised September 11, 1986

Ultraviolet-induced flashover has been observed over stressed, angled, acrylic insulators illuminated by a short (60 ns) pulse of excimer laser light at 249 nm. Flashover has been observed at ultraviolet fluences of $5\text{--}65\text{ mJ/cm}^2$ for electric field stresses approximately 10–30% of static breakdown stress. Insulators at positive angle (conventional configuration) exhibit a reduced tolerance to ultraviolet light versus insulators at negative angle (unconventional configuration) by approximately a factor of 2, while the presence of impurities at the triple point reduces the tolerance to ultraviolet even further. Flashover is related to the fluence, rather than the power density, for short pulses, and the production of photoelectrons is a likely mechanism for the initiation of flashover.

KEY WORDS: Insulator flashover, ultraviolet, surface plasma

1. INTRODUCTION

It has long been known that the interface of a solid dielectric insulator with vacuum is one of the weak points of a high-voltage transmission system, because an insulator in vacuum is subject to flashover at high electric field stress. Researchers in the field of high-energy-density plasmas have found that intense ultraviolet radiation can initiate the flashover process at the dielectric/vacuum interface.^{1,2} Subsequent bench tests have shown that the phenomenon exists even at relatively low field stress (approximately 10% of self-breakdown stress).^{3,4} While ultraviolet-induced insulator flashover is a bane to designers of pulsed-power systems, it may well be a boon in the development of low-inductance, high-current, triggerable surface-tracking switches,^{5,6} large-area flashboards for ion diodes, in plasma processing applications where it is desirable to create a large-area uniform surface discharge plasma in a controlled manner, or as new xuv light sources. With the recent development of multi-microsecond electron beam

¹ Intense Energy Beam Interaction Laboratory, Department of Nuclear Engineering, University of Michigan, Ann Arbor, Michigan 48109

accelerators such as the Michigan Electron Long-Beam Accelerator^{7,8} (MELBA) there exists increased concern about the performance of the insulator stacks which may be subjected to intense ultraviolet radiation.

One drawback with previous ultraviolet-induced flashover experiments was that, although it was apparent that the moderate to hard portion of the ultraviolet spectrum ($h\nu \approx 4\text{ eV}$) was responsible for initiating flashover, it was unclear exactly what the characteristics of the illumination were in this region. Pinched plasma devices were previously used as illumination sources; consequently the illumination was broadband and irregular in time, usually appearing in several discrete pulses of many microseconds duration. The difficulties associated with interpreting such data have been eliminated in this experiment by using an ultraviolet excimer laser as the illumination source. The illumination is monochromatic and is applied in a single, near-gaussian pulse. The laser has the added advantage that the portion of the insulator which is illuminated can be closely controlled.

2. EXPERIMENTAL APPARATUS

The experimental apparatus is illustrated in Fig. 1. It consists of an illumination source and its associated optics, a test chamber in which a sample insulator is placed, and a high-voltage supply with a voltage monitor.

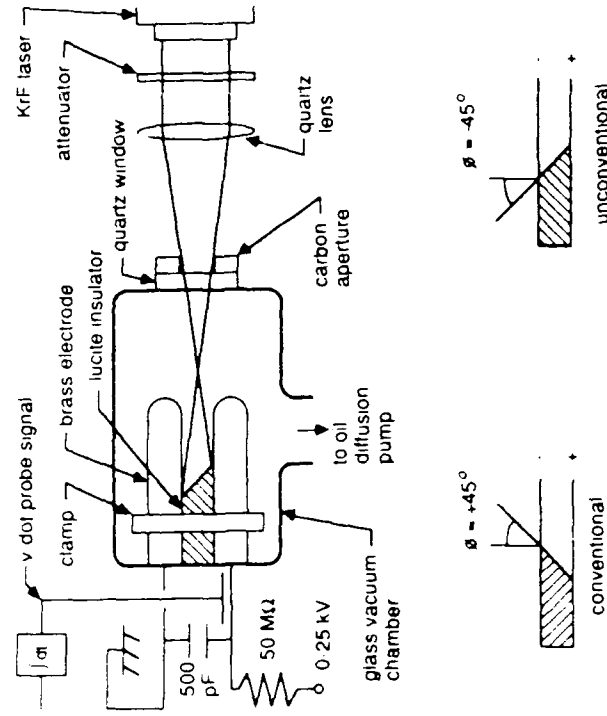


Fig. 1. Experimental apparatus for investigating ultraviolet-induced insulator flashover.

Ultraviolet illumination was provided by a krypton fluoride excimer laser (Lumonics TE-202) at 249 nm ($h\nu = 5$ eV). The laser emits a uniform rectangular beam, approximately 2.5 cm high \times 3.0 cm wide at the laser aperture. The beam was imaged using a simple planoconvex quartz lens onto a 1.1-cm² profile at the insulator surface. Thus the entire output of the laser was used to illuminate a small portion of the insulator surface including the anode and cathode triple points, while the electrodes remained unilluminated except for a small area at the triple point itself which was in the falling edge of laser illumination. A carbon aperture was used to eliminate stray light on the electrodes, and this aperture could be varied to further restrict illumination of the insulator surface.

The temporal pulse shape of the laser was measured by an ultraviolet-sensitive PIN diode and is shown in Fig. 2. The pulse has a full width at half maximum of 27 ± 2 ns and a full width at the base of 58 ± 2 ns where the small variation is indicative both of shot-to-shot differences and differences between various fills of the lasing gas mixture. A large-area calorimeter was used to monitor the total laser energy. From the pulse shape and the energy deposited, the peak intensity could be calculated. The beam was attenuated using filters made of thin sheets of polyethylene stretched on a metal frame.

A quartz window admitted the laser light to a Pyrex vacuum chamber evacuated to typically 5.6×10^{-5} Torr by a 2-inch oil diffusion pump. The insulator sample was made of 0.63 cm acrylic stock approximately 10 cm wide. This material was chosen because it is the material used on MELBA and many other similar devices. The exposed surface was angled at 45°

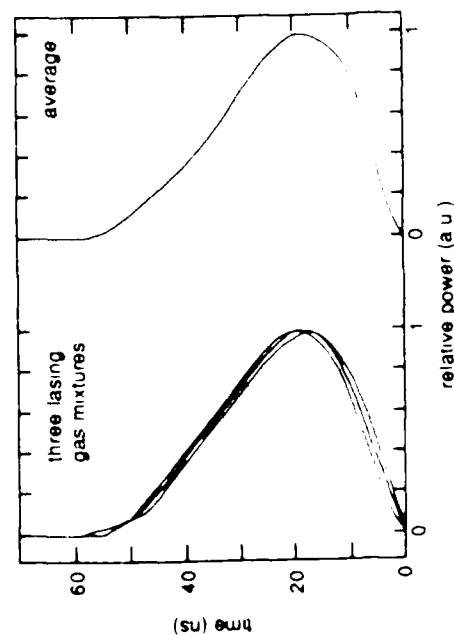


Fig. 2. Laser pulse shape

according to typical practice^{18,19} and was smoothed with 600-grit carbide paper. Data are presented with the insulator installed in both a positive angle (conventional) and a negative angle (unconventional) configuration, as indicated in Fig. 1. The insulator was held between two brass electrodes, which extended forward well beyond the insulator surface to eliminate irregularities due to fringing fields in the gap. An insulating clamp was placed around the electrodes to ensure that good contact was made between the electrodes and the insulator.

High D.C. voltage was applied between the electrodes while the voltage was monitored with a passively integrated V-dot probe in an oil tank external to the vacuum chamber. Voltage was maintained with a small (500 pF) capacitor isolated from the power supply by a large (50 M Ω) resistor. A maximum voltage $V = 25$ kV could be obtained, for a maximum electric field in the gap of $E = 39.3$ kV/cm. The flashover strength of acrylic reported in the literature is approximately 200 kV/cm for both configurations¹⁸; the insulator was far from static breakdown. Nevertheless, flashover was observed under ultraviolet illumination. Because the energy in the capacitor was small, the flashover produced no noticeable damage to the insulator surface, and many shots could be taken before cleaning or replacing the insulator sample. Timing between the laser PIN diode signal and the voltage probe was carefully measured to allow timing resolution to within ± 2 ns.

Open-shutter photography was used, viewing along the edge of the insulator to obtain a profile of the discharge, or viewing obliquely to determine the portion of the insulator over which flashover occurred.

3. EXPERIMENTAL PROCEDURE

In a typical shot series, the insulator sample and the electrodes were cleaned with methanol, the insulator was clamped in place, and the system was evacuated. The initial energy in the unattenuated laser pulse was measured. High voltage was applied, the laser was pulsed to illuminate the insulator, and the voltage probe indicated flashover by a collapse of voltage across the electrodes. The time at which flashover occurred was measured. Attenuation was added to reduce the laser intensity on the insulator surface and another shot was taken. As the laser intensity was decreased, flashover occurred later in time. Further attenuation was added and shots were taken until the voltage probe indicated that flashover was no longer induced. At this point, the voltage was varied and the procedure repeated. Voltage was varied randomly to avoid any conditioning effects or systematic errors. After approximately 20 shots the insulator was removed, examined, and cleaned.

Care was taken to ensure that the laser illumination was well characterized. The laser energy tended to decrease monotonically after a large number of shots since the fluorine in the lasing mix reacted with the electrodes in the lasing chamber. By monitoring the laser energy frequently between shots on the insulator, the energy in the unattenuated beam could be predicted at any time. Periodically, burn patterns were taken on developed, unexposed Polaroid film. When the illumination began to appear uneven (after approximately 50 shots) the lasing gas mixture was replaced so that the effect of hot spots in the laser illumination was avoided.

4. EXPERIMENTAL DATA AND ANALYSIS

Data from a single shot is shown in Fig. 3. We identify several times from this figure. We take the time $t = 0$ to be the start of the laser pulse. The laser intensity peaks at t_p , where $t_p = 20 \pm 2$ ns. We take the time at which flashover occurs, t_f , to be the beginning of the rapid (≤ 2 ns) collapse of voltage across the electrodes. For the data presented in this paper $10 \text{ ns} < t_f < 70 \text{ ns}$. In some data, there is a prebreakdown voltage droop, indicative of a small prebreakdown current in the gap. We define the width of this droop as w . For these data $0 \leq w \leq 8 \text{ ns}$. The width w tended to zero at high electric fields.

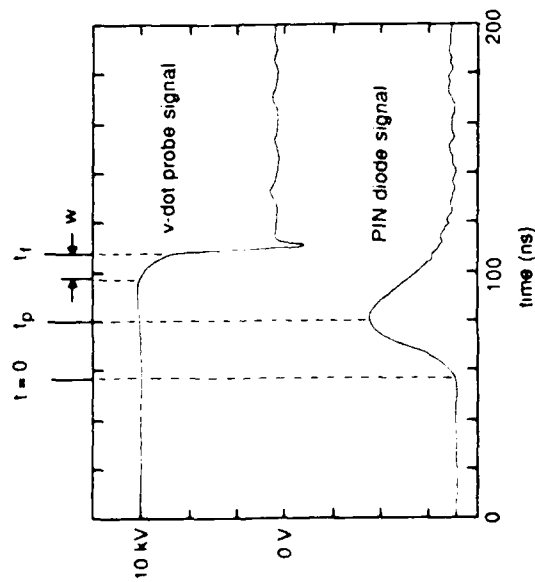


Fig. 3. Sample data: voltage across the electrodes (top) and laser illumination (bottom) versus time.

The laser pulse shape is constant for all data, so that we need only to know the peak intensity I_{\max} to characterize the intensity $I(t)$ for the entire pulse. Clearly, laser light which illuminates the gap after flashover occurs has no role in the process that initiates flashover. (After a low-impedance path is created, the dynamics of the plasma in the gap will be dominated by the external circuit.) Therefore, we may define the fluence F as

$$F = \int_0^{t_f} I(t) dt$$

One basic question which needs to be addressed is whether ultraviolet-induced insulator flashover is dependent upon ultraviolet intensity (W/cm^2) or total fluence (J/cm^2) at the time of flashover. Therefore we present the data as time to flash versus peak intensity (a) and fluence (b) for several values of the electric field E in Figs. 4-8. The time to flash is dependent on the details of $I(t)$ and is specific to this illumination source. However, as the intensity is varied by a factor of 2-6 for the various configurations, the fluence at the time of flashover is nearly constant. Further, the mere fact that the flashover is observed much later than the peak of $I(t)$ argues that ultraviolet-induced flashover is a function of fluence. If flashover were initiated at a particular critical intensity, that intensity would always be attained, if at all, on the rising edge of the pulse, so that $t_f \leq t_p$. But in fact, the data show that in many cases $t_f > t_p$ by as much as 40 ns. The question of formative time-lag may be eliminated, because the data show that the prebreakdown phenomena occur on a much shorter time scale than this ($0 \leq w \leq 8 \text{ ns}$), while flashover itself forms quite rapidly ($\leq 2 \text{ ns}$). Therefore

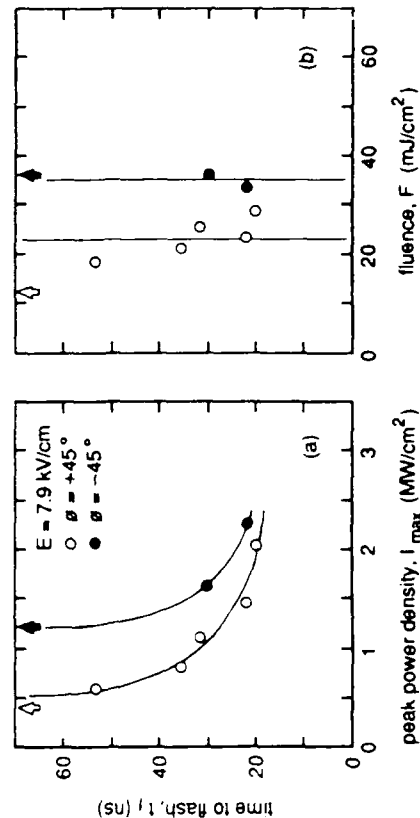


Fig. 4. Flashover behavior for insulators under ultraviolet illumination for electric field stress of 7.9 kV/cm. Arrows indicate shots for which flashover was not observed.

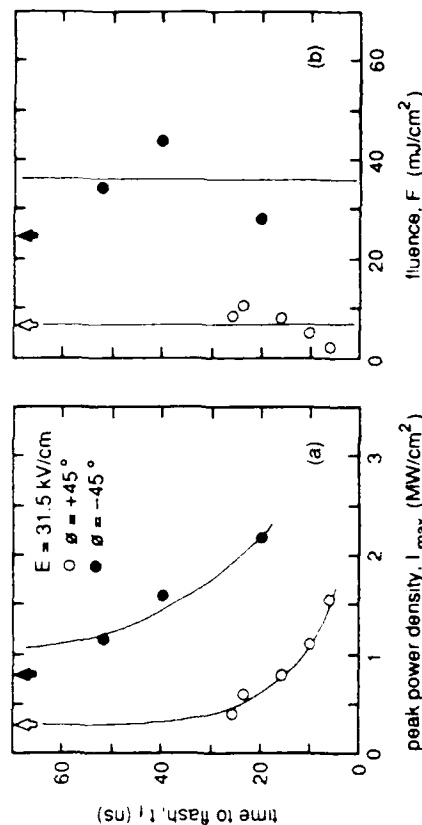


Fig. 7. Flashover behavior for insulators under ultraviolet illumination for electric field stress of 31.5 kV/cm.

is scatter in the data (typical of electrical breakdown phenomena), two trends are clear: (1) flashover voltage decreases as the ultraviolet fluence increases, and (2) the unconventional insulator orientation is more tolerant to ultraviolet illumination than the conventional. This latter observation is consistent with previous ultraviolet-induced insulator flashover studies.⁽³⁻⁴⁾

Open-shutter photography, as shown in Fig. 10, reveals that in the positive-angle configuration (lower photo) the discharge connects with the cathode triple point (as indicated by the bright spot in the photograph at that point) but appears to miss the anode triple point. In the negative-angle

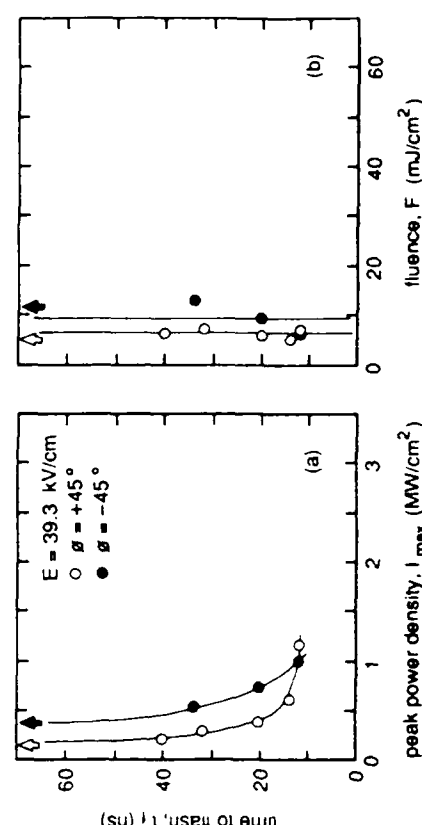


Fig. 8. Flashover behavior for insulators under ultraviolet illumination for electric field stress of 39.3 kV/cm.

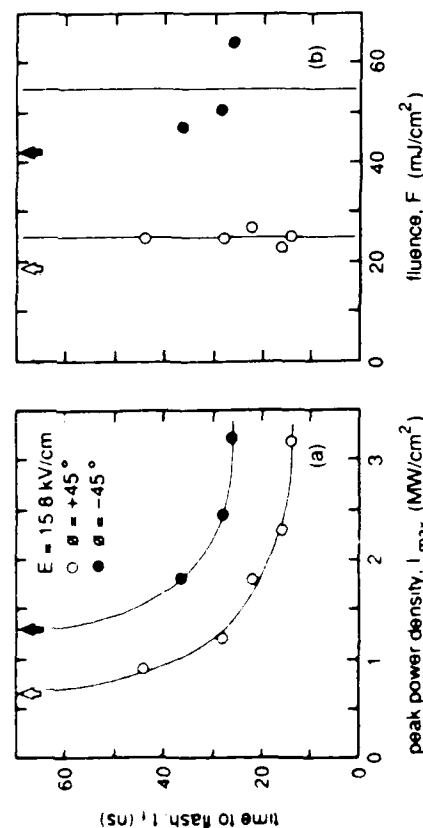


Fig. 5. Flashover behavior for insulators under ultraviolet illumination for electric field stress of 15.8 kV/cm.

we must conclude that it is fluence rather than intensity which is the key in ultraviolet-induced flashover. The data show that the critical fluence to initiate flashover is independent of $I(t)$ for this wavelength.

On the other hand, the critical fluence does depend on the electric field stress and the geometry. Figures 4-7 show the significant result that the unconventional geometry is more resistant to ultraviolet-induced flashover by up to a factor of 2 in fluence. Figure 9 compiles the data shown in Figs. 4-8 for both geometries, displaying the fluences required to initiate flashover shown in the right part of each figure versus electric field. Although there

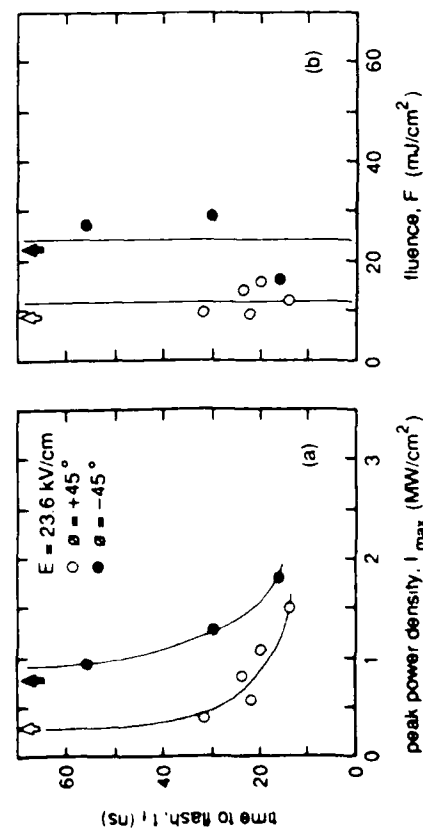


Fig. 6. Flashover behavior for insulators under ultraviolet illumination for electric field stress of 23.6 kV/cm.

the short formation times seen in these data, the photoemission of electrons, especially in the high-field regions of the triple point, seems to be the most plausible explanation, versus other mechanisms such as gas desorption from the insulator surface. The question arises, if illumination of the triple point is a key to ultraviolet-induced insulator flashover, can flashover be avoided by blocking illumination of the offending triple point? Our experimental observations indicate that it can. In an early experiment in this series, at low voltage and low power density (no converging optics used) in the positive-angle configuration, flashover was not induced when the cathode triple point was blocked, but flashover was induced when the triple point was illuminated, regardless of what other areas of the insulator were illuminated.

The role of impurities also appears to be important. In one series of shots with the insulator at positive angle, dielectric oil was found to have leaked through the vacuum feed-through and to have been drawn by capillary action up to the cathode triple point, although the insulator surface itself remained clean. Flashover voltage under ultraviolet illumination was found to have been reduced by approximately a factor of 2 versus a clean insulator. Vacuum grease accidentally left in the gap was found to cause a similar lowering of the flashover voltage. Since these contaminants may be present in practical systems, future research must develop a better physical understanding of their role in ultraviolet-induced insulator flashover.

ACKNOWLEDGMENTS

This research was supported by SDIO-IST, ONR, AFOSR, and a Presidential Young Investigator Award from the NSF. One of the authors (C.L.E.) was supported by AFIT/CI.

REFERENCES

1. P. J. Turchi and W. L. Baker, *J. Appl. Phys.* **44**, 4936 (1973).
2. W. L. Baker, M. C. Clark, J. H. Degnan, G. F. Kiuttu, C. R. McClenahan, and R. E. Reinovsky, *J. Appl. Phys.* **49**, 4694 (1978).
3. C. L. Enloe, R. Blaher, M. Coffing, and R. E. Reinovsky, Proceedings of the 10th International Symposium on Discharges and Electrical Insulation in Vacuum, Columbia, South Carolina, 1982 (IEEE Catalog No. 82CH1826-7), p. 308.
4. C. L. Enloe and R. E. Reinovsky, Proceedings of the 4th IEEE Pulsed Power Conference, Albuquerque, New Mexico, 1983 (IEEE Catalog No. 83CH1908-3), p. 679.
5. A. H. Guenther and J. R. Bettis, *J. Phys. D: Appl. Phys.* **11**, 1577 (1978).
6. A. H. Guenther and J. R. Bettis, Proceedings of the 5th IEEE Pulsed Power Conference, Arlington, Virginia 1985 (IEEE Catalog No. 85C2121-2), p. 47.
7. R. M. Gilgenbach, Proceedings of the 5th IEEE Pulsed Power Conference Arlington, Virginia, 1985 (IEEE Catalog No. 85C2121-2), p. 126.

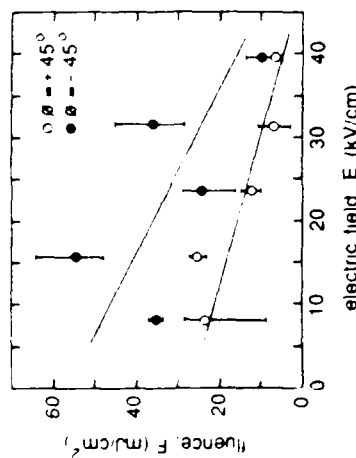


Fig. 9. Fluence required to initiate flashover as a function of electric field stress. Lines represent a least squares fit to all data for which breakdown was observed.

configuration (upper photo), the opposite appears to be true: the discharge connects with the anode triple point, but misses the cathode triple point. The discharge remains generally near the insulator surface in the negative-angle case, but appears to lift off a portion of the surface in the positive angle case. This lifting-off is more pronounced at higher voltages.

5. DISCUSSION

The flashover behavior of insulators in vacuum under pulsed over-voltages has been well characterized.^(8,10,11) The systematic investigation of insulator flashover under intense ultraviolet illumination has only begun over the last few years,^(1,4) so that detailed models do not yet exist. Given

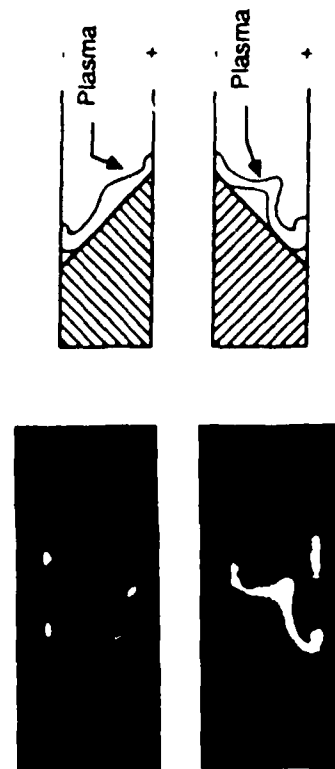


Fig. 10. Open-shutter photographs of insulator flashover at an electric field of 31.5 kV/cm for insulators at positive (lower) and negative (upper) angle.

UV-Induced Flashover of a Plastic Insulator

8. O. Milton, *IEEE Trans. Electr. Insul.* E1-7, 9 (1972).
9. A. Watson, *J. Appl. Phys.* 38, 2019 (1967).
10. R. Hawley, *Vacuum* 18, 383 (1968).
11. P. H. Gleichauf, *J. Appl. Phys.* 22, 766 (1951).
12. E. S. Borovik and B. P. Batrakov, *Sov. Phys. Tech. Phys.* 3, 1811 (1958).
13. A. A. Avdienko and M. D. Malev, *Sov. Phys. Tech. Phys.* 22, 986 (1977).

END
FILMED
4-89
DTIC